Precise nuclear data of the ^{14}N(p,γ)^{15}O reaction for solar neutrino predictions

Dissertation

zur Erlangung des akademischen Grades
Doctor rerum naturalium
(Dr. rer. nat.)

vorgelegt der Fakultät Physik

der Technischen Universität Dresden

von

Dipl.-Phys. Louis Wagner

geboren am 22. 03. 1988 in Weimar

Eingereicht am 11. 01. 2018

Verteidigt am 07. 06. 2018

Diese Dissertation wurde von Oktober 2013 bis Januar 2018 am Institut für Strahlenphysik des Helmholtz-Zentrums Dresden-Rossendorf und am Institut für Kern- und Teilchenphysik der Technischen Universität Dresden angefertigt.

1. Gutachter: Prof. Dr. Kai Zuber
2. Gutachter: PD Dr. Daniel Bemmerer
3. Gutachter: Prof. Dr. Shawn Bishop

Kurzdarstellung

Die ^{14}N(p,γ)^{15}O Reaktion ist die langsamste Phase im Bethe-Weizsäcker-Zyklus des Wasserstoffbrennens und bestimmt deshalb die Reaktionsrate des gesamten Zyklus. Präzise Werte für die Reaktionsrate sind notwendig um das Wasserstoffbrennen in unserer Sonne besser zu verstehen. Besonders das Problem widersprüchlicher Ergebnisse aus Vorhersagen des aktuellen Sonnenmodells und helioseismologischen Experimenten könnte durch genauer bekannte ^{14}N(p,γ)^{15}O Reaktionsraten aufgelöst werden.
Dafür soll der solare ^{13}N und ^{15}O Neutrinofluss von den β^+-Zerfällen als direkter Informationsträger über die Häufigkeit von Stickstoff und Kohlenstoff im Sonneninneren genutzt werden. Der für die Berechnung der Häufigkeiten benötigte Wirkungsquerschnitt der ^{14}N(p,γ)^{15}O Reaktion wurde in einer Evaluation verschiedener Messungen reduziert, da der Anteil des direkten Protoneneinfang mit Übergang in den Grundzustand deutlich weniger zum gesamten Wirkungsquerschnitt beiträgt als zuvor angenommen. Die evaluierte relative Gesamtunsicherheit ist mit 7.5 % dennoch hoch, was zu einem großen Teil an ungenügendem Wissen über die Anregungsfunktion in einem weiten Energiebereich liegt.
In der vorliegenden Arbeit werden experimentell ermittelte Wirkungsquerschnitte in Form von astrophysikalischen S-Faktoren für zwei Übergänge vorgestellt. Für den stärksten Übergang, den Protoneneinfang zum angeregten Zustand bei 6.79 MeV in ^{15}O, wurden zwölf S-Faktoren bei Energien zwischen 0.357 – 1.292 MeV mit geringeren Unsicherheiten als zuvor ermittelt und für den direkten Übergang in den Grundzustand zehn Werte zwischen 0.479 – 1.202 MeV.
Außerdem wurde ein R-Matrix Fit durchgeführt um den Einfluss der neuen Daten auf Extrapolationen zum astrophysikalisch relevanten Energiebereich zu prüfen. Die kürzlich vorgeschlagene Erhöhung des S-Faktors im Gamow-Fenster konnte nicht bestätigt werden und es wurden auch Unterschiede zu bisherigen Messungen im Energiebereich um 1 MeV deutlich. Die neuen extrapolierten S-Faktoren sind $S_{679}(0) = (1.19 \pm 0.10)$ keV b und $S_{\mathrm{GS}}(0) = (0.25 \pm 0.05)$ keV b und sie stimmen mit den von der Evaluation empfohlenen Werten im Rahmen ihrer Unsicherheiten überein.

Abstract

The ^{14}N(p,γ)^{15}O reaction is the slowest stage of the carbon-nitrogen-oxygen cycle of hydrogen burning and thus determines its reaction rate. Precise knowledge of its rate is required to improve the model of hydrogen burning in our sun. The reaction rate is a necessary ingredient for a possible solution of the solar abundance problem that led to discrepancies between predictions of the solar standard model and helioseismology.

The solar ^{13}N and ^{15}O neutrino fluxes are used as independent observables that probe the carbon and nitrogen abundances in the solar core. This could settle the disagreement, if the ^{14}N(p,γ)^{15}O reaction rate is known with high precision. After a review of several measurements its cross section was revised downward due to a much lower contribution by one particular transition, capture to the ground state in ^{15}O. The evaluated total relative uncertainty is still 7.5 %, in part due to an unsatisfactory knowledge of the excitation function over a wide energy range.

The present work reports experimentally determined cross sections as astrophysical S-factor data at twelve energies between 0.357 – 1.292 MeV for the strongest transition, capture to the 6.79 MeV excited state in ^{15}O with lower uncertainties than before and at ten energies between 0.479 – 1.202 MeV for the second strongest transition, capture to the ground state in ^{15}O.

In addition, an R-matrix fit is performed to estimate the impact of the new data on the astrophysical relevant energy range. The recently suggested slight S-factor enhancement at the Gamow window could not be confirmed and differences to previous measurements at energies around 1 MeV were observed. The present extrapolated zero-energy S-factors are $S_{679}(0) = (1.19 \pm 0.10)$ keV b and $S_{\mathrm{GS}}(0) = (0.25 \pm 0.05)$ keV b and they are within the uncertainties consistent with values recommended by the latest review.

Parts of the present data have been published in a peer-reviewed journal:

L. Wagner, S. Akhmadaliev, M. Anders, D. Bemmerer, A. Caciolli, St. Gohl, M. Grieger, A. Junghans, M. Marta, F. Munnik, T. P. Reinhardt, S. Reinicke, M. Röder, K. Schmidt, R. Schwengner, M. Serfling, M. P. Takács, T. Szücs, A. Vomiero, A. Wagner, K. Zuber
Astrophysical S-factor of the ^{14}*N(p,*γ*)*^{15}*O reaction at 0.4 – 1.3MeV*
Phys. Rev. C 97, 015801 (2018)

This work was supported by the Helmholtz Association (grant number VH-VI-417, Nuclear Astrophysics Virtual Institute NAVI) and the TU Dresden Graduate Academy.

Contents

List of Tables

List of Figures

1. Introduction

Our Sun always was a fascinating and important subject of astronomy and astrophysics. The close distance compared to all other stars provides the unique opportunity to measure stellar properties and processes with a precision virtually impossible for other stars. Understanding our Sun on a level that allows precise predictions of its development is not only important for the future life on earth but for the understanding of stellar evolution in general.

This chapter gives a more detailed motivation for the experiments presented in this work. First a short introduction to the nuclear fusion process under investigation is given in Sec. 1.1. It follows the implication of this process for evolution models of our Sun in Sec. 1.2. The last section provides an overview of important research about the topic conducted in the last three decades and how this work can improve the knowledge base (Sec. 1.3).

1.1. The carbon–nitrogen–oxygen cycle

The rate of the carbon–nitrogen–oxygen (CNO) cycle of hydrogen burning plays a crucial role in stellar models, both for energy generation (0.8 % of the total luminosity of the Sun) and for nucleosynthetic predictions of stellar evolution. The catalytic cycle burns hydrogen to helium with carbon, oxygen and nitrogen as catalyst. Its strong dependence on the plasma temperature in the stellar core makes the cycle more efficient for more massive stars then the Sun, where the temperatures are higher then in the Sun with $T_\mathrm{c} = 15.6 \cdot 10^6$ K. At even higher temperatures more heavy nuclei including fluorine participate in the burning process and additional cycles become important. In Fig. 1.1 the first two cycles with their participating reactions and isotopes are drawn.

Once cycle I in Fig. 1.1 has reached equilibrium, its rate is determined by the rate of the slowest reaction, ^{14}N(p,γ)^{15}O.

The ^{14}N(p,γ)^{15}O reaction proceeds by capture to the ground state and several excited states in the ^{15}O nucleus. Fig. 1.2 shows the Q value of proton capture on ^{14}N, the proton energies for resonant capture to ^{15}O and the relevant levels of ^{15}O with the respective J^π as the level spin and parity. The data are taken from Ref. [Ajz91], except

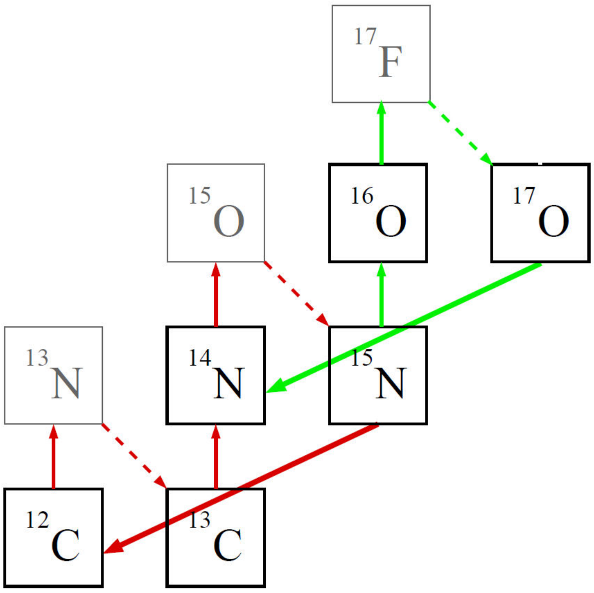

Figure 1.1.: Schema of the CNO cycle I (in red) and II (in green). The third and fourth cycle are not shown. Proton capture reactions are the vertical solid arrows, β decays are the diagonal dashed arrows and (p,α) reactions are the diagonal solid arrows. Nuclides shaded in gray are unstable.

where updated values from Ref. [ICF$^+$05] were available. The red arrows mark the transitions that were investigated in this work.

The ^{14}N(p,γ)^{15}O reaction cross section $\sigma(E)$ can be parameterized as the astrophysical S-factor $S(E)$ defined in Ref. [Ili07] by the relation:

$$S(E) = \sigma(E) \cdot E \cdot \exp\left(-\frac{2\pi}{\hbar} Z_0 Z_1 e^2 \sqrt{\frac{m_{01}}{2E}}\right) \tag{1.1}$$

where E is the proton energy in the center-of-mass frame of reference (c.m.), $Z_0 = 1$ and $Z_1 = 7$ are the charge numbers of H^{1+} and N^{7+} and m_{01} is the reduced mass from both particles.

The total S-factor of ^{14}N(p,γ)^{15}O is the sum of all S-factors from the different levels at a given energy and is denoted $S_{114}(E)$. The Gamow peak is the important narrow energy range where the ^{14}N(p,γ)^{15}O reaction occurs in stellar plasma with the highest rate. For the Sun this temperature dependent window is around the maximum of the Gamow peak of E_{Gamow} = 28 keV in the c.m. system. Because this is close to zero on an MeV scale, the S-factor of this energy is usually approximated as $S_{114}(0)$ although this would be exact only for a constant S-factor and corrections are determined by its

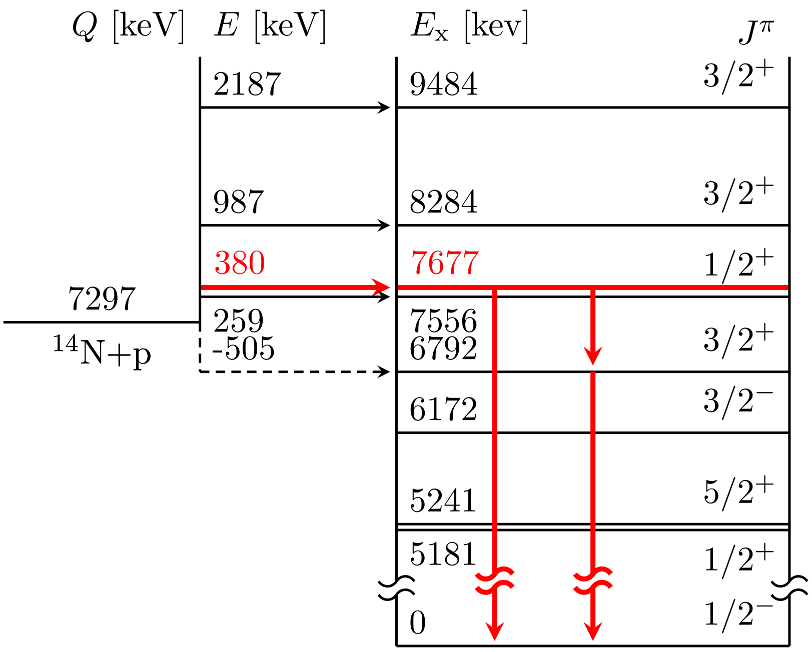

Figure 1.2.: Level scheme of ^{15}O with data from Ref. [Ajz91] and updated data from Ref. [ICF^{+}05]. The strongest transitions in the ^{14}N(p,γ)^{15}O reaction at 0.4 – 1.4 MeV proton beam energies are marked with red arrows, using a c.m. energy of 380 keV as an example.

first and second derivative $S'(0)$ and $S''(0)$. A constant S-factor around the Gamow window allows for an analytical calculation of the reaction rate $N_A\langle\sigma\nu\rangle$ given by:

$$N_A\langle\sigma\nu\rangle = N_A\sqrt{\frac{2}{m_{01}}}\frac{\Delta}{(kT)^{3/2}}S_{114}(0)e^{-3E_0/kT} \qquad (1.2)$$

from Ref. [Ili07, p. 178, Eq. (3.80)] with T the plasma temperature in the Sun core and Δ = 14 keV the width of the Gamow peak for this temperature.

1.2. The Solar Standard Model and solar neutrinos

Both the central value and the uncertainty of the ^{14}N(p,γ)^{15}O reaction rate are of significance for a number of astrophysical scenarios, such as hydrogen shell burning in asymptotic giant branch stars discussed in Refs. [HA04, HAL06], the dating of globular clusters like Refs. [ICF^{+}04, D^{+}04] did and the solar abundance problem brought up in Ref. [HS08].

The latter problem has arisen due to the re-determination of the elemental abundances in the Sun based on three-dimensional models for the solar atmosphere, which entailed a significant reduction of the adopted abundance values as described in Refs. [AGSS09, CLS^{+}11]. The abundances of the elements heavier then Helium, referred to as metals in the astrophysics community, are important input parameters of stellar evolution models. The most famous and best tested stellar model is the Solar Standard Model or short SSM. A first version by Bahcall, Fowler, Iben, and Sears was used 1963 in Ref. [BFIS62] to predict solar neutrino fluxes. Developed over more then two decades, Bahcall presented the Solar Standard Model 1989 in his Book "Neutrino Astrophysics" [Bah89].

The major input parameters besides the mentioned chemical abundances are the solar mass, radius, age and luminosity, the radiative opacity, the equation of state and nuclear parameters like the reaction rates of the proton-proton chain and the CNO cycle. The four important assumptions for the SSM construction explained in Ref. [Bah89] are that hydro-static equilibrium exists, that energy is only transported by photons and convective motion, that energy is only generated by nuclear reactions and that abundances only change because of nuclear reaction products. The last assumption was later updated to include diffusion effects discussed in Ref. [SPnGH13]. With an educated guess of starting parameters the iterative solar evolution code is repeated with varying starting values until the boundary conditions of the Sun which are mass, radius and luminosity at a given age are met.

Because the SSM depends on the correctness of its input parameters, updated input data can lead to deviations in the model predictions. The biggest change in the last decade was the new evaluation of elemental abundance of metals mentioned above. For further reference the updated SSM is called AGSS09 and the model with the old abundances GS98 as they are usually denoted in literature.

When fed into the SSM, the new, lower abundances lead to a predicted sound speed profile that is at odds with helioseismological observations. Fig. 1.3 shows the large discrepancy between the new AGSS09 model predictions and the observed sound speed data if compared to the small deviations of the old GS98 model predictions to the data. This conflict between two observables, i.e. elemental abundances and helioseismology, may in principle be addressed by studying an independent third observable.

It has been suggested by Ref. [HS08] to use solar neutrinos from the β^{+} decay of the CNO cycle nuclides ^{13}N, ^{15}O, and ^{17}F for this purpose. These neutrinos may in principle be detected at modern neutrino detectors like Borexino, described in Ref. [BBB^{+}14], SNO+ (Ref. [A^{+}16]), and possibly at the Chinese Jinping Underground Facility presented in Ref. [BCC^{+}17a]. Using the well-measured ^{8}B neutrino flux as a solar ther-

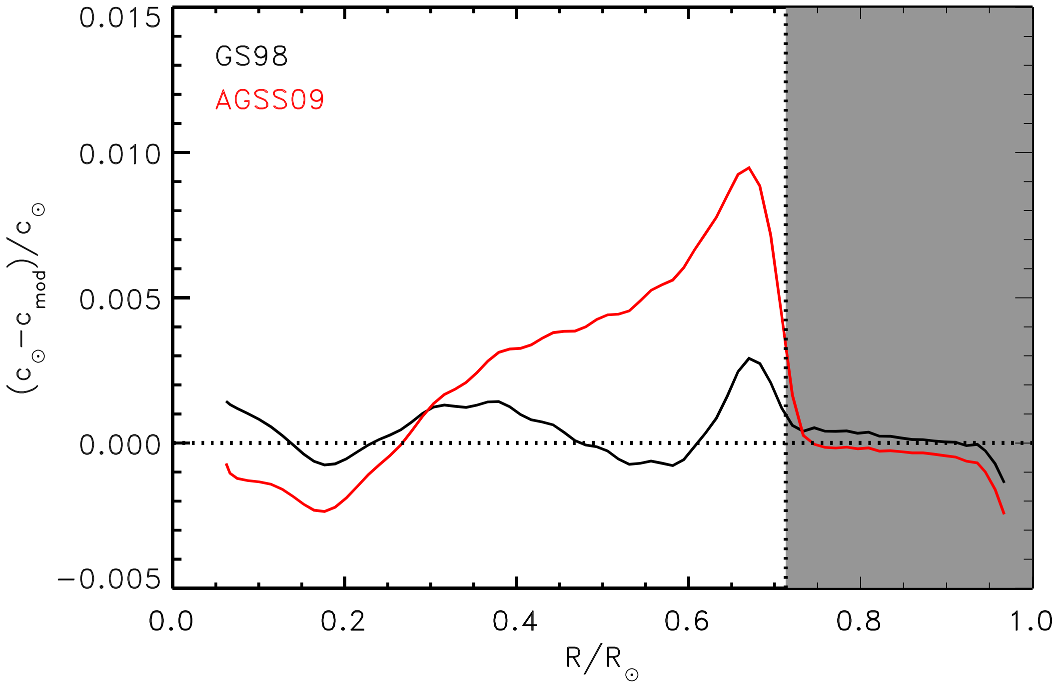

Figure 1.3.: Relative sound speed profile inside the Sun $(c(r)_{\text{solar}} - c(r)_{\text{SSM}})/c(r)_{\text{solar}}$ with $c(r)_{\text{SSM}}$ from the two SSM model predictions and $c(r)_{\text{solar}}$ from the helioseismology data of Ref. [BCE+09]. The red curve belongs to the low metal abundance of AGSS09 and the black to the higher metal abundance of GS98. Fig. taken from Ref. [HRS13].

mometer as in Ref. [TBSZ15], the CNO neutrino flux would be directly proportional to the abundances of carbon, nitrogen, and oxygen in the solar core as Refs. [HS08, SHP11] show.

As an example of the importance of neutrino flux measurements one can calculate the change in the ^{15}O neutrino flux prediction assuming the lower metal abundance from Ref. [AGSS09]. It would change by 30.7 %, states Ref. [SPnGH13]. But these solar neutrino flux predictions depend directly on the nuclear physics parameter $S_{114}(0) = 1.66 \pm 0.12$ keV b (from the latest review in Ref. [AGR+11]) with power-law dependencies for the neutrino flux of $\Phi(^{13}\text{N}) - 0.747$ and $\Phi(^{15}\text{O}) - 1.000$ according to Ref. [SPnGH13, Tab. I]. A comparison of predicted and measured neutrino fluxes would show if the lower metal abundances of Ref. [AGSS09] are correct but only if the uncertainties of the values are small enough to allow a 3σ distinction between predictions from old and new abundances. However, because the S_{114} uncertainty has the largest influence on the flux prediction uncertainty (see Ref. [SPnGH13, Tab. III]) such an approach presupposes that the rate of the Bethe-Weizsäcker cycle is known with an uncertainty better then

5 %. The present value with 7 % uncertainty from the review in Ref. [AGR+11] is not precise enough.

Precise nuclear physics input for the SSM is not only important for parameters of the Sun. Because the stellar evolution codes that form the basis of the SSM are used in many fields of stellar astrophysics a change of input parameters can have an impact on derived properties of other stars as well. A very recent study in Ref. [VRA+17] calculated the base of the convective zone and the helium ionization zone of stars observed with the *Kepler* space mission described in Ref. [KBB+10]. This was done by fitting the observed stellar oscillation frequencies with stellar models using ^{14}N(p,γ)^{15}O reaction rates from Refs. [FIC+04, ICF+05]. In the latest review mentioned above (Ref. [AGR+11]) those data were re-normalized by 3 %. Already this small change could have an impact on the results of the study.

Another recent study used stellar evolution models for a theoretical prediction of the brightness of the Red Giant Branch tip. In Ref. [SWC+17] the authors conclude that with careful stellar modeling that also includes consistent use of nuclear reactions, an accurate prediction for the luminosity of the Red Giant Branch tip is possible. Since this brightness is used in astrophysics as a reference value, changes of an input parameter of the used model can have far reaching consequences.

1.3. Overview on recent publications of ^{14}N(p,γ)^{15}O and aim of this work

The latest comprehensive ^{14}N(p,γ)^{15}O experiment covering a wide energy range has been reported in 1987 by the Bochum group of Ref. [SBB+87]. However, it is by now accepted that the Bochum-based value used in Refs. [SBB+87, AAB+98, AAR+99] of the stellar ^{14}N(p,γ)^{15}O rate must be revised downward by a factor of two.

This consensus in the review Solar Fusion cross sections II (SFII, Ref. [AGR+11]) is based on indirect data from Refs. [BCP+01, MBB+03, YMA+04], direct cross section measurements from Refs. [FIC+04, ICF+05, RCA+05, MFG+08, MFB+11, LGd+16] and R-matrix fits in Refs. [AD01, MBB+03]. The most important conclusion from these works is that the astrophysical S-factor, extrapolated to zero energy, for capture to the ground state in ^{15}O is $S_{\mathrm{GS}}(0) = 0.20 - 0.49$ keV b, not 1.55 keV b as previously reported by Ref. [SBB+87]. After this strong reduction, the remaining ambiguity in ground state capture has been the object of dedicated efforts, both by direct experiments in Refs. [MFG+08, MFB+11] and indirect experiments in Ref. [Mic13]. Tab. 1.1 lists the astrophysical S-factors extrapolated to zero energy for the important transitions in the ^{14}N(p,γ)^{15}O reaction from several of the mentioned references.

Table 1.1.: Astrophysical S-factor, extrapolated to zero energy, for the most important transitions in the ^{14}N(p,γ)^{15}O reaction from Bochum [SBB+87], LUNA [FIC+04, ICF+05, MFG+08, MFB+11], TUNL [RCA+05] and SFII [AGR+11]. Most recently the Notre Dame group [LGd+16] reported extrapolated S-factors for R/DC→6.79 MeV of (1.29±0.04(stat)±0.09(syst)) keV b and for R/DC→0 of (0.42±0.04(stat)$^{+0.09}_{-0.19}$(syst)) keV b.

Transition [MeV]	Bochum $S(0)$ [keV b]	LUNA $S(0)$ [keV b]	TUNL $S(0)$ [keV b]	SFII $S(0)$ [keV b]
R/DC→6.79	1.41±0.02	1.20±0.05	1.15±0.05	1.18±0.05
R/DC→6.18	0.14±0.05	0.08±0.03	0.04±0.01	0.13±0.06
R/DC→5.24	0.018±0.003	0.070±0.003		0.070±0.003
R/DC→5.18	0.014±0.004	0.010±0.003		0.010±0.003
R/DC→0	1.55±0.34	0.20±0.05	0.49±0.08	0.27±0.05
Sum	3.20±0.54	1.56±0.08	1.68±0.09	1.66±0.12

The present work, instead, concentrates on the ^{14}N(p,γ)^{15}O transition that dominates, the capture to the 6.79 MeV excited state. In addition, it also provides some new results for ground state capture. The 6.79 MeV transition accounts for ~70 % of the total cross section. Its S-factor curve, plotted in Fig. 1.4 is essentially flat over a wide energy range as shown by Ref. [SBB+87], indicating a dominance of direct capture and capture through very wide resonances. Indeed, the 6.79 MeV transition plays only a secondary role for the low-energy resonance at E = 259 keV investigated by Refs. [MFG+08, MFB+11]. The resonance has recently emerged as a precise normalization point for S-factor data and was repeatedly updated by Refs. [ICF+05, RCA+05, BCL+06, AGR+11, DKC+16]. The transition has not been detected in the subsequent resonance at E = 987 keV studied in Ref. [MTB+10].

Several recent R-matrix extrapolations for capture to the 6.79 MeV state converge in a narrow band at $S_{6.79}(0)$ = 1.15-1.20 keV b, with error bars as low as 4 %. They were done by the LUNA (Laboratory for Underground Nuclear Astrophysics) collaboration in Refs. [FIC+04, ICF+05], by TUNL (Triangle Universities Nuclear Laboratory) in Ref. [RCA+05] and in SFII from Ref. [AGR+11]. Two works, however, report somewhat higher central values and also higher uncertainties. The first, based on a measurement of the asymptotic normalization coefficient governing direct capture and a subsequent R-matrix fit including the data available at the time (i.e. without the LUNA and TUNL data), reported a value of $S_{6.79}(0)$ = (1.40±0.20) keV b in Ref. [MBB+03]. The second, based on a comprehensive R-matrix fit including not only new capture data but also angular distributions, gave a value of $S_{6.79}(0)$ = (1.29±0.04(stat)±0.09(syst)) keV b

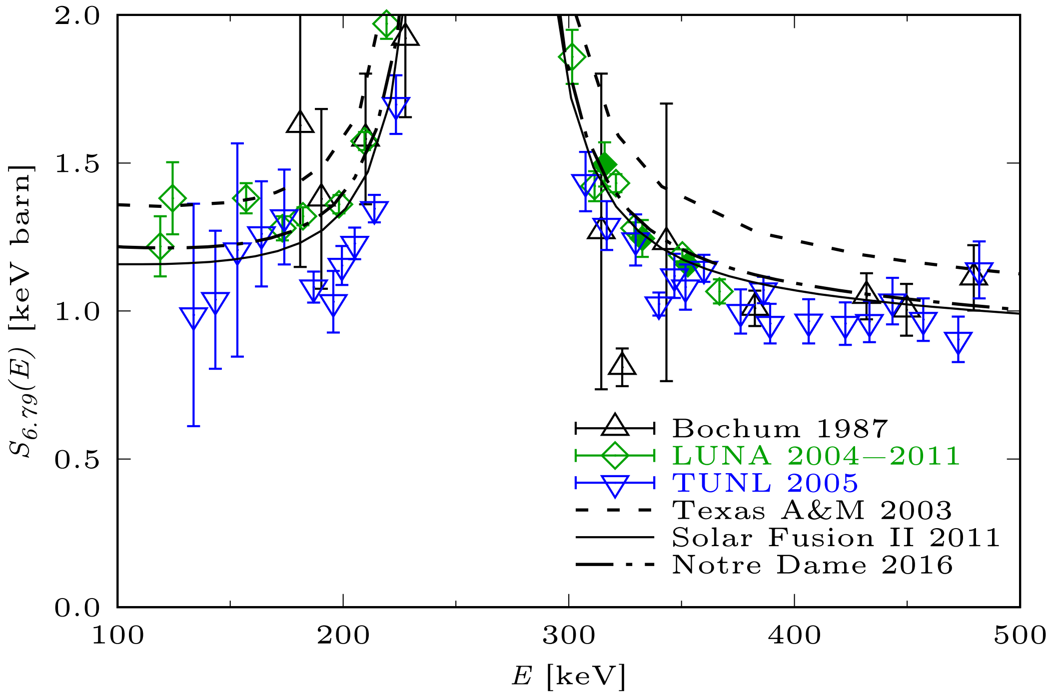

Figure 1.4.: Astrophysical S-factor for capture to the 6.79 MeV excited state in the ^{14}N(p,γ)^{15}O reaction at low energy from the Bochum [SBB+87], LUNA [FIC+04, ICF+05, MFG+08, MFB+11], and TUNL [RCA+05] experiments, respectively. R-matrix fits by the Texas A&M [MBB+03], SFII [AGR+11], and Notre Dame [LGd+16] groups, respectively, are shown as lines.

in Ref. [LGd+16].

These various R-matrix fits may be benchmarked against recent and precise experimental capture data at relatively low energy, E = 100-500 keV (Fig. 1.4). However, it should be noted that there is still a significant energy gap from the data points at 100-500 keV to the solar Gamow energy, E_{Gamow} = 28 keV.

Summing detector data from LUNA reach down to the lowest energies hitherto measured, E = 70 keV, and provide a value for the total S-factor, summed from all transitions, of 1.7 keV b from Refs. [LBC+06, BCL+06]. However, by design the summing data cannot constrain the partial S-factor for capture to the 6.79 MeV level very well.

Even though the experimental situation at E = 100-500 keV is satisfactory as Fig. 1.4 shows, for several important energy intervals at higher energy, E > 500 keV, the only existent radiative capture data set is still the one from Bochum in Ref. [SBB+87]. For another transition in ^{14}N(p,γ)^{15}O , the ground state capture, the Bochum data had to be corrected by up to 50 % by Refs. [FIC+04, AGR+11] for the so-called true coincidence summing-in effect described in Ref. [Gil08]. This effect led to an artificial increase of the signal for ground state capture by the coincident detection of the DC→6.79 MeV and 6.79 MeV→0 γ-rays. It was neglected in the original publication of Ref. [SBB+87] but was corrected for in subsequent work as mentioned above. The same process leads to the loss of counts in the 6.79 MeV→0 γ-ray, by the true coincidence summing-out effect. This latter effect scales with the total γ-ray detection efficiency and may thus reach values up to 10 % in close geometry. The Bochum excitation function was taken at close distance, with just 2 cm separating the target from the detector end cap.

A very recent study from Notre Dame in Ref. [LGd+16] contributed radiative capture data for capture to the 6.79 MeV level in the 1.5-3.4 MeV energy range and for the ground state transition from 0.6-3.4 MeV . In the important range around 1 MeV, for the 6.79 MeV transition, angular distributions are reported but integrated S-factor data are missing in Ref. [LGd+16].

Because of the possible systematic uncertainty given by the neglected summing effects in the Bochum data set from Ref. [SBB+87] and the limitations of the very recent Notre Dame data set, it is necessary to perform an independent experimental study of the ^{14}N(p,γ)^{15}O cross section over a wide energy range. The present work aims to provide this cross-check, by supplying new and impartial capture cross section data for two ^{14}N(p,γ)^{15}O transitions in the E = 366-1289 keV energy range. The energy range is chosen in a way that there is some overlap to the recent and precise low-energy data at 100-500 keV from LUNA and TUNL.

2. Experimental setup to measure ^{14}N(p,γ)^{15}O

The realization of the experiment required several devices to count the γ-rays from the capture reaction of hydrogen on nitrogen in the laboratory.
This chapter describes the components of the experiment on ^{14}N(p,γ)^{15}O including the source, the accelerator, the target and its chamber as well as the γ-ray detection and the signal chain. In total three measurement phases were carried out from 2013 to 2015 each with different proton energies as summarized in Tab. 2.1.

2.1. Accelerator

The proton beam for the experiment was provided by the 3 MV Tandetron, described in Ref. [FBHT96]. This tandem accelerator is located at the Helmholtz-Zentrum Dresden-Rossendorf (HZDR), Germany. It has a Cs sputter ion source HVEE 860-C Ref. [FT03] that provides negative hydrogen ions H^- with injection energies of $U_{\text{inject}} \cdot e = 25\,\text{keV}$. The source is connected to an injection magnet with a rectangular deflection to select the ions by charge per mass ratio. In the first half of the accelerator tank the ions receive an increase in kinetic energy proportional to the terminal voltage potential. The Cockcroft-Walton generator next to the terminal, made of capacitors and diodes in a voltage multiplier ladder network, is used to generate the high voltage and a so-called generating voltmeter is needed to measure the high acceleration potential. To avoid sparks the terminal is insulated in a tank with SF_6 under a pressure of 8 bar.

Table 2.1.: Beamtimes for the ^{14}N(p,γ)^{15}O experiment.

Beamtime	start	end	proton energies [keV]
Phase 1a	07/01/2013	11/01/2013	747.5; 857.0; 956.4
Phase 1b	28/01/2013	01/02/2013	532.5; 640.0; 1114.6; 1191.7; 1301.2
Phase 2	17/03/2014	22/03/2014	406.7; 852.9
Phase 3	09/03/2015	13/03/2015	640.0; 680.5; 852.9; 1299.2; 1400.6

By interacting with the circulating nitrogen stripper gas in the center of the tank, the hydrogen ions experience a charge reversal because they lose two electrons in the charge exchange ionization with the nitrogen molecules. Therefore the now positive ions can be accelerated a second time towards the exit of the tank, again with an energy proportional to the high voltage on the terminal U_{term}. The total kinetic energy in the laboratory frame of a proton E_{p} after exiting the accelerator tank is then calculated by

$$E_p = (U_{\text{inject}} + 2\frac{U_{\text{term}}}{r}) \cdot e \cdot c \tag{2.1}$$

with e the elemental charge and $c = 1{,}0142 \pm 0{,}0003$ as a calibration constant for the true proton energy derived in earlier experiments of Ref. [Sch11, p. 63] at this accelerator. After those calibration measurements a second voltmeter was installed to get a better resolution for the terminal voltage ($\Delta U_{\text{term}}(new) = 0.01\,\text{kV}$) because the old voltmeter readout has an uncertainty of 0.5 kV. To correlate the new voltmeter with the old both values were taken each time and then the difference $U_{\text{term}}(new) - U_{\text{term}}(old)$ was set against $U_{\text{term}}(old)$ to make a linear fit without offset. The result was a ratio $r = U_{\text{term}}(new)/U_{\text{term}}(old) = 1.0059$ with a coefficient of determination of $R^2 = 0.999994$. Using $U_{\text{term}}(new)$ divided by r in Eq. (2.1) reduced the systematic uncertainty on E_{p} to be below 0.06%.

After the acceleration the ion beam passes the electrostatic quadrupole lens, the analyzing magnet as well as horizontal and vertical deflectors. One last limiting of the beam is done by a collimator, consisting of a water cooled copper plate with a round hole of 5 mm in diameter in the middle. At this collimator at least 10% of the beam intensity was deposited in order to ensure a homogeneous beam on the target.

The last element the beam has to pass through before hitting the target is a 12 cm long copper tube with 2 cm diameter, that is electrically insulated from the chamber. Whenever the target, consisting of titanium nitride (TiN), is hit by an ion, electrons can be emitted from the target if the energy exceeds the work function (W_{TiN} =4.5 eV from Ref. [LDDF12]). The approximated energy W transferred to an electron at rest is

$$W = 4T\cos(\Theta)^2 = 4 \cdot \frac{m_e}{m_p} \cdot T_0 \cdot \cos(\Theta)^2 \tag{2.2}$$

as derived from equations in the Appendix of Ref. [RKMG92] with m_e and m_p the electron and proton mass at rest, T_0 the incident proton kinetic energy and Θ the angle of the ejected electron with respect to the beam axis. For 1 MeV protons Eq. (2.2) indicates a transferred energy of 2176 eV for the forward scattered electrons and a lower energy for angles away from the beam axis.

An earlier experiment Ref. [Tro09] with the same setup showed that the backward scattered electrons that leave the target only have a very low energy below 25 eV because -25 V on the mentioned copper tube were sufficient to deflect those secondary electrons (SE) back on the target. To ensure the accuracy of the current measurement -100 V were applied onto a feedthrough to this tube. Since the number of protons that have hit the target is determined by the total charge deposition on the target, the lost electrons would otherwise lead to an overestimation of the number of protons without this suppression. The current was not only measured at the target, but on the collimator too, in order to know how much beam current was lost there. Although the collimator also produces secondary electrons and therefore produces no accurate current measurement, this information is still important in the process of adjusting the magnets and steerer to get the maximum beam current onto the target.

Several Faraday cups along the beam line, which can be moved into the beam temporarily to measure the current, can give additional hints on how the beam can be optimized. Because of inhomogeneity and degradation of the ion source the beam current decreases over time and optimizations were done regularly to keep the target current approximately constant. As an example the current trend of target Ca-TiN-2 is plotted in Fig. 2.1 for a beam energy of 680 keV. An overview of the average target currents is given in Tab. 2.3.

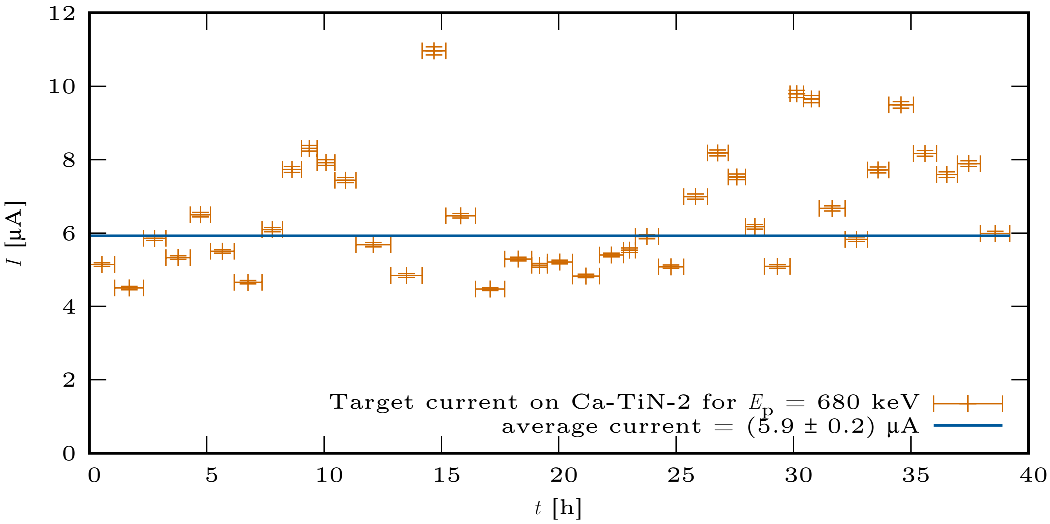

Figure 2.1.: The current measured on target Ca-TiN-2 over the irradiation time was $5.9 \pm 0.2\,\mu\mathrm{A}$ on average. The graph shows some larger deviations towards higher currents that were no problem for the setup or the target. Deviations towards currents lower then $4\,\mu\mathrm{A}$ could be prevented by periodical beam alignment corrections.

The beam adjustment at the lowest proton energy of E_p = 400 keV was the most difficult for the operators. The reason is that with a low kinetic energy below 10 % of the maximum provided by the terminal the ions are stronger influenced by any weak electric or magnetic field with diverging effects on the beam. One outcome was that the beam was much less focused and up to 70 % of it hit the collimator. In the end, the average current on the target with this proton energy was only a fourth of the highest currents measured at higher proton energies as Fig. 2.2 shows. This circumstance is especially disadvantageous, if combined with another aspect. The reaction cross section drops by two orders of magnitude from the highest to the lowest energy. As a consequence both aspects lead to much longer irradiation times for good statistics at low proton energies as will be shown in Sec. 3.3.

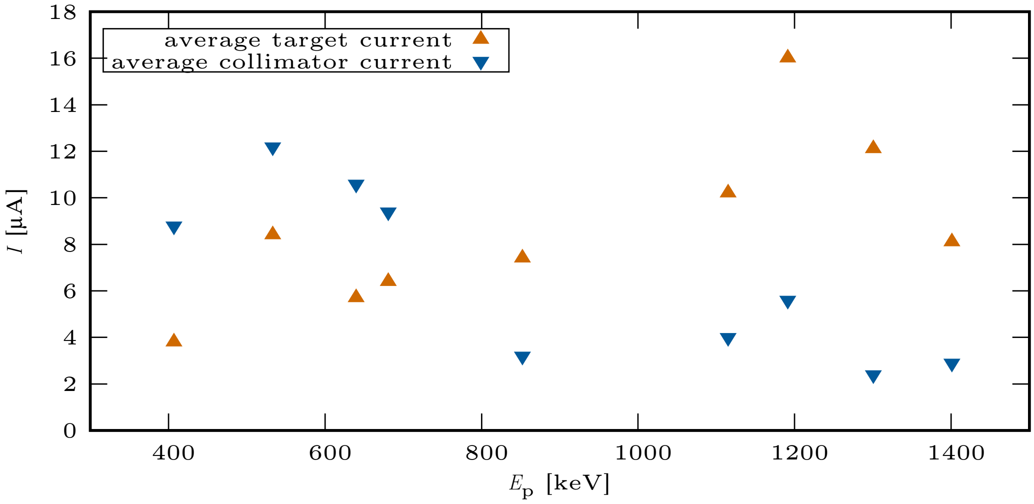

Figure 2.2.: The average currents from target and collimator in dependence on the beam energy show that for energies above 800 keV more ions hit the target than were stopped at the collimator. For lower energies the opposite case is true because the beam could not be focused as well as for high energies. This trend holds true despite the problem, that the collimator had no SE suppression and the absolute collimator current is thus systematically measured too high.

The complete beam line is kept under high vacuum of at least $5 \cdot 10^{-7}\,\mathrm{mbar}$ to minimize interactions of the beam with any residual gas. During the first runs, the vacuum in the target chamber had to be better than $1 \cdot 10^{-6}\,\mathrm{mbar}$ before the irradiation runs were started. Because the analysis showed that on some targets a buildup of an impurity layer of carbon was found after the irradiation, in the succeeding runs the scroll pump was replaced by an oil free type and the pressure had to be one order of magnitude lower then in the first runs.

It turned out that a qualitative difference of the beam spots could be seen already by visual inspection. If one compares the targets of measurement phase one in Fig. 2.3 with those from the second and third phase in Fig. 2.4, only a brown spot appeared where the beam hit the later targets but no blue or gray area is visible like on the first targets. A quantitative analysis of these differences is given in Sec. 3.2.2, showing that the improved setup reduced the carbon buildup by $50-60\,\%$. One way to reduce contaminants even more could be the use of a cold trap in front of the target which is a planned upgrade for the target chamber.

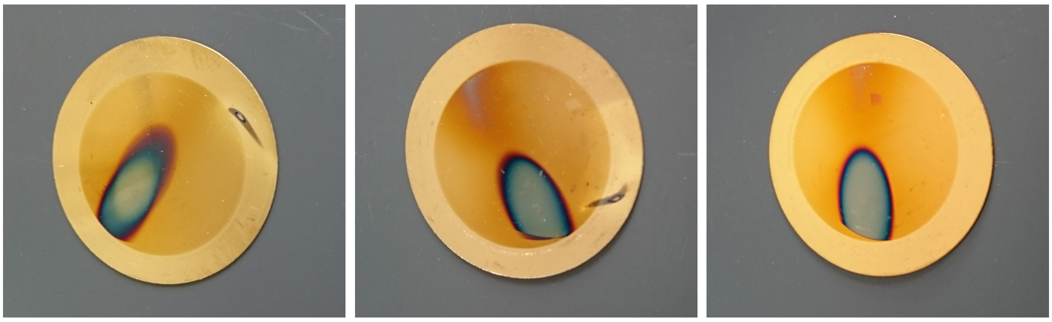

Figure 2.3.: The targets of phase 1 (order from left to right) Vom-TiN-5, Vom-TiN-6 and St-TiN-1 all had a clear beam spot on the golden TiN layer after irradiation. The gray metallic ellipsoidal spots are surrounded by a blue ring followed by a ring with black and brown shades.

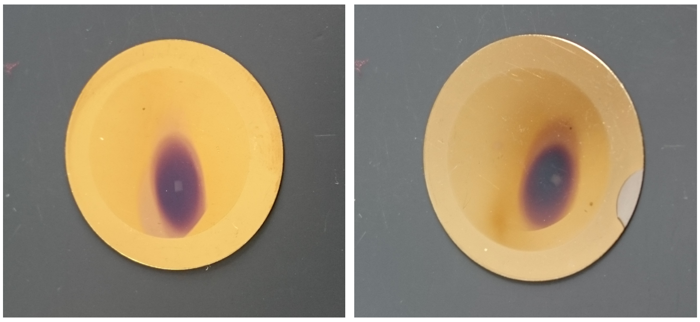

Figure 2.4.: The targets of phase 2 & 3 St-TiN-5 (left) and Ca-TiN-2 (right) both had only a brown ellipsoidal spot on the golden TiN layer from the irradiation.

The brighter concentric band on the edge of each target marks the area that was covered by the target holder ring. It is important, that the ellipsoidal beam spot is not cut by this band. An overlap would indicate, that part of the beam hit the metal holder and not the target. The result would be a decrease in the γ-rays from the ^{14}N(p,γ)^{15}O reaction and an increase from unwanted γ-lines from ^{27}Al(p,γ)^{28}Si . Moreover the current measurement would be the same, because the target and the ring are electrically connected. On the first run of the first measurement phase this problem came up because the mentioned γ-lines of ^{27}Al(p,γ)^{28}Si found in the on-line spectra had higher count rates than expected. The run was stopped and the yield from the aluminum reaction was halved by varying the beam sweep horizontal offset of the beam line. However, the increase in the monitor γ-line peak from ^{15}N(p,$\alpha\gamma$)^{12}C explained in detail in Sec. 3.3.1 was insignificant within the statistical uncertainty. For the other targets the visual inspection showed less to no overlap.

Since the chamber had to be opened several times during the experiment to change the targets, it was flushed with dry nitrogen gas while it was open to avoid humidity entering the chamber. A closed shutter always separated the open chamber from the evacuated beam line at those times.

2.2. Targets

The advantages and disadvantages of solid targets compared to gas targets that are summarized in Tab. 2.2 will be discussed in this section.

Admittedly, the targets listed in Tab. 2.3 for the ^{14}N(p,γ)^{15}O experiment were solids mainly from practical reasoning, because a target chamber for solid targets was already available for the beam line at the HZDR. It was used for several experiments in the last years (see Ref. [MTB^{+}10, SAA^{+}13, DCF^{+}15, RAB^{+}16]) and is well known, while a windowless gas target chamber would have to be built first. On the other hand, this decision meant that the nitrogen had to be bound in to a solid compound that could withstand high vacuum conditions and the bombardment with high energy protons.

Table 2.2.: Advantages and disadvantages of the solid TiN targets for the ^{14}N(p,γ)^{15}O experiment compared to a nitrogen gas target.

Advantages	Disadvantages
• well known target chamber • easy cooling procedure • small energy loss • defined thickness • can be analyzed afterwards • simple pumping setup • small interaction point	• composite material for solid N • backing needed • very thin film necessary • elaborate coating process • endurance depends on stoichiometry • contaminant buildup • stopping power dominated by Ti

Table 2.3.: Overview of mounted TiN targets with thickness, picked up total charge, average current and proton irradiation energies.

Target tag	made at	nominal thickness	charge [C]	current [μA]	E_p [keV]
Vom-TiN-5	INFN-LNL	170 nm, $90\,\mu\mathrm{g}/\mathrm{cm}^2$	2.40	8.93	747.5; 857.0; 956.4
Vom-TiN-6	INFN-LNL	170 nm, $90\,\mu\mathrm{g}/\mathrm{cm}^2$	1.82	9.62	532.5; 1114.6; 1191.7; 1301.2
St-TiN-1	HZDR	140 nm, $70\,\mu\mathrm{g}/\mathrm{cm}^2$	0.86	10.92	640.0
St-TiN-5	HZDR	170 nm, $90\,\mu\mathrm{g}/\mathrm{cm}^2$	1.46	3.98	406.7; 852.9
Ca-TiN-2	INFN-CIVEN	200 nm, $105\,\mu\mathrm{g}/\mathrm{cm}^2$	1.92	6.12	640.0; 680.5; 852.9; 1299.2; 1400.6

Target tag	mount	dismount	Remarks
Vom-TiN-5	07/01/2013	11/01/2013	very stable over irradiation; visible C layer
Vom-TiN-6	29/01/2013	01/02/2013	stable till end of 1. beamtime; visible C layer
St-TiN-1	28/01/2013	29/01/2013	possible degradation of TiN layer; thick C layer
St-TiN-5	17/03/2014	22/03/2014	very stable over 5 days; weak beam spot
Ca-TiN-2	09/03/2015	13/03/2015	stable over 5 days; weak beam spot

Titanium nitride was used to fulfill this task, because this ceramic material has a high mechanical hardness and is chemically only reactive above 800°C (from Ref. [Mün57]). Since the proton beam heats the target with a power P that is the product of the acceleration voltage of Eq. (2.1) and the target current I_target an upper limit of the heating power would be $P = 1.5\,\mathrm{MV} \cdot 20\,\mu\mathrm{A} = 30\,\mathrm{W}$. A very small part of this power (<0.6 W) is deposited in the target because of the energy loss of the protons (see Sec. 3.2.1) but the protons are stopped in the much thicker tantalum backing which is connected to a cycle of deionized cooling water. The thermal conductivity of Tantalum is $\lambda = 57.5\,\mathrm{W/m{\cdot}K}$ at room temperature (from Ref. [ACA+11]). With Fourier's law of thermal conduction

$$\dot{Q} = \lambda \cdot A \frac{\Delta T}{d} \tag{2.3}$$

and assuming equilibrium between the thermal conduction through the tantalum backing and the heating power from the protons stopped in the tantalum the temperature increase on the target can be calculated.

Solving Eq. (2.3) for ΔT with the backing thickness $d = 0.22\,\mathrm{mm}$, the beam spot area $A = 66\,\mathrm{mm}^2$ and $\dot{Q} = P = 30\,\mathrm{W}$ gives an increase of $\Delta T = 1.8\,\mathrm{K}$. Because Eq. (2.3) assumes heat conduction only perpendicular to the surface from the beam spot to the backside and not over the whole tantalum backing it only provides an upper limit for the temperature increase. This effectively prevents unwanted heating-up of the target and keeps the conditions constant during the irradiation. In addition to the heat dissipation, the backing serves as the support structure for the very thin TiN layer. The reason for the thin layer is, that the protons may only lose a small amount of energy in the target so that no resonance energy below the original proton energy is accidentally hit. These thin films of only several hundred nanometer thickness need, however, an elaborate creation process. It is called reactive magnetron sputtering according to Ref. [RMP+01a] and is described briefly in the next paragraph.

For the target production via a reactive sputtering process a vacuum chamber with substrate anode, target cathode and magnetron inside is needed. Like common sputtering the potential between substrate anode (tantalum backing) and target cathode (titanium disk) ionizes the inert working gas argon, which has a very low gas pressure below 10^{-4} mbar. But in addition the magnetron behind the cathode improves the plasma density on the target surface and thus increases the yield of sputtered Ti atoms by a higher bombardment rate with Ar^+ ions. The nitrogen induced in the chamber as the reactive gas reacts, as the name suggests, with the Ti that condenses on the substrate. The ratio of Ti and N on the substrate is mainly influenced by the partial pressure of N and the proportion should be near the stoichiometrical 1:1 ratio of Ti:N. This ensures that the above mentioned properties of TiN are met. Once a satisfying set of parameters is found, the target thickness is only determined by the time the process is kept going. For example with the setup used at the HZDR this took several hours per target. Other targets of Tab. 2.3 were produced in Italy at two National Institutes for Nuclear Physics (INFN) LNL and CIVEN. Further details on the Italian setup can be found in Ref. [RMP+01b].

With the described process the layer of TiN is very homogeneous as the examination by Elastic Recoil Detection Analysis (ERDA) (see Sec. 3.2.2) confirmed and has a well defined thickness as target scans in Sec. 3.2.1 show. This makes the description of the energetic profile of the targets much less complicated than working with the effective lengths of a gas target. In addition the solid targets were examined by ERDA after the irradiation to see any effects the ion bombardment had on the composition of the target. Already during the experiment it became clear that the durability varied a lot from target to target because of different stoichiometry and thickness. Thus the target endurance needed to be monitored for the whole irradiation time. The above mentioned buildup of contaminants is another disadvantage of the solid targets that shifted the effective proton energy about 2 keV in average because of the energy loss in the contaminant layer. But the improved pumping system that reduced those residual gases in the chamber is still rather simple compared to systems for windowless gas targets that often have a multi staged pumping scheme (see Ref. [CCL$^+$02] for example).

2.3. γ-ray detectors and electronics

2.3.1. High-purity germanium detectors

To detect the high energy photons from the ^{14}N(p,γ)^{15}O reaction with a very good energy resolution two high-purity germanium (HPGe) detectors were used. The Ge crystals of such detectors typically have net impurity concentrations of about 10^{10} atoms/cm^3 according to Ref. [ES08]. The HPGe detectors, manufactured by Canberra both need positive bias voltage to be applied but the crystal of detector one is an n-type and the crystal of detector two is a p-type. At an angle of 55° with respect to the beam axis detector one, model EGC 100-250-SEG4 was installed. It has four crystal segments of 86.5 mm length and together they form a single ended coaxial shape of 76.5 mm in diameter.

For this experiment only the summing signal of the four segments was read out by the electronics and with 394 cm^3 of active volume the detector has 100 % relative efficiency according to the data sheet. As defined in Ref. [ES08] this relative efficiency is given in relation to a standard 3 by 3 inches NaI(Tl) detector measuring the 1332.5 keV gamma line of a ^{60}Co source in 25 cm distance on the symmetry axis. Detector two, model GC6020 has a single ended coaxial shaped crystal too, but is not segmented. With a smaller crystal length of 60 mm and a diameter of 71 mm it has only 60 % relative efficiency and is placed perpendicular to the beam axis. The measured distances from the detector end caps to the target are shown in Fig. 2.5 for the setup used in the second phase 2014 and they are the same for the other two phases within $\approx 2\,\mathrm{mm}$.

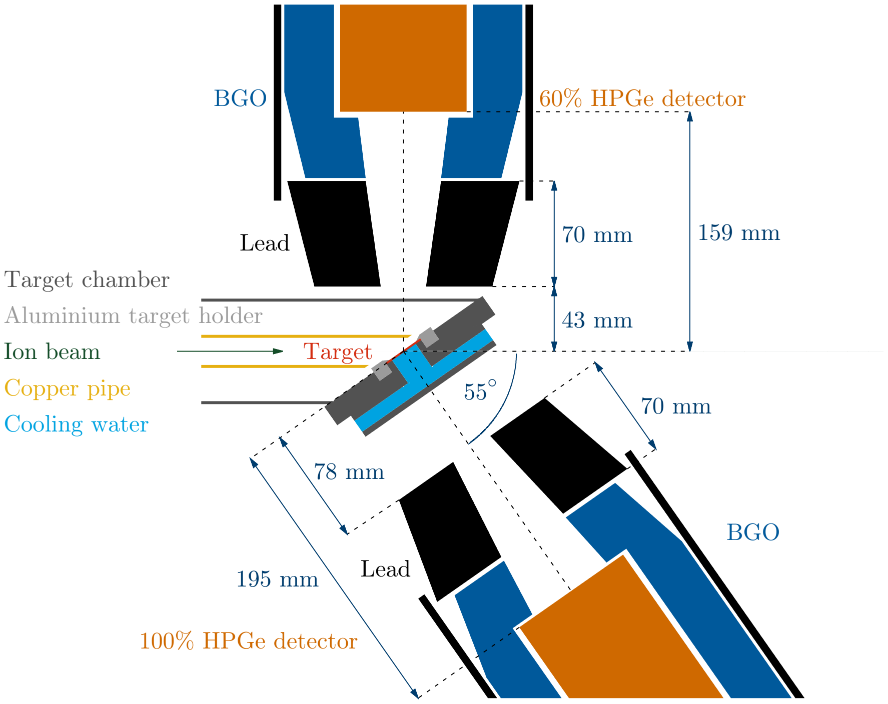

Figure 2.5.: Schematic sketch of the setup in top view with the proton beam (green) coming from the left side towards the target (red) in the center. The detectors (orange) at 55° and 90° with respect to the beam axis are surrounded by the BGO (blue) and the lead shielding (black). Adapted from Ref. [SAA$^+$13] with updated distances and not true to scale. (Only the front parts of the detectors are drawn.)

2.3.2. Detector shielding

The detectors are surrounded by two types of shielding against unwanted background radiation as Fig. 2.6 from the visualization of the simulation shows. The outer layer consists of a 20 mm thick hollow cylinder of lead and a lead collimator at the front with a thickness of 70 mm. The radiation coming from the target can pass unattenuated through a 30 mm hole. The passive shielding at the side reduces the γ-radiation background from natural sources roughly by a factor of three. The collimator in the front attenuates γ-rays by a factor of 50 to efficiently absorb γ-radiation coming from the target that would not hit the HPGe detector but only the surrounding layer of active shielding described in the next paragraph.

For muons a much thicker passive shielding of several hundreds of meters of material would be needed to see a significant reduction. Instead an additional different layer of shielding is in place around the detector, again in the approximate shape of a hollow cylinder. The 30 mm thick layer consists of bismuth germanate ($Bi_4Ge_3O_{12}$) or short

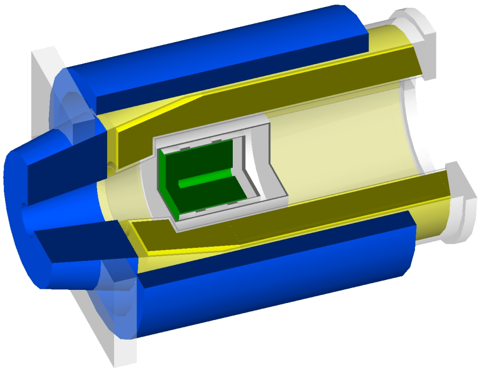

Figure 2.6.: 3D schematic of detector 2 with a quarter cut along the symmetry axis to see the inner parts. Starting from the center one can see the HPGe crystal (green), enclosed by the end cap and support structures (gray). The BGO scintillator (yellow) and the lead shield (blue) surround the Detector in a cylindric form. The drawing is true to scale. Detector 1 has the same housing but longer and segmented crystals. The cooling rod and photomultiplier tubes are not shown.

BGO that acts as a solid scintillator with very high detection efficiency for ionizing radiation like muons and γ-rays. The eight photomultiplier tubes attached at the end transform and exponentially amplify the light signal into an electric signal that can be processed by the electronics described in Sec. 2.3.3. Because the logic unit triggered a veto every time the BGO had a signal above the threshold, background radiation that entered through the BGO shielding was significantly reduced in the spectra. The effect of an active veto on the detector with 60% relative efficiency was studied in detail in Ref. [SBR$^+$15].

Radiation that isn't fully absorbed in the HPGe crystal and leaves the detector volume because of scattering by the Compton effect or pair production would not account for the full energy peak of the gamma spectrum but for the Compton continuum or the escape peaks. But since the escaping radiation has a high chance to leave a signal in the BGO, the event can be vetoed out and this leads to a better peak to background ratio in the spectrum, as seen in Fig. 2.7 at the 6790 keV full energy peak for example. Without the active veto the peak is almost completely covered by the background. The feature to suppress Compton scattered events in the spectra is the reason that the BGO detector is also called anti Compton shield.

2.3.3. Electronics

A data acquisition (DAQ) system has to handle several input signals and store them in an adequate way for further analysis. To effectively reduce the amount of data generated

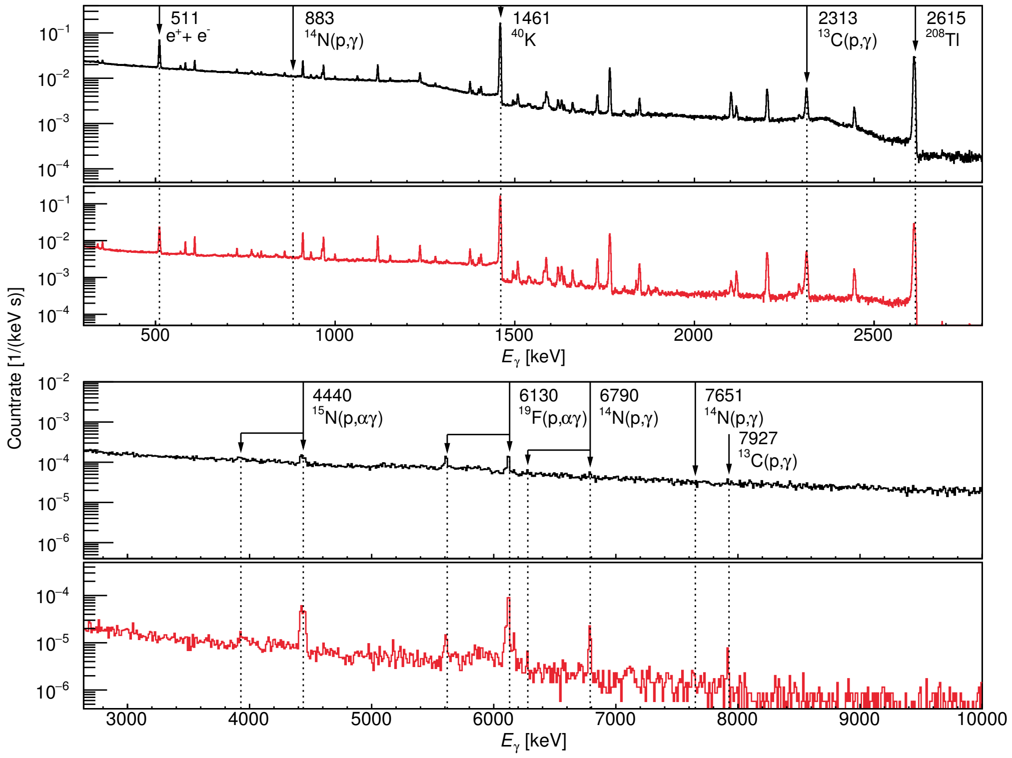

Figure 2.7.: γ-ray spectrum in the 55° detector. The top, black spectrum is the in-beam spectrum at E_p = 406 keV without the active veto. The bottom, red spectrum is the same measurement but with activated anti-Compton veto. The spectra are rescaled with the irradiation time of 97 hours.

in the ^{14}N(p,γ)^{15}O experiment, histograms were used to save energy spectra of the detector signals.

As mentioned in the previous Sec. 2.3.2 the active part of shielding produced signals as well. Those were not saved separately but had direct influence on the acceptance of detector signals. The signals of the two BGO's first passed an Octal Constant-Fraction Discriminator (CFD), ORTEC model CF8000 to control the signal shape and timing and second an Octal Gate Generator, ORTEC model GG8000, to get coincident signals for the Quad 4-input Logic, ORTEC model CO4020. To each BGO signal the other input was the according HPGe detector signal. But first these signals from the detector preamplifier passed the Spectroscopy Amplifier, ORTEC model 671 using the count rate meter (CRM) output to have a standard logic signal and were transformed by a NIM-TTL-NIM Adapter, C.A.E.N. model N89 for compatibility reasons. For the BGO signal acting as a veto in the logic the AND connection of BGO and detector was adapted by the N89 level translator again and passed to the pile-up rejection (PUR) input of the EtherNIM multichannel buffer, ORTEC model 919E. With this the shaped pulses from the amplifier unipolar (UNI) output were rejected in the EtherNIM DAQ if the BGO had fired too. This on the other hand meant only escape suppressed HPGe signals were counted in the system. Connected to a Windows PC via LAN the software ORTEC MEASTRO-32 multichannel analyzer (MCA) emulator took the data from the EtherNIM and stored them in separate histograms for each of the two detectors. To assure a simultaneous start and end of gamma counting and charge counting, which is described in the next paragraph, the "change sample" output of the 919E was connected to the gate input of the scaler used and controlled via software commands.

The charge collection from the target, mounted on the electrical insulated chamber end cap, was managed by a Digital Current Integrator, ORTEC model 439. It generated pulses of $10^{-8}\,\mathrm{C}$ that were counted in a Quad Scaler and Preset Counter/Timer, C.A.E.N. model N1145 with the above mentioned gate for the measurement time. The precision of the beam current calibration was estimated as 1 %. Afterwards the charge record was assigned to each measurements filename manually.

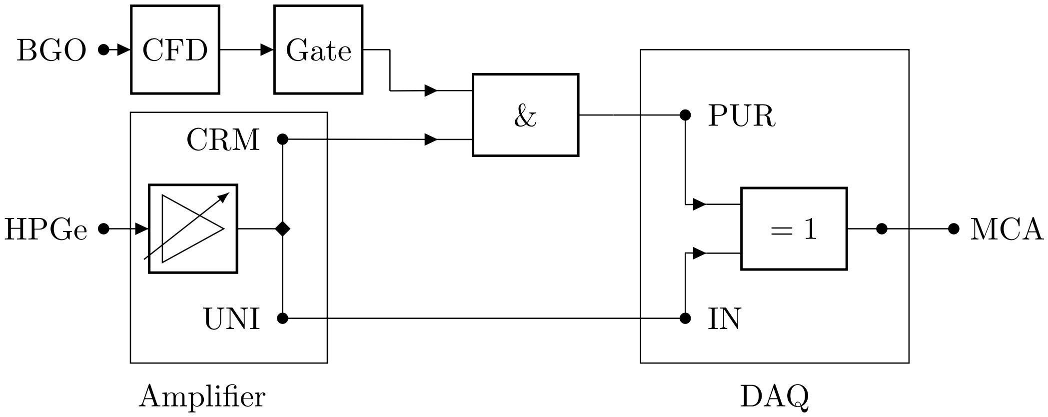

Figure 2.8.: The logic circuit of processing BGO and HPGe detector signals.

3. Analysis of measurements

In order to get the energy dependent S-factors $S(E)$ of the ^{14}N(p,γ)^{15}O reaction from the raw gamma spectroscopy histogram data several steps have to be taken. The first section in this chapter describes the energy and efficiency calibration of the detector (Sec. 3.1). The next step is the characterization of the used targets in Sec. 3.2 with two independent methods. The analysis of the gamma spectra is explained in detail in the last section Sec. 3.3.

3.1. Detector calibration

For the energy calibration of detector one and two no additional measurements were necessary. In every gamma spectrum of the irradiation experiment prominent peaks were clearly identified over the full range of interest to calculate a calibration function. A linear relation with offset was assumed because of the well known detector characteristics from previous experiments (see Ref. [Sch11, p.54] for details). The identified peaks were the electron positron annihilation peak at 511 keV, the natural background peaks of ^{40}K and ^{208}Tl at 1461 keV and 2615 keV respectively and two beam induced background peaks of ^{19}F(p,$\alpha\gamma$)^{16}O at 6130 keV and ^{15}N(p,γ)^{16}O at 12127 keV + $E_{\text{c.m.}}$. The last two γ-ray energies were corrected for the recoil effect when the γ-ray is radiated from the nuclei. This reduces the γ-ray energy depending on the initial energy E_γ and the nuclei mass m and is calculated with Eq. (3.1), adapted from the time reversed inelastic collision. The last reaction was corrected with Eq. (3.2) in addition for the Doppler shift at detector one ($\alpha = 55°$) because the decay is not at rest. This is in contrast to the γ-ray from ^{19}F(p,$\alpha\gamma$)^{16}O where the ^{16}O nucleus has time to be stopped considering the disexcitation half life of 18.4 ps.

$$E_{\text{recoil}} = -\frac{E_\gamma^2}{2 \cdot m \cdot c^2} \tag{3.1}$$

$$E_{\text{doppler}} = E_\gamma \left(1 - \frac{1}{1 - \frac{v}{c} \cdot \cos\alpha}\right), \text{with} \tag{3.2}$$

$$v = \frac{\sqrt{2 m_{\text{p}} E_{\text{p}}}}{(m_{\text{p}} + m_{^{15}\text{N}}) \cdot c} \tag{3.3}$$

Eq. (3.3) calculates the reaction product nuclei velocity from inelastic collision with $m_{^{15}\mathrm{N}}$ and m_p as the ^{15}N and proton mass at rest and the proton energy E_p in the lab frame.

To know the full-energy peak detection efficiency as a function of energy, ^{60}Co, ^{88}Y, and ^{137}Cs γ-ray intensity standards calibrated to activity uncertainties better than 1% (68% confidence level) by Physikalisch-Technische Bundesanstalt (PTB), Braunschweig, Germany were used. In addition, the ^{27}Al(p,γ)^{28}Si reaction studied in Ref. [AKHF77] was measured.

Determining the efficiency curve consists of two parts. The first part is a fit to the results of the intensity standards measurements with Eq. (3.4) with parameters a and b to get the low energy detection efficiency and the true rate of the ^{27}Al(p,γ)^{28}Si reaction from the 1.779 MeV peak.

$$\varepsilon(E_\gamma) = \exp\left(a + b \cdot \ln \frac{E_\gamma}{1.779\,\mathrm{MeV}}\right) \tag{3.4}$$

$$\varepsilon(E_\gamma) = \exp\left(x + y \cdot \ln \frac{E_\gamma}{6.792\,\mathrm{MeV}} + z \cdot \left(\ln \frac{E_\gamma}{6.792\,\mathrm{MeV}}\right)^2\right) \tag{3.5}$$

Second, for E_γ from 1.7 MeV to 20 MeV the efficiency curve was fitted with Eq. (3.5), varying parameters x,y and z to extend the energy range. Therefore the count rates of the ^{27}Al(p,γ)^{28}Si reaction measurement and the known relative γ-ray intensities and angular corrections from Ref. [AKHF77] of the γ-rays with higher energy up to 11 MeV were used in the "two-line method" (see Ref. [ZJAvdL90] for details of this method).

The result is an empirical parametrization using Eq. (3.4) below 1.7 MeV and Eq. (3.5) above this threshold with always less then 3 % uncertainty for the detection efficiency of the analysed peaks. An example is shown for phase 3 in Fig. 3.1. The uncertainty increases significantly after the last data point at 10.763 MeV as the residuum shows, but this is not in the region of interest any more. The curve of detector 1 had a up to 35 % higher efficiency for low energy γ-rays (<2 MeV) compared to phase 1 and 2, because a different detector from Ortec had to be used. Although the nominal relative efficiencies on the data sheets were the same with 100 %, apparently γ-rays were counted more efficiently at low energies in the new detector. The reason could be the thinner end cap out of carbon of the Ortec detector and the closer distance between crystal and end cap (4 instead of 6 mm). The curves of detector 2 were the same within 2 % in all three phases, because the setup was the same. The curves of phase 1 and 2 are Fig. A.1 and Fig. A.2 in the appendix.

In addition, the target chamber and γ-ray detectors were modelled in the Geant4 v10.2 (Geometry and Tracking) Monte Carlo framework of Ref. [A$^+$03] using the nominal

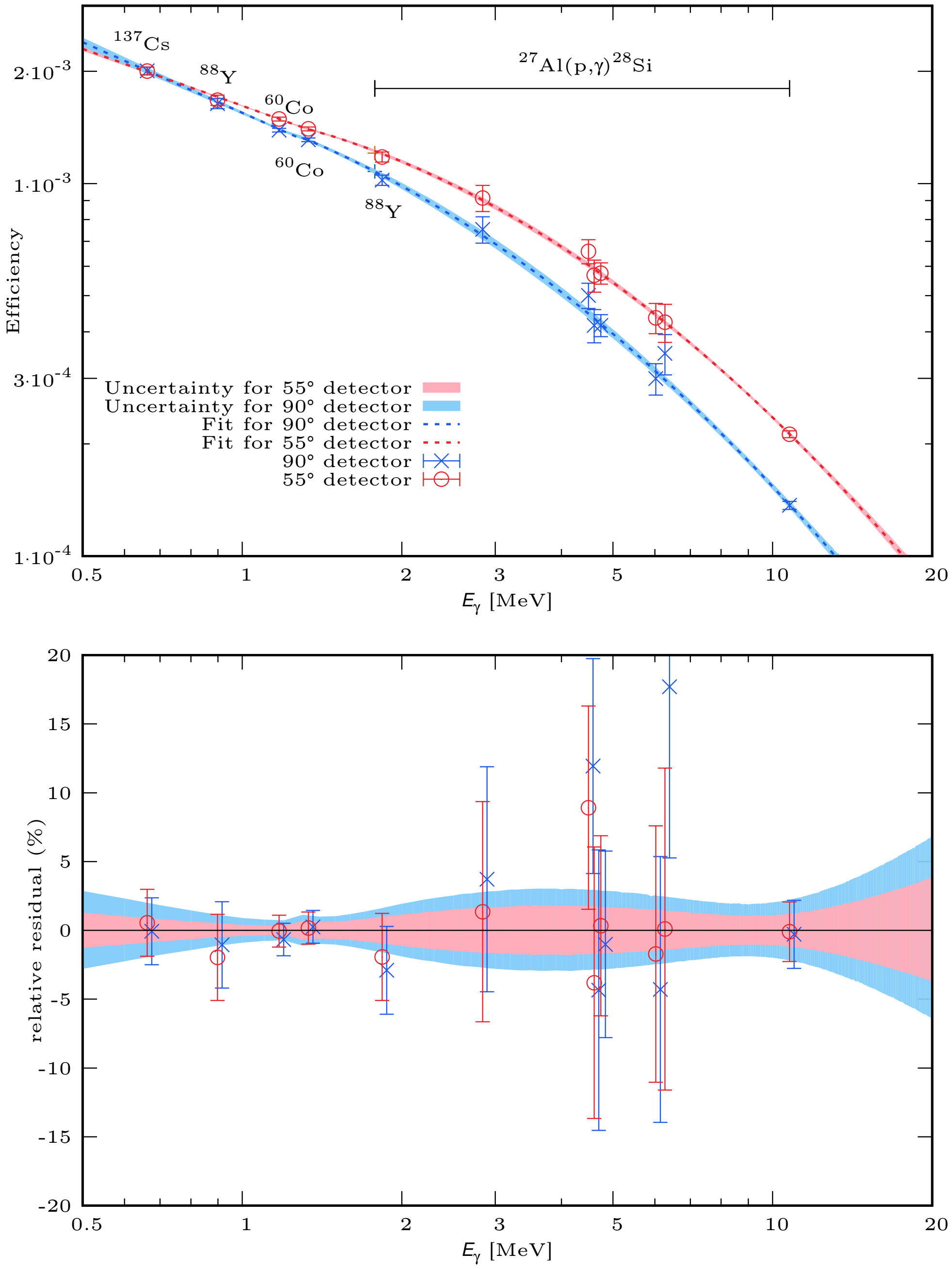

Figure 3.1.: The calculated γ-ray detection efficiency $\varepsilon(E_\gamma)$ for detector 1 at 55° in red and detector 2 at 90° in blue, tagged with the source (decay or ^{27}Al(p,γ)^{28}Si reaction) are in the top panel together with the fitted efficiency curves and their uncertainties. The bottom panel shows the relative differences to the respective fit. Plotted are the results of phase 3.

geometry provided by the manufacturer. The Monte Carlo simulation was only used to check if geometric corrections for the finite solid angle subtended by the detectors were necessary and for the prediction of the shape of the Compton edge and continuum. The peak detection efficiency for the data analysis was always taken from the experimental data and their parameterization (Fig. 3.1) instead.

3.2. Target analysis

A very important task during the experiment was the monitoring of the target. The target was positioned inside a closed vacuum chamber as described in Sec. 2.1 and a visual inspection would have cost several hours of beam time, because of the pumping process afterwards. To have a clue if the target still had the right properties and was not destroyed by the intense proton bombardment a reaction with high photon count rates in the spectra was monitored.

The reaction ^{15}N(p,$\alpha\gamma$)^{12}C with a broad peak at E_γ = 4.439 MeV from the 2^+ level in ^{12}C is well suited for this task because it is intrinsic in the target. That is despite the fact that only 0.3663 % of nitrogen with natural abundance is the isotope ^{15}N (see Ref. [CBd$^+$02]) because it is compensated by a high cross section. A constant rate of γ-radiation from this reaction suggests that the ^{14}N content stays the same during the irradiation as well. A count rate drop on the other hand would indicate a problem with the target, like degradation of the TiN layer. This of course is only true if the beam current is constant over the irradiation. Otherwise one has to correct the rates for the varying beam current or compare the differential yields.

3.2.1. Nuclear Resonant Reaction Analysis (NRRA) technique

Not only the online monitoring was done with the ^{15}N(p,$\alpha\gamma$)^{12}C reaction. To have more detailed information about the target a resonance scan was performed before and after every long term irradiation. Using the narrow resonance at a proton energy of E_p = 897 keV in the lab system and small increments of the proton energy in the range E_p = [850; 950] keV the target profile could be investigated. Because of the similar proton energy range no big changes in beam focusing were necessary for this *in situ* measurement. About 1 mC accumulated charge per energy step were sufficient to have enough counts from the 4.439 MeV γ-rays for statistical uncertainties below 3 % in the resonance region. Outside of the resonance region the counts were far fewer, of course, inducing the typical trapezoidal shape of the target scan profiles as shown in Fig. 3.2.

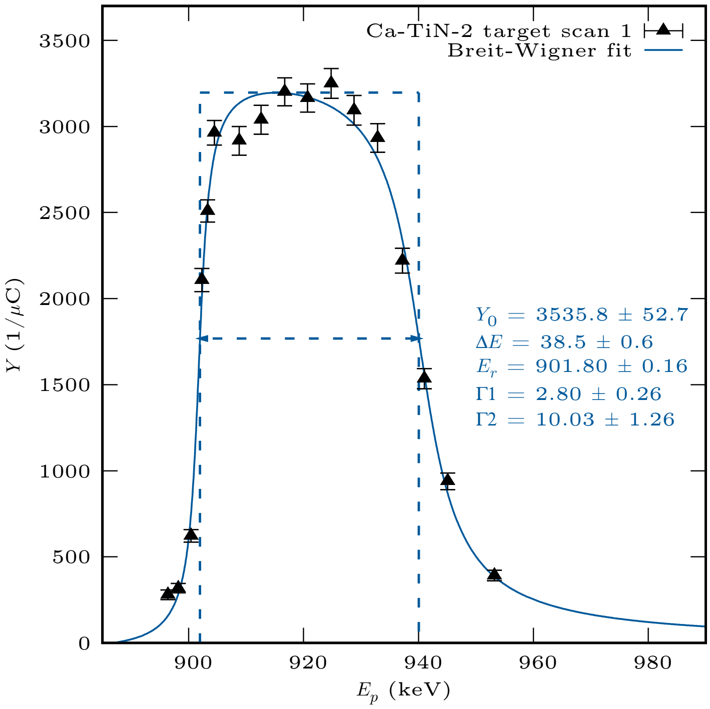

Figure 3.2.: The first resonance scan of target Ca-TiN-2 is plotted in black and the fit to Eq. (3.6) with results of the free parameters are shown in blue. The rising edge on the left, the yield plateau in the middle and the falling edge on the right define basic target properties. All values except the yield Y have the unit keV.

There the yield of ^{15}N(p,$\alpha\gamma$)^{12}C is drawn against the used proton energy in the laboratory frame for target Ca-TiN-2. As soon as the proton energy exceeds the resonance energy the yield increases with a steep rise. With higher energy the protons have to lose some keV in the target by collision and scattering losses before the resonance energy is reached. If the energy is even higher the ions can't lose enough energy on their way through the target for a resonant reaction to occur and the yield decreases significantly back to the non-resonant value. This trend can be described analytical by Eq. (3.6), the adapted Breit-Wigner formula from Ref. [Ili07, p. 339, Eq. (4.100)] if the stopping power ϵ is energy independent over the resonance width $\Gamma_{\mathrm{lab}} = 1.47$ keV of Ref. [TWC93, Tab. 16.22]. Since ϵ changes less than 0.2 % in this energy range the assumption is justified. Therefore, the energy dependent yield curve $Y(E_p)$ from the scan was fitted with the parameterization

$$Y(E_p) = \frac{\lambda_r^2}{2\pi}\frac{\omega\gamma}{\epsilon_r}\left[\arctan\left(\frac{E_p - E_r}{\Gamma_1/2}\right) - \arctan\left(\frac{E_p - E_r - \Delta E}{\Gamma_2/2}\right)\right]. \tag{3.6}$$

The free parameters for the fit are E_r the resonance energy, ΔE the target thickness, $\Gamma_{1,2}$ the adapted partial widths and the effective stopping power ϵ_r. The fixed parameters on the other hand are the de Broglie wavelength λ_r which can be calculated for this system and the resonance strength $\omega\gamma = 362 \pm 20$ eV that was previously measured by Ref. [MTB+10].

The γ-ray angular distribution of this resonance and a weaker one at lower energy, $E_\text{p} = 430$ keV has last been studied in details in the 1950s in Ref. [BJN52, KFFL53] and was found to be strongly anisotropic. A very recent re-study of the $E_\text{p} = 430$ keV resonance's γ-ray angular distribution led to the different results of Ref. [RAB+16]. This induced some doubts concerning the 897 keV resonance angular distribution and resonance strength. In addition, consecutive scans before and after long-term irradiation showed a little ($< +15\,\%$) increase in the yield plateau in eight of twelve cases. This highly unexpected behavior could not be explained by the build-up of a carbon layer or other contaminants on the target surface.

Therefore, pending further re-investigation of the 897 keV resonance as well, in the present work the NRRA yields obtained with this latter resonance are used only for relative monitoring of one given target between the start and the end of the irradiation. On the other hand, the results of the maximum proton energy loss in the targets ΔE, that is independent from angular distributions and the resonance strength, was found reliable if compared to the independent method described in the next paragraph Sec. 3.2.2. An overview of the results can be found in Tab. 3.2 at the end of this section.

3.2.2. Elastic Recoil Detection Analysis (ERDA) technique

After the *in situ* analysis and the long-term irradiations concluded, each target was again analyzed. But this time the heavy-ion elastic recoil detection (HI-ERD) technique at the HZDR 6 MV Tandetron accelerator was used.

For the analysis, the accelerator provided 43 MeV chlorine ions. The HZDR HI-ERD setup and analysis use well known techniques that are standard in material science and have been described previously in Ref. [KMH+14]. The raw ERD data visualized in Fig. 3.3 were converted to a depth profile using the NDF software of Ref. [BJW97] and elemental stopping powers from the SRIM software (The Stopping and Range of Ions in Matter) described in Ref. [ZZB10, Zie13].

One advantage of the HI-ERD technique was the precise positioning of the very small beam spot. On each target studied, two separate loci were analyzed. One was well inside the beam spot area, the second one well outside. This assured an independent measure

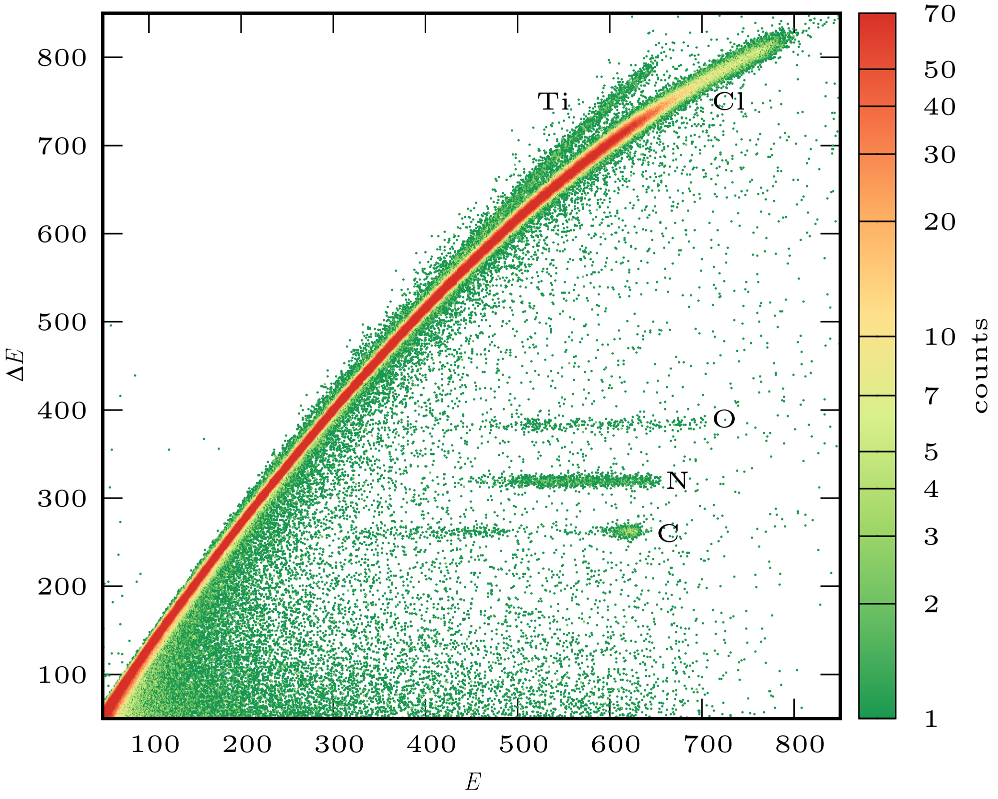

Figure 3.3.: Stoichiometry counting spectrum of target Ca-TiN-2. The x- and y-axis are in arbitrary units of energy. The spanned plane of energy loss over total particle energy allows an element separation. The target elements N and Ti, the contaminants C and O and the Cl from the beam are marked. The H signal is too weak to be seen in this plot.

of the degradation of the target under bombardment, in addition to the resonance scans (Sec. 3.2.1). For two of the targets no HI-ERD outside the spot was done, because it was not necessary for the main analysis. The data are discussed using the results from target Ca-TiN-2 in the beam spot area (Fig. 3.4) as an example. The initial layer found already in the NRRA scan is reproduced by ERDA. The analysis showed that it is carbon. This is consistent with the fact that the beam spot appears slightly black.

Behind this initial layer, a 2590 $\cdot 10^{15}$ atoms/cm^2 thick layer of TiN is found, with a stoichiometric ratio of TiN$_{0.97}$. This layer also contains 3-10 atom% hydrogen. This element can be found in tantalum and may have migrated from the backing to the TiN layer. This assumption is supported by the fact that the ERDA shows a peak in the hydrogen concentration up to 40 atom% in the Ta backing. On the other hand the backing underwent a cleaning process with hydrochloric acid.

After the TiN layer, a thin Ti layer is present. Looking at the ΔE over E plot of Fig. 3.3

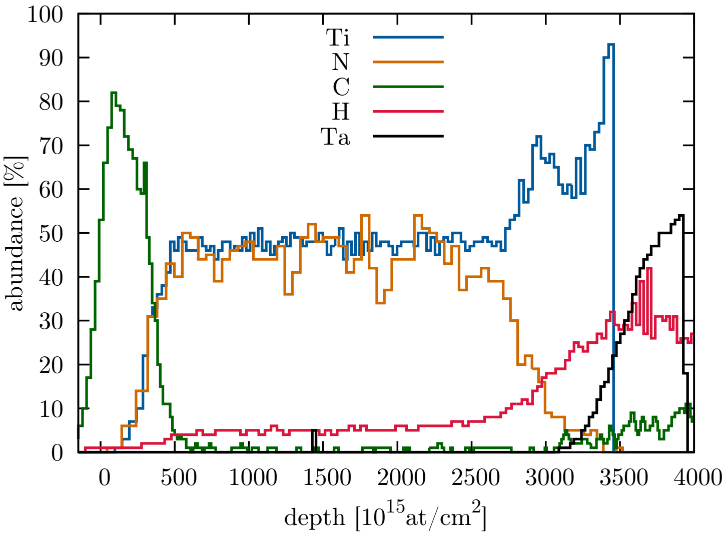

Figure 3.4.: Depth profile of target Ca-TiN-2. With the data from Fig. 3.3 the elemental ratio at depths up to $4000 \cdot 10^{15}$ atoms/cm^2 was calculated to have a profile of the target stoichiometry. The small (<1 %) Oxygen fraction was not plotted for clarity reasons.

shows that the separation between Ti from the target and the back scattered Cl beam becomes difficult at greater depths because of the higher atomic mass of Ti (47.87 u) compared to Cl (35.45 u). This made a cut off for the Ti signal necessary right before overlapping with the Cl signal. This problem might be solved by using a beam with ions heavier then Ti and an increased beam energy. But for our purpose this was not necessary, because in the region of interest (the target layer) the Ti signal was separable from the Cl signal. The apparent pure Ti layer behind the TiN layer might not be as thick as shown in Fig. 3.4 because of the mentioned separation problem. This problem is the reason for the sharp cut off in the Ti curve, too. Therefore this intermediate layer is excluded from further analysis.

Finally, towards the end of the target layer a steep increase of the concentration of the backing material, tantalum, is found as expected. In addition an average 30 atom% contamination of hydrogen is present, that is not uncommon, as mentioned earlier. It should be noted, that the hydrogen does not stem from the proton irradiation, because not irradiated target areas show about the same H content and the beam energy during the experiment was too high to implant H at the shallow depth of 400 nm.

A different profile is plotted in Fig. 3.5 showing target St-TiN-1 after the irradiation. The initial carbon layer is much bigger then on target Ca-TiN-2 and the TiN layer is about half as thick. This target, produced in a different facility (see Tab. 2.3), did not contain a significant amount of hydrogen although the backing was cut from the same

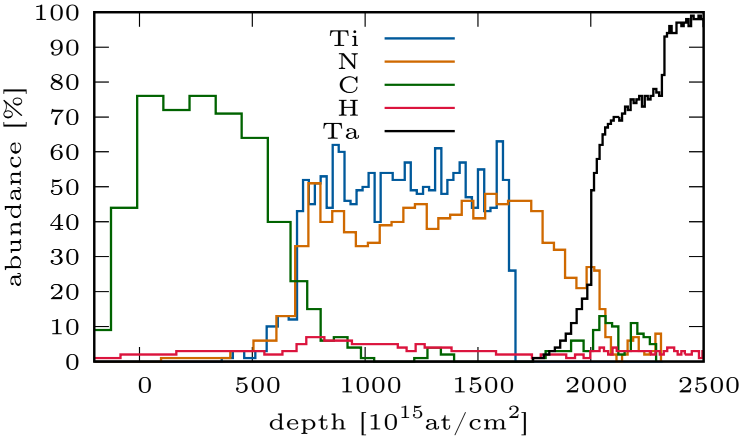

Figure 3.5.: Elemental stoichiometry depth profile of target St-TiN-1. The small (<1 %) Oxygen fraction was not plotted for clarity reasons.

tantalum sheet. But this time no hydrochloric acid was used. This indicates that the H content in Fig. 3.4 stems from the different treatment in the production process. In the end the irradiation measurement with target St-TiN-1 had to be excluded from the results because of the large carbon layer and the strong degradation of the very thin TiN layer as the NRRA showed.

For all the targets, the stoichiometric ratio x, for a compound TiN$_x$, was determined by calculating the average titanium and nitrogen concentrations on their common plateau in the ERD depth profiles. Using the value x the effective stopping power defined in Ref. [Ili07, p. 336, Eq. (4.94)] $\epsilon_{\text{eff}}(897)$ for protons with ^{14}N as the active nucleus was determined:

$$\epsilon_{\text{eff}}^{^{14}\text{N}}(897) = \frac{1}{0.996337}\left[\epsilon_{\text{N}}(897) + \frac{1}{x}\epsilon_{\text{Ti}}(897)\right] \tag{3.7}$$

where $\epsilon_{\text{N}}(897)$ and $\epsilon_{\text{Ti}}(897)$ are the stopping powers for 897 keV protons in solid nitrogen and titanium, respectively. The stopping power values $\epsilon_{\text{N,Ti}}$ are taken from the SRIM software, adopting the SRIM relative uncertainty of 2.9 % for $\epsilon_{\text{N}} = 5.181\,{}^{\text{eV cm}^2}/_{10^{15}\text{ atoms}}$ and 4.4 % for $\epsilon_{\text{Ti}} = 11.091\,{}^{\text{eV cm}^2}/_{10^{15}\text{ atoms}}$ in the c.m. system. The factor 1/0.996337 corrects the effective stopping power for the 99.6337 % isotopic abundance of ^{14}N in natural nitrogen. This abundance has been found to be very stable in air as stated in Ref. [CBd$^+$02] and is conservatively assumed to remain constant with 1 % uncertainty. As already mentioned the results can be found in Tab. 3.2 at the end of this section.

3.2.3. Calculations and corrections for the targets

The stopping power $\epsilon(E_p)$ calculated by ERDA and the energy loss $\Delta E(E_p)$ in the target are both dependent on the initial proton energy E_p and both are needed to calculate the reaction cross sections for the investigated proton energies from 400 to 1400 keV. The target scans show the energy loss only at the resonance energy of 897 keV. But because only the ratio of both quantities is needed for the cross section calculation, the relation

$$\frac{\Delta E(E)}{\epsilon(E)} = n, \tag{3.8}$$

from Ref. [Ili07, p. 336, Eq. (4.92)] can be used. n, the concentration of target nuclei, is a characteristic independent of ion energy E_p and therefore preferred in the cross sections calculations.

However, to calculate the median effective proton energy E_{eff} in the target for a given incident proton beam with energy E_0 the same Ref. states that the energy loss in the target has to be known for this beam energy to calculate

$$E_{\text{eff}} = E_0 - \frac{\Delta E(E_0)}{2}, \tag{3.9}$$

assuming approximately constant cross section and stopping power over the energetic target thickness. To solve this problem the program SRIM was used again to calculate the stopping power of the compound TiN at the different H^+ ion energies. Together with the constant concentration n and Eq. (3.8) the energy dependent target thickness could be calculated and used to correct the proton energy with Eq. (3.9).

The resulting fit parameters of Eq. (3.6) from the NRRA in Sec. 3.2.1 can be used for further calculations of target and beam parameters. The first partial width parameter Γ_1 in this equation is actually a superposition of the total width Γ and the beam spread width Δ_{beam} by

$$\Gamma_1 = \sqrt{\Gamma^2 + \Delta_{\text{beam}}^2}. \tag{3.10}$$

Because the total width is known, as mentioned above, the typical beam spread could be calculated for every scan. With a range of [1.3 ... 2.7] keV and an average of $(1.9\pm0.2)\,\mathrm{keV}$ the beam spread was quite different in the three measurement phases, but this fluctuation of the beam, that depend on the source material, the beam adjustment and the beam energy had to be expected over time. The reason that the right flank in Fig. 3.2 is larger then the left one, is the straggling process of the protons. This adds

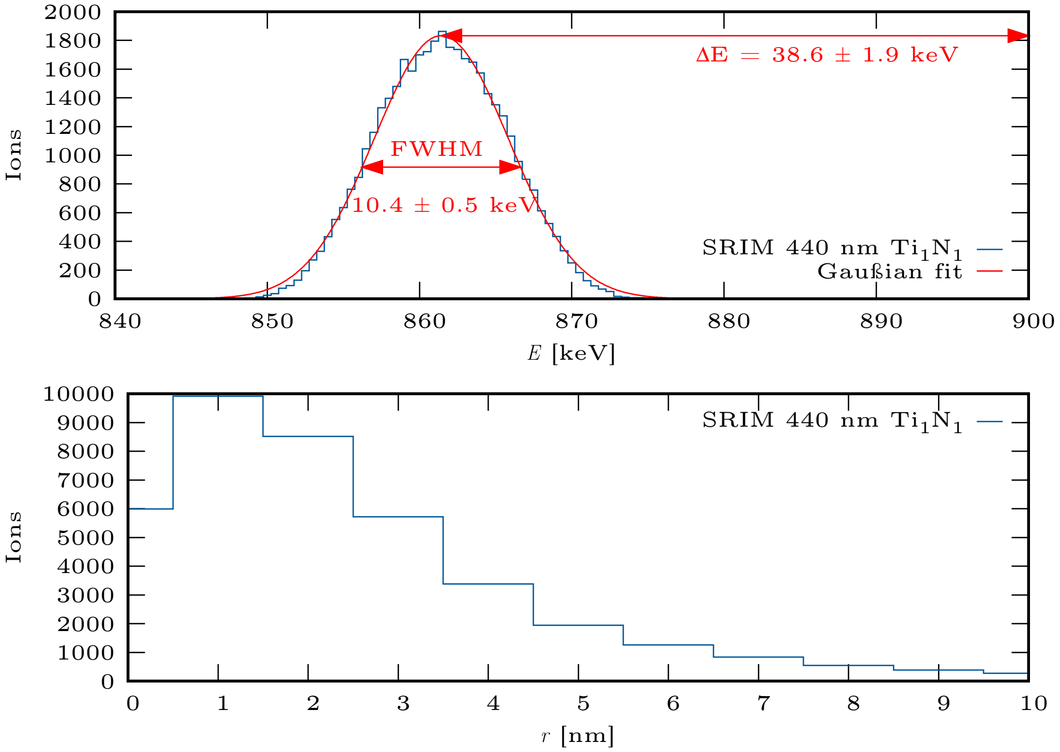

Figure 3.6.: The SRIM simulation for 440 nm TiN of ratio 1 to 1 reproduces the properties of the target scan from target "Ca-TiN-2" ($\Delta E = 38.5 \pm 0.6\,\mathrm{keV}$; $\Gamma_{\mathrm{Stragg}} = 9.6 \pm 1.3\,\mathrm{keV}$) within the uncertainties. The bottom plot underlines that a radial straggling of protons of $r > 7\,\mathrm{nm}$ is fairly unlikely.

to the second partial width parameter Γ_2 and can be calculated by

$$\Delta_{\mathrm{stragg}} = \sqrt{\Gamma_2^2 - \Delta_{\mathrm{beam}}^2 - \Gamma^2} = \sqrt{\Gamma_2^2 - \Gamma_1^2} \tag{3.11}$$

from the difference of the widths. Δ_{stragg} is different for every target because it depends on the target thickness and the stopping power as stated in Ref. [Ili07, p. 346, Eq. (4.120)]. But despite its effect on the shape of the yield curve the FWHM accounting for the target thickness is not affected by the straggling.

To check if the straggling calculation is correct it was compared to a simulation of the energy loss of the proton. For this the software tool SRIM needed the incident proton energy, the target thickness and composition to calculate a large number of ions on their way through the target with the Monte Carlo method.

One problem with the target composition was, that only stopping tables for elements and certain materials are available. But for TiN the program had to calculate them from the elemental ones and assume the standard density of TiN even if the ratio was not one to one. This adds a systematic uncertainty to the straggling, but as Fig. 3.6 shows, the straggling is in the range of the target scan results for the target under investigation (Ca-TiN-2), if the same energetic target thickness is applied in the simulation. The simulated thickness was not the nominal value of Tab. 3.2 because the nominal thickness differs from the measured thickness and the proton beam had an incident angle of 55° increasing the proton path length by a factor of $1/\cos(55°) = 1.74$. This lead to a thickness of 440 nm that corresponds to 38.5 keV proton energy loss.

The second plot of Fig. 3.6 demonstrates that radial straggling is no significant reason for increased proton energy loss in the target. Thus no correction for this effect was necessary.

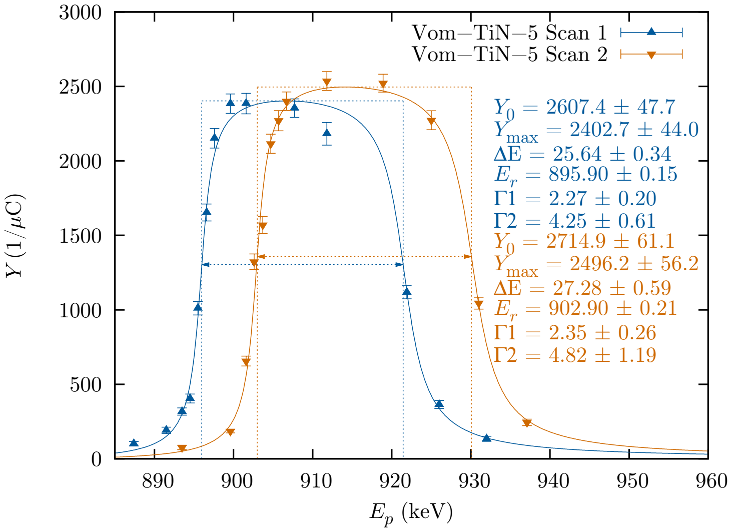

Figure 3.7.: The first and second resonance scan of target Vom-TiN-5 are plotted in blue and orange with their fits to Eq. (3.6) with results of the free parameters. All values except the yield Y have the unit keV.

By comparing consecutive scans of the same target like in Fig. 3.7 sometimes a shift of the rising edge was observed. This edge marks the resonance energy of $E_\mathrm{r} = 897\,\mathrm{keV}$ on a new target but if E_r is higher in later scans, the protons lose energy before they can hit the target layer. This can be explained by a layer on top of the target that is building up during the irradiation process. As mentioned in Sec. 2.1 this effect was stronger before the new pumping procedure was in place because more residual gas was in the target chamber. Because beam current and chamber pressure were not constant during the irradiation, the build up process is nonlinear. Half the resulting energy shift ΔE_shift that was applied to correct the effective proton energy is therefore not necessarily the average shift. To take this into account, the uncertainty in the proton energy was

increased by $\Delta E_{\text{shift}}/2$.
The results of the target scans with all the corrections are summarized in the second part of Tab. 3.2 at the end of this section.
To have a better comparison of the target parameters determined by ERDA and NRRA, the results of Tab. 3.2 are plotted in Fig. 3.8. In addition, the results of fitting a Breit-Wigner function of similar shape like Eq. (3.6) to the peak of direct capture to the ground state and the primary peak of the 6.79 MeV excited state transition in ^{14}N(p,γ)^{15}O are shown, corrected for the γ-ray energy resolution of the detector. The spectra of the analyzed peaks and their fits are plotted in Figs. A.3 and A.4 in the appendix. To determine the proton energy loss in each layer found in the ERDA, additional calculations were necessary. With the following parametric formula from Ref. [AZ77, p. 10 Eq. (17)], the stopping power ϵ in a specific element can be calculated depending on the c.m. energy E of the proton and the target.

$$\epsilon(E) = \frac{a \cdot E^b \cdot \frac{c}{E} \cdot \log(1 + \frac{d}{E} + e \cdot E)}{a \cdot E^b + \frac{c}{E} \cdot \log(1 + \frac{d}{E} + e \cdot E)} \tag{3.12}$$

Eq. (3.12) combines the stopping power approximation from Lindhard, Scharff and Schiott (LSS theory from 1963 in Ref. [LSS63]) for low energies of $E < 30\,\text{keV/u}$ with the description of the high energy range by the Bethe-Bloch formula using a to e as fitting parameters to experimental data. For the elements found in the targets by ERDA the parameters are given in Tab. 3.1.

Table 3.1.: Parameters for Eq. (3.12) fitted from the SRIM software stopping power tables for protons in the different elements found in the targets.

Element	a	b	c	d	e
H	1.28	0.46	302.24	2755.40	0.0397
C	1.96	0.66	1144.51	4.10	0.0571
N	2.78	0.48	2005.95	808.55	0.0124
Ti	5.81	0.44	4513.56	917.33	0.0137

With $\epsilon(E_{\text{p}})$ and the nuclei per target area n from ERDA, Eq. (3.8) gave the energy loss but with adjustment for the 55° incident angle of the protons.

$$\Delta E(\epsilon(E_{\text{p}}),n) = \epsilon(E_{\text{p}}) \cdot \frac{n}{\cos(55^\circ)} \tag{3.13}$$

The NRRA value of ΔE had to be rescaled, in order to be directly comparable to the results of the peak analysis, because the energy loss depends on the initial proton energy.

$$\Delta E(E_\mathrm{p}) = \Delta E(897\,\mathrm{keV}) \cdot \frac{\epsilon(E_\mathrm{p})}{\epsilon(897\,\mathrm{keV})} \tag{3.14}$$

The ratio of the stopping powers in Eq. (3.14) was again calculated with Eq. (3.12). The top panel of Fig. 3.8 shows, that the energy loss in the carbon layer measured by NRRA in general follows the trend of the ERDA results. Eight of 13 data point pairs are comparable within the one sigma uncertainty of 10% for each measurement. For targets St-TiN-1 and Vom-TiN-5 the differences are larger but within 2 sigma uncertainty. Comparing the results of the energy shift calculated from the direct peak fitting approach to the shift from the carbon layer in the ERDA data shows much more scattering and no general trend. In addition, the results from the two analyzed peaks differ by 2 - 4 keV. Because of the discrepancies with two independent methods that give concurring results (ERDA and NRRA) this third and direct method of determining the energy shift is identified to be not as reliable as a separate target analysis and therefore not considered in further analysis of the carbon layer.

The middle panel of Fig. 3.8 shows the thickness of the TiN layer in the targets with the methods described above. The general picture is similar to the data sets of the top panel, meaning the ERDA and NRRA data coincide very well and the direct peak fitting results have higher deviations from the other two methods. However, they differ by less than one standard deviation for the majority of cases. The two outliers of target St-TiN-1 at 640 keV and Vom-TiN-6 at 1301 keV have problems with background peaks interfering with the peak of interest and their special treatment is described in the next section.

The bottom panel of the same figure shows results of target thickness and carbon layer measurements again, but for a closer look on the deviations they are plotted relative to the NRRA results, which would be at 1.0 and are not plotted, therefore. The good congruence between NRRA and ERDA measurements is a strong argument to trust the target characterization with these methods and provides a reliable base for further analysis. For the following calculations the stoichiometry from ERDA and the target thickness from NRRA were used because of the respectively smaller uncertainties.

Table 3.2.: Results of ERDA (first part) on a clean area and on the beam spot and NRRA (second part) before and after irradiation of the targets (calculated in lab system). N_C is the carbon area density, x is the N to Ti ratio, $\epsilon_\mathrm{eff}^{^{14}\mathrm{N}}(897)$ the effective stopping in ^{14}N at $E = 897\,\mathrm{keV}$, E_p the measured resonance energy and ΔE_N the energy loss in the N layer. The E_p-shift is the difference between E_p before and after the irradiation.

general			ERDA		
target	$d_\mathrm{TiN,nom}$ [nm]	area	N_C $[10^{15}\,\frac{\mathrm{atoms}}{\mathrm{cm}^2}]$	x of TiN$_x$	$\epsilon_\mathrm{eff}^{^{14}\mathrm{N}}(897)$ $[10^{-15}\,\frac{\mathrm{eV\cdot cm}^2}{\mathrm{atoms}}]$
Vo-TiN-5	170	clean	-	-	-
		spot	712	0.81	18.89
Vo-TiN-6	170	clean	29	0.73	20.40
		spot	602	0.80	19.12
St-TiN-1	140	clean	84	0.88	17.91
		spot	658	0.83	18.63
St-TiN-5	170	clean	-	-	-
		spot	274	0.87	17.99
Ca-TiN-2	200	clean	79	1.00	16.35
		spot	271	0.97	16.63

general			NRRA		
target	$d_\mathrm{TiN,nom}$ [nm]	status	E_p-shift [keV]	E_p [keV]	ΔE_N [keV]
Vo-TiN-5	170	before		895.9	25.6
		after	9.0	904.9	24.7
Vo-TiN-6	170	before		898.2	25.0
		after	4.2	902.4	24.9
St-TiN-1	140	before		900.3	20.0
		after	3.8	904.2	18.7
St-TiN-5	170	before		902.8	28.3
		after	1.8	904.6	29.1
Ca-TiN-2	200	before		901.8	38.5
		after	2.9	904.7	37.1

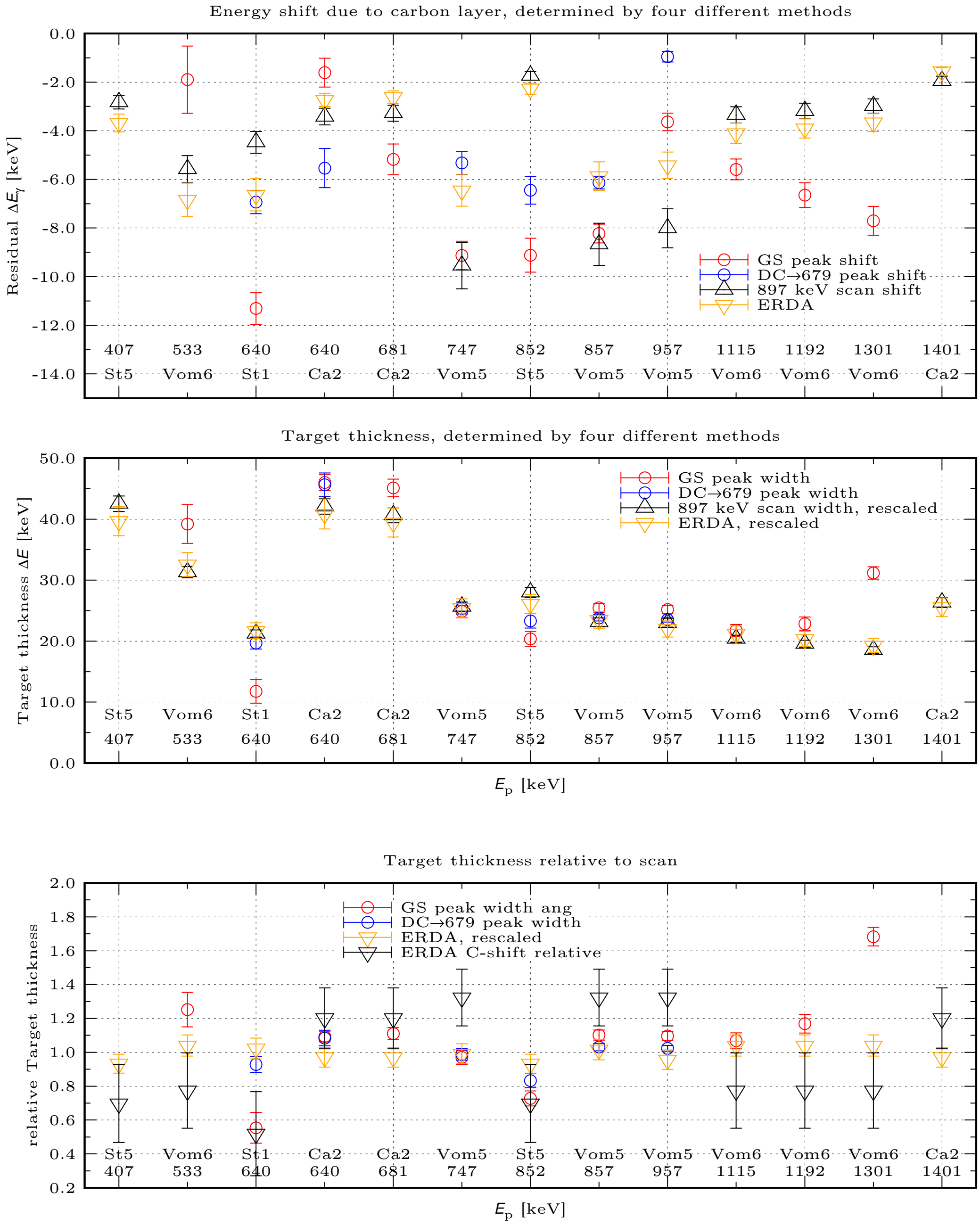

Figure 3.8.: The three panels show the results of the target characterization by different methods. In the top panel the proton energy shift by the carbon layer on the target surface is plotted for each target and energy. In the middle panel the energy loss in the TiN target (target thickness) is shown. The NRRA and ERDA results are rescaled according to the different energies for direct comparison to the peak width analysis. The lowest panel shows the same data but relative to the NRRA scan.

3.3. Irradiation measurements

As a first step the recorded in-beam γ-ray spectra are interpreted for the data analysis (Sec. 3.3.1). Then the efficiency-corrected yields from the two detectors are compared to check the literature data on the angular distribution (Sec. 3.3.2). Finally, the sought after cross section and astrophysical S-factor are determined (Sec. 3.3.3).

3.3.1. Interpretation of the observed γ-ray spectra

Typical in-beam γ-ray spectra taken with the two HPGe detectors are shown in Fig. 3.9 for a representative high beam energy, E_p = 1191 keV, and in Fig. 3.11 for the lowest beam energy, E_p = 407 keV.

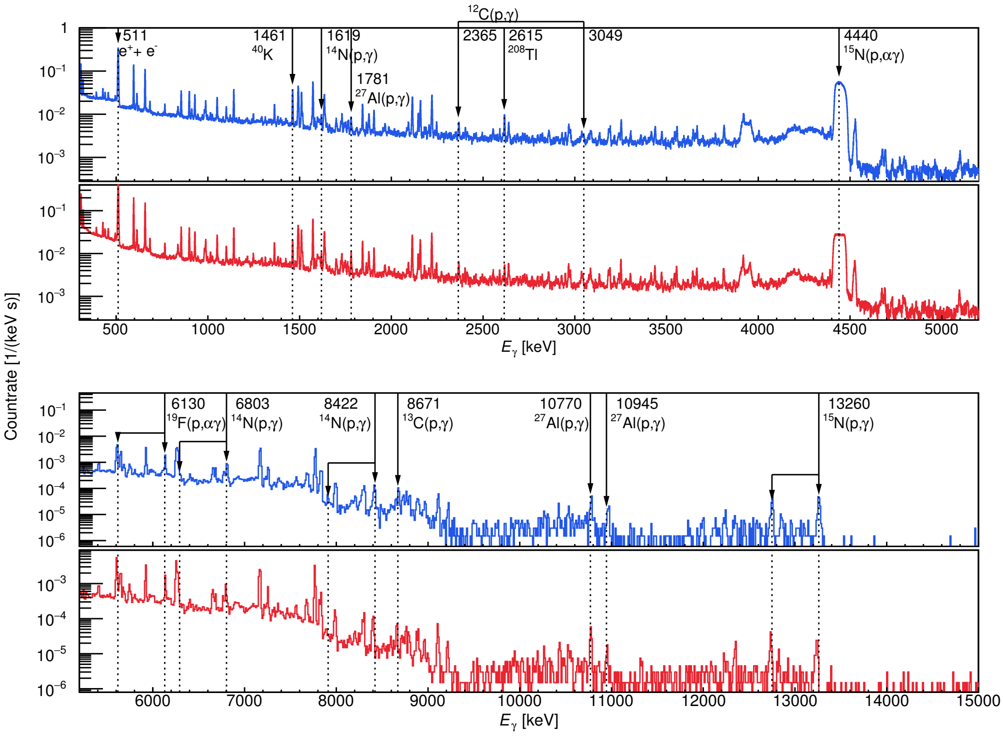

Figure 3.9.: In-beam γ-ray spectrum at E_p = 1191 keV. The irradiation time was 3.7 hours, total accumulated charge 0.21 C. Top, blue spectrum: 55° detector. Bottom, red spectrum: 90° detector.

In the low γ-ray energy part of the 1191 keV spectrum (Fig. 3.9, upper panel), the well-known room background lines at 511, 1461, and 2615 keV are visible. In addition, the primary γ-ray from capture to the 6792 keV level can be seen at 1619 keV, with the typical peak shape shown by the target profile. Somewhat weaker lines from the

^{12}C(p,γ)^{13}N reaction on the initial carbon layer of the target are apparent at 2365 and 3049 keV.

One of the tallest peaks is actually the wide 4439 keV line from ^{15}N(p,$\alpha\gamma$)^{12}C which is used for the monitoring of the irradiation. The yield of the 4439 keV γ-ray from the decay of the first excited state of ^{12}C provided a real time estimate of the state of each target. Fig. 3.10 shows the 4439 keV γ-ray peak yield of target St-TiN-5 at E_p = 407 keV as an example of the target monitoring during long term irradiation. The low fluctuations around the average yield indicate that the N amount in the target stayed the same during the irradiation.

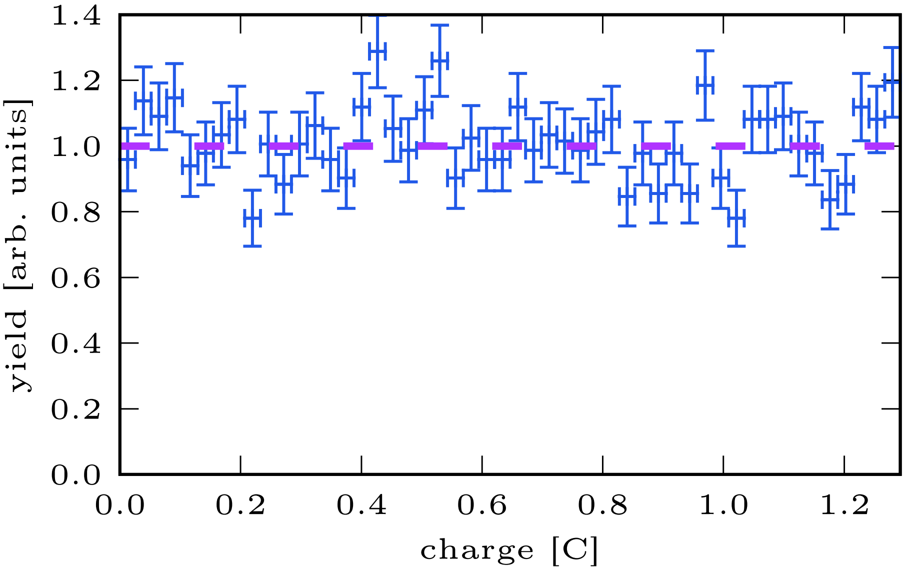

Figure 3.10.: Yield of the 4439 keV γ-ray from the ^{15}N(p,$\alpha\gamma$)^{12}C reaction during a long irradiation of target St-TiN-5 at E_p = 407 keV, as a function of the accumulated charge. The yield is normalized with the average yield value.

The only case where a significant degradation of the 4439 keV yield was observed was target St-TiN-1, with 28 % degradation. This target was then excluded from the analysis to limit the resultant uncertainty. Only runs with 4439 keV yield degradation less than 5 % were adopted for the analysis.

In the high γ-ray energy part of the spectrum (Fig. 3.9, lower panel), a number of parasitic peaks due to the ^{19}F(p,$\alpha\gamma$)^{16}O background reaction are apparent, most problematic at 6130 keV. This peak, which includes both a sharp Gaussian component due to ^{16}O nuclei stopped in the backing and a wide Doppler continuum due to in-flight decay of ^{16}O, is so close to the weak secondary γ-ray from the decay of the 6172 keV excited state in ^{15}O that no analysis of the DC$\rightarrow$6172 transition is attempted in the present work.

Additional γ-lines stem from the ^{13}C(p,γ)^{14}N reaction on the initial carbon layer, from the ^{15}N(p,γ)^{16}O reaction on the 0.4 % ^{15}N content in natural nitrogen, and from the ^{27}Al(p,γ)^{28}Si reaction from beam losses on the target holder. The latter reaction also gives rise to a secondary γ-ray at E_γ = 1779 keV that is populated in a number of strong ^{27}Al(p,γ)^{28}Si resonances. Based on their known strengths and branching ratios from Ref. [MVR75, Bas13], this line is used to put an upper limit of $\leq$ 0.5 % for beam lost on the target holder.

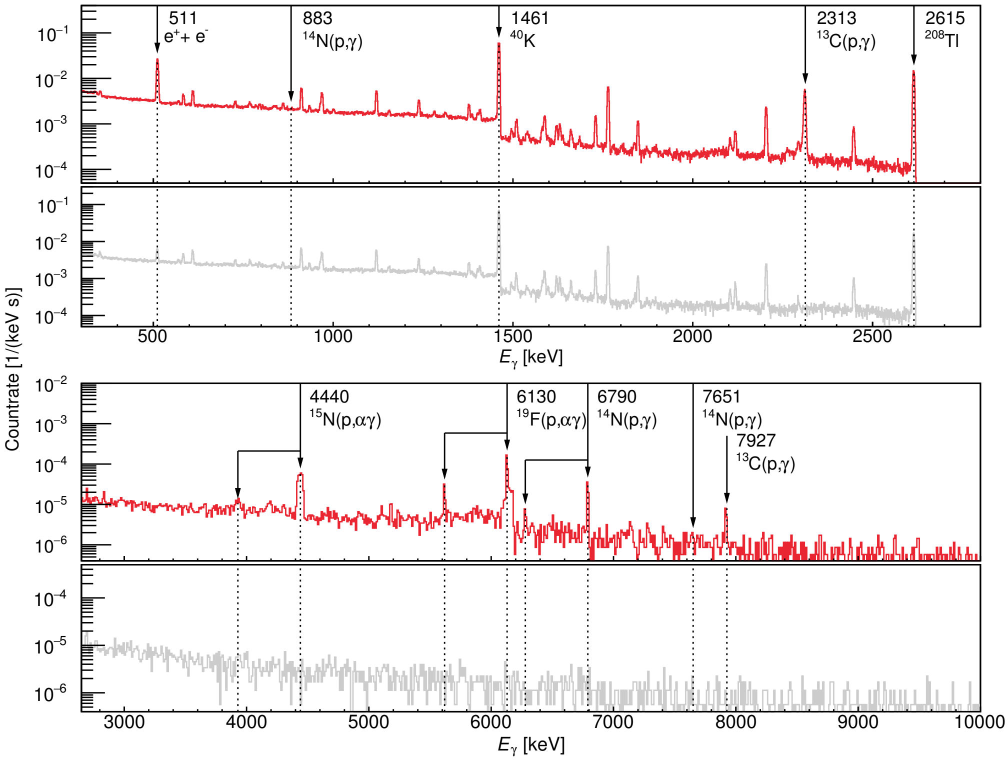

Figure 3.11.: In-beam γ-ray spectrum at E_p = 407 keV, of the 90° detector. The top, red spectrum is the in-beam spectrum with an irradiation time of 97 hours and a total accumulated charge of 1.3 C. The bottom, grey spectrum is the no-beam background, rescaled for equal time.

The three γ-rays used for the analysis are (1) the secondary γ-ray due to the decay of the E_x = 6792 keV excited state in ^{15}O (shown at 6790 keV in Fig. 3.11 due to the recoil correction), (2) the primary γ-ray from capture to the 6792 keV level (seen at 1619 kev in Fig. 3.9) and (3) the primary γ-ray from ground state capture, seen at 7651 keV. These three γ-rays are shown in detail in Figures A.3 and A.4 in the appendix, together with the regions of interest selected for the determination of the peak area and for the estimation of the linear background to be subtracted.

Despite the low counting rate at $E_\mathrm{p} < 0.5\,\mathrm{MeV}$, low-energy runs were undertaken in order to connect the present data to the well-studied low-energy region at E = 300-500 keV shown previously in Fig. 1.4. The γ-ray spectrum from the run with the lowest proton energy is shown in Fig. 3.11.

In the low-energy region the spectrum is entirely dominated by the room background (Fig. 3.11, top panel). The Compton continuum from the room background is strong enough to prevent a meaningful analysis of the primary γ-ray from capture to the 6792 keV level (at E_γ = 883 keV).

The broad 4439 keV peak by the ^{15}N(p,$\alpha\gamma$)^{12}C reaction is again clearly visible in the high-energy part of the spectrum (Fig. 3.11, bottom panel). Of the various ^{19}F(p,$\alpha\gamma$)^{16}O peaks, only the most problematic one at 6130 keV is visible at this low energy. The secondary γ-ray due to the decay of the E_x = 6792 keV excited state in ^{15}O (shown at 6790 keV in Fig. 3.11) is clearly visible. However, at this lowest beam energy, the same is not true for the primary γ-ray from ground state capture, expected at 7651 keV. It coincides with the Compton edge of the 7927 keV peak from the direct capture peak in the ^{13}C(p,γ)^{14}N reaction, preventing an analysis of the ground state transition for this data point.

In several cases special steps had to be taken for the background subtraction as listed in the following text. The respective error bar for each of the data points listed was increased to take the uncertainty from the subtraction procedure into account.

- At E_p = 533 keV, the ground state primary is affected by background due to the 23 keV wide ^{13}C(p,γ)^{14}N resonance at E_p = 551 keV (see Ref. [Ajz91]). In order to treat this background, the shape of the detector response has been simulated by Geant4 and subtracted from the observed spectrum (Fig. 3.12). After subtraction of the Compton edge based on the simulation (60% and 30% of the raw counts for the 55° and 90° detector, respectively), the ground state capture peak clearly emerges, albeit on top of a remaining continuum. The position and width of the peak coincide with what is expected from the resonance scan (Sec. 3.2.1). The error bar for these data points is conservatively increased by 30 % of the subtracted counts.

- At E_p = 1115 keV, there is a γ-ray exactly 511 keV above the 6792 keV secondary, so that its single-escape peak had to be subtracted based on the known single-escape/full-energy peak ratio, giving 16 % correction.

- At E_p = 1301 keV, a γ-ray at 9010 keV lies 511 keV above the ground state primary. This peak is tentatively assigned to the ^{18}O(p,γ)^{19}F reaction. Its single-escape peak had to be subtracted based on the known single-escape to full-energy peak ratio, giving 50 % correction.

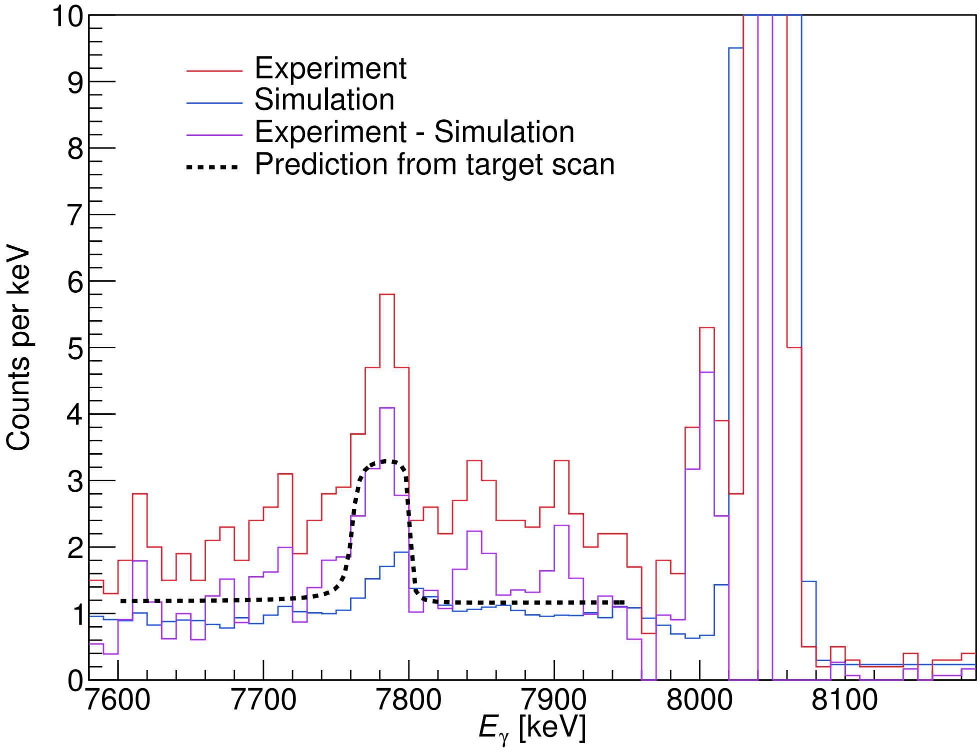

Figure 3.12.: In-beam γ-ray spectrum from the 55° detector for the E_p = 533 keV run near the ground state capture peak. See text for details.

For the ground state (GS) peak, the yield has been corrected down by a part of the measured yield $c_\mathrm{SumIn,GS}$ = 0.4 - 1.5 % for the summing-in effect with Eq. (3.15). The fraction $c_\mathrm{SumIn,GS}$ of the yield are events in the peak area of interest caused by the coincidences between two simultaneous photons fully absorbed in the detector with a summed energy signal.

$$c_\mathrm{SumIn,GS} = \frac{GS_\mathrm{coinc}}{GS} = \frac{\varepsilon(E_\mathrm{prim}) \cdot \varepsilon(E_\mathrm{sec})}{\varepsilon(E_\mathrm{GS})} \cdot \frac{S_{6.79}(E_\mathrm{p})}{S_\mathrm{GS}(E_\mathrm{p})} \tag{3.15}$$

This correction has been estimated based on the γ-ray detection efficiencies $\varepsilon(E_\mathrm{prim})$ and $\varepsilon(E_\mathrm{sec} = 6792\,\mathrm{keV})$ for primary and secondary γ-rays from the 6792 keV state and $\varepsilon(E_\mathrm{GS})$ for the ground state γ-ray and the ratio between the astrophysical S-factors for the 6.79 MeV and ground state transitions. A conservative 20 % relative uncertainty was assumed for the correction. Based on the total γ-ray efficiency from the calibration measurement with the ^{137}Cs source, the summing-out correction for the 6792 keV secondary peak was found to be even lower, always below 0.6 %. This opposite effect reduces events from a peak area of interest, due to coincidence between an absorbed photon of the peak and an absorption of a second simultaneous photon in the detector, again summing both energies in the signal.

Taking the mentioned corrections for the full energy peak counts N_R into account, the experimental yield Y was calculated using

$$Y = \frac{N_R}{W(\Theta) \cdot \varepsilon \cdot Q \cdot \frac{t_L}{t_R}}. \tag{3.16}$$

$W(\Theta)$ is the angular correction factor discussed in the next section. Q denotes the integrated beam current, ε the γ-ray detection efficiency and $\frac{t_L}{t_R}$ the dead time correction.

3.3.2. Angular distribution information

The angular distribution of the off-resonant ^{14}N(p,γ)^{15}O γ-ray yield was measured in a wide energy range in the Bochum experiment and presented in the form of first and second order angular distribution coefficients $a_{1,2}$ in Ref. [SBB$^+$87] for the Legendre polynomials in Eq. (3.17).

$$W(\theta_\gamma) = 1 + a_1 Q_1 P_1(\cos\theta_\gamma) + a_2 Q_2 P_2(\cos\theta_\gamma) + ... \tag{3.17}$$

The distribution $W(\theta_\gamma)$ is cut off after the second Legendre polynomial because higher order corrections were not reported. $Q_{1,2}$ are attenuation factors based on the geometric correction for the finite solid angle of the detector. The Geant4 simulation (Sec. 3.1) showed that, because of the long distances between target and detectors of 15.9 cm and 19.5 cm compared to the crystal diameters (Fig. 2.5), the Q-factors could be set to unity for the present analysis.

Recently, the distribution was re-measured at Notre Dame by Ref. [LGd$^+$16]. The angular data from the two publications are different for the primary γ-rays. For the γ-rays from direct capture to the ground state and to the 6792 keV excited state, Notre Dame reported a non-negligible coefficient for the P_1 Legendre polynomial, which lead to up to 40 % forward-backward asymmetry. Bochum had reported such a forward-backward asymmetry for ground state capture, but not for capture to the primary γ-ray of the 6792 keV excited state. This difference is shown in Fig. 3.13 for the data colored in black. The efficiency-corrected ratio of the yields of the two detectors is consistent with both reported ratios within the uncertainties.

The present data is not very sensitive to the angular distribution. The first-order Legendre polynomial vanishes at 90°,

$$P_1(\cos 90°) = \cos 90° = 0. \tag{3.18}$$

The second-order Legendre polynomial vanishes at 55°,

$$P_2(\cos 55°) = \frac{1}{2}(3\cos 55° - 1) = -0.0065 \approx 0. \tag{3.19}$$

The secondary γ-ray of the 6.79 MeV transition was reported to be isotropic by Bochum and not studied by Notre Dame. The efficiency-corrected ratio of the yields of the two detectors is consistent with this expectation as the red colored data in Fig. 3.13 show. For ground state capture the different reported Legendre coefficients from Bochum and Notre Dame partially cancel out in the yield ratio. The present data are in fair agreement with the yield ratio expected based on these works as the blue colored data in Fig. 3.13 demonstrate. The ground state capture data points at E = 480 keV however have such low statistics (∼ 40 % stat. uncertainty each), that their ratio fits

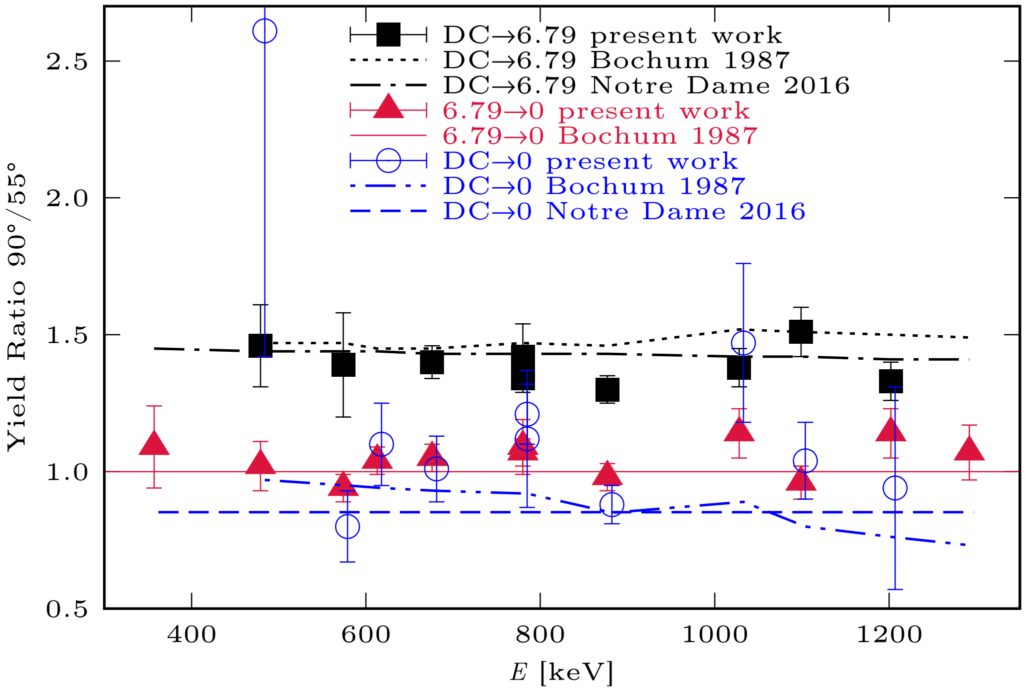

Figure 3.13.: Ratio of the efficiency-corrected γ-ray yields from the 90° and 55° detectors from the present work, compared with previous results from Bochum in Ref. [SBB$^+$87] and Notre Dame in Ref. [LGd$^+$16].

any expectation within the large uncertainty. On the other hand the data point just above the E = 987 keV resonance is an outlier for ground state capture, possibly due to some residual contribution by the resonance.

For the data analysis no angular correction is made for the 6.79 MeV secondary γ-ray. For the primary γ-ray to the 6.79 MeV level the data are corrected with the measured angular coefficients by the recent Notre Dame experiment in Ref. [LGd^{+}16]. For the ground state primary γ-ray the previous coefficients from the Bochum experiment in Ref. [SBB^{+}87] are used instead. They are consistent with Notre Dame and more easily accessible in the paper.

3.3.3. Determination of the cross section and astrophysical S-factor

The experimentally observed yield $Y(E_\mathrm{p})$ and the sought after cross section are connected by the following relation:

$$Y(E_\mathrm{p}) = \int_{E_\mathrm{p}-\Delta E_\mathrm{p}}^{E_\mathrm{p}} \frac{\sigma(E_\mathrm{lab})}{\epsilon^{14}_\mathrm{eff}(E_\mathrm{lab})} dE_\mathrm{lab} \tag{3.20}$$

It was checked if a numerical integration of Eq. (3.20) was really necessary, because an analytical approach would reduce the complexity of further analysis. If the cross section and the effective stopping power are not varying significantly over the energetic target thickness one can replace the dependence of σ and ϵ from E_lab in Eq. (3.20) with the constant effective energy E_eff, that was defined as the median energy of the integrand in Ref. [RR88].

$$E_\mathrm{eff} = E_\mathrm{p} - \frac{\Delta E_\mathrm{p}}{2} \tag{3.21}$$

The proton beam energy E_p in Eq. (3.21) was corrected for energy loss in the initial carbon layer (Sec. 3.2.1), where necessary. The integral of Eq. (3.20) resolves in the described case to

$$Y(E_\mathrm{eff}) = \frac{\sigma(E_\mathrm{eff}) \cdot \Delta E_\mathrm{p}}{\epsilon^{14}_\mathrm{eff}(E_\mathrm{eff})}. \tag{3.22}$$

In Fig. 3.14 the numerical integration was done for the measurement at E_p = 640 keV with target Ca-TiN-2. The left panel shows the stoichiometry measured by ERDA. This was used to divide the target into thin layers with depth dependent ratios of Ti and N. The right diagram shows the yield of the capture to the 6.79 MeV excited state of the ^{14}N(p,γ)^{15}O reaction. The yield is calculated in each layer separately to solve Eq. (3.20) numerically by assuming a flat S-factor of 1 keV b and an effective stopping from ERDA with Eq. (3.7). The S-factor in the title of the plot was calculated from the quotient of the experimental yield (Eq. (3.16)) and the yield summed over all layers

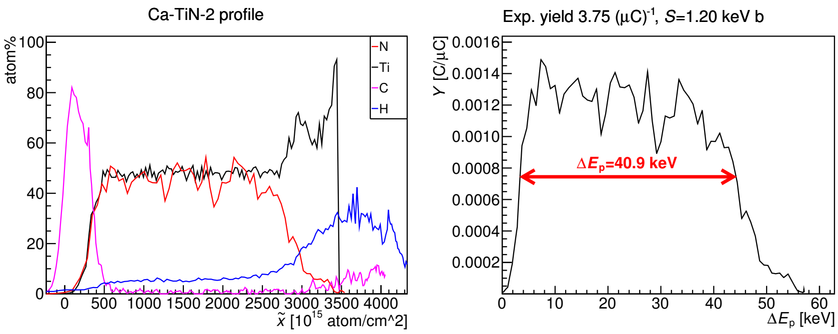

Figure 3.14.: The ^{14}N(p,γ)^{15}O yield (right panel) using the depth dependent Ca-TiN-2 target stoichiometry from ERDA (left panel). The S-factor is the ratio of the experimental yield and the yield sum of all layers. The initial proton beam energy was $E_\text{p} = 597$ keV and the average energy loss was 40.9 keV.

(Eq. (3.20)) multiplied by 1 keV b from the flat S-factor assumption. The yield curve in Fig. 3.14 depends by necessity on the assumed shape of the S-factor curve. There for the calculation was repeated with the Solar Fusion II (SFII, Ref. [AGR$^+$11]) S-factor curve, showing differences of $< 1\,\%$ in the final S-factor.

The resulting S-factor is equal to the experimental S-factor calculated with Eq. (3.22) and Eq. (3.23) $S_{6.79}(E) = (1.17 \pm 0.04_\text{stat})$ keV b within the statistical uncertainties. This assures that no systematic error is introduced by using Eq. (3.22). Ca-TiN-2 at E_p = 640 keV was chosen, because it was the thickest target in the experiment and the energy was one of the lowest. At those two conditions the effect on the S-factor from varying cross-section and effective stopping over the target thickness is the strongest. Since no considerable effect was found, it is safe to assume the other data points are not affected as well. Thus, the S-factor could be calculated using Eq. (3.22) solved for $\sigma(E_\text{eff})$ and the following equation:

$$S(E_\text{eff}) = \sigma(E_\text{eff}) \cdot E_\text{eff} \cdot \hat{T}. \tag{3.23}$$

The Gamow factor $\hat{T}$ in Eq. (3.23) was computed with

$$\hat{T}(E) = \exp\left(\frac{2\pi}{\hbar}\sqrt{\frac{m}{2E}} Z_0 Z_1 e^2\right) \equiv e^{2\pi\eta(E)} \tag{3.24}$$

using the Sommerfeld parameter η with the equation

$$2\pi\eta(E) = 0.989534 Z_0 Z_1 \sqrt{\frac{M_0 M_1}{M_0 + M_1}\frac{1}{E}}, \tag{3.25}$$

where the relative atomic masses M_i are in units of u and the energy E is in MeV according to Ref. [Ili07, p. 107, Eq. (2.126)]. $Z_0 = 1$ and $Z_1 = 7$ are the charge numbers of H^{1+} and N^{7+}. The final astrophysical S-factor values are summarized in Tab. 3.3.

Table 3.3.: $^{14}N(p,\gamma)^{15}O$ S-factors for capture to the 6.79 MeV excited state and for capture to the ground state in ^{15}O, as a function of the effective energy $E_{\text{c.m.}}$ in c.m. system.

$E_{\text{c.m.}}$ [keV]	$S_{6.79}(E_{\text{c.m.}})$ [keV b]	$\Delta S^{\text{stat}}_{6.79}$ [keV b]	$S_{\text{gs}}(E_{\text{c.m.}})$ [keV b]	$\Delta S^{\text{stat}}_{\text{GS}}$ [keV b]
357	1.27	0.10	-	-
479	1.12	0.07	0.19	0.07
574	1.17	0.04	0.26	0.02
613	1.05	0.05	0.22	0.02
676	1.14	0.04	0.24	0.02
780	1.00	0.04	0.26	0.03
780	1.07	0.03	0.31	0.03
877	1.06	0.03	0.42	0.02
1028	1.17	0.05	0.30	0.05
1099	1.23	0.04	0.29	0.03
1202	1.21	0.07	0.23	0.05
1292	1.15	0.07	-	-

3.3.4. Uncertainties

The uncertainties of the present data points (Tab. 3.4) are divided in two groups: The first group (systematic uncertainties) are scale factors that would, at least in principle, affect all the present data points uniformly. The second group (statistical uncertainties) affects each data point randomly and may thus have a different sign for each data point. Only the latter uncertainties should be used when for example gauging the appropriateness of an R-matrix fit as in Sec. 4.3. The former uncertainties will then determine the additional scaling uncertainty of the fit result.

The largest systematic uncertainty, 6 %, stems from the determination of the target composition, here expressed as the effective stopping power, by the ERDA technique (Sec. 3.2.2). This determination is made separately for each target studied here, using one and the same beam, detectors, and analysis method. Therefore it is conservatively assumed that the ERDA uncertainty has a scale factor component of 6 % common to all data points (due to the calibration of the ERD apparatus used) and a statistical component that is target dependent of 5 %. The γ-ray detection efficiency contributes 3 % error (Sec. 3.1). The 5 % uncertainty due to the angular corrections in Sec. 3.3.2 is estimated based on the analysis of the yield ratios shown in Fig. 3.13. The beam current is conservatively approximated to be known with 1 % uncertainty, due to remaining imperfections of the Faraday cup used (see Sec. 2.3.3).

The beam energy calibration affects the conversion of the measured yield to the astrophysical S-factor. The systematic uncertainties are always at 0.06 % or less (Sec. 2.1) and therefore are left out of the table. The statistical uncertainty of the effective energy stems mainly from the energy correction based on the loss in the carbon layer discussed in Sec. 3.2.3. Propagating the systematic uncertainty through Eq. (3.24) increased it particularly in the low energy region to up to 2.7 %.

The 20 % relative uncertainty of the summing corrections (Sec. 3.3.1) resulted in additional count rate uncertainties always below 0.3 % and are hence omitted in the table.

The energetic target thickness is determined by the resonance scans of the target, and its uncertainty mainly stems from the statistical error of the fit curve obtained, meaning it has to be treated like a statistical uncertainty contributing up to 3 % error.

The main statistical uncertainty originates from the γ-ray counting statistics and from the background subtraction, where applicable. For the 6.79 MeV transition, the statistical uncertainty is between 3 % and 10 %. For the ground state transition, due to the lower statistics, higher uncertainties of typically 5-18 % are found.

There are two cases with higher statistical uncertainty in the ground state transition: At

Table 3.4.: Error budget for the astrophysical S-factor, in percent. See text for the E = 479 keV and 1202 keV data points and for further details.

Uncertainty	syst. [%]	stat. [%]
Effective stopping power (Sec. 3.2.2)	6	5
γ-ray detection efficiency (Sec. 3.1)	3	
Angular correction (Sec. 3.3.2)	5	
Beam current (Sec. 2.3.3)	1	
Effective beam energy E (Sec. 3.2.3)		0.3 - 3
Energetic target thickness ΔE_{p} (Sec. 3.2.1)		3
Count rate, ground state (Sec. 3.3.1)		5 - 18
Count rate, 6.79 MeV (Sec. 3.3.1)		3 - 10
Total, ground state	8	6 - 17
Total, 6.79 MeV	8	3 - 8

E = 479 keV (E_p = 533 keV) where the ion beam induced background subtraction plays a major role, for the ground state primary γ-ray a statistical error bar of 37% (28%) is found in the 55° (90°) detector, leading to a total statistical uncertainty of 36 % for the weighted average of the two, taking the uncertainties in the angular correction into account. The second case is E = 1202 keV with the subtraction of a single-escape line leading to a statistical uncertainty of 20 % in the weighted average.

4. R-matrix analysis

In order to estimate their impact on the low-energy extrapolated S-factor, the present data were included in a limited but detailed R-matrix fit, using the AZURE2 code of Ref. [AU$^+$10b]. Instead of a full R-matrix fit like in other recent Refs. [AGR$^+$11, LGd$^+$16, AU$^+$10b], the new fit concentrated on the influence of the new data on key parameters in the R-matrix framework of the ^{14}N(p,γ)^{15}O reaction.
The first section provides a brief introduction about R-matrix theory. This is followed by Sec. 4.2 dealing with the selection of data sets and parameters. Finally, the performed R-matrix fits and extrapolations are described in Sec. 4.3.

4.1. The phenomenological R-matrix

First introduced by Wigner and Eisenbud in 1947 [WE47] to describe resonances in nuclear reactions, the R-matrix theory became a powerful tool for parametrizing cross sections of reactions and scattering of particle systems that can consist of nucleons, nuclei, electrons, atoms or molecules. The theory accounts for interference effects between multiple resonances and nonresonant contributions and is therefore even valid in great distance to resonances.
According to Ref. [WE47] the main idea of the theory is to separate the configuration space of a system into an internal and external region with a boundary between the regions called the channel radius a (sometimes also R). Ref. [DB10] states that, if a is chosen large enough, the external part of the system interacts only by long-range forces that are Coulomb interactions. Therefore, the scattering wave functions can be approximated by asymptotic expressions. Only energy, mass, charge and angular momentum of the couple of particles interacting are needed for the description of this system. The resulting wave functions are called channels. The internal region, on the other hand, is described by many-body nuclear physics with eigenstates. They can be calculated because they form a discrete basis in the confined system, labeled as poles. Then the scattering wave function for an arbitrary energy can be expanded over the internal region. The eponymous R-matrix is the inverse of the logarithmic derivative of the wave function, calculated at the boundary. A match with the solution and derivative

of the external region wave function provides the scattering matrix and the bound states of the system.
In Ref. [DB10] it is also mentioned, that the R-matrix theory was developed in two branches. One approach has the aim to solve the Schrödinger equation for coupled channel problems in a simplified and efficient way and is called the calculable or computational R-matrix. The other part follows the original idea of parametrizing resonances and non-resonant parts of low energy cross sections with a limited number of real parameters with physical meaning. This branch is called the phenomenological R-matrix and is the basis of the cross section fits in this chapter. Provided with the adequate program even a multi channel system is rather easy to handle with this R-matrix framework for the end-user. For a comprehensive overview of R-matrix theory one may refer to Ref. [LT58] or the more recent update in Ref. [DB10].
The AZURE2 program described in Ref. [AU$^+$10b] that was used in this work, provides the option to include additional poles, not related to real resonances. Such poles placed at very high level energies and with very broad resonance widths are called background poles (BGP). They simulate a slowly varying offset in the cross section, induced by a non-resonant mechanism. For the ^{14}N(p,γ)^{15}O system such poles were considered by some groups like in Refs. [AU$^+$10b, AGR$^+$11, LGd$^+$16] to account for the strong background contribution of possible unidentified resonances at higher energies.
It should be noted that the R-matrix framework in the phenomenological treatment is not close to a first principles description of physical reality like the *ab initio* calculations in Ref. [ELR$^+$15] but rather a model using a number of assumptions and parameters. Therefore, generally speaking constraints such as elastic scattering and angular distributions should not be used as justification to accept fits that do not track the experimental radiative-capture data. In the past, these secondary observables have been found useful to constrain R-matrix fits like in Refs. [AU$^+$10b, LGd$^+$16]. However, they have no direct bearing on the astrophysically relevant quantity sought here, i.e. the thermonuclear reaction rate that depends on the low energy reaction cross section.

4.2. Datasets, energy levels and starting values

This focus meant in particular that no elastic scattering data from Ref. [dBG$^+$15] are included and angular distribution data (from Refs. [SBB$^+$87, LGd$^+$16]) are only used to correct the absolute cross section as discussed in Sec. 3.3.2, not for the R-matrix fit itself. The present fit makes no attempt to reproduce these secondary observables, and therefore it serves mainly as an illustration of the possible effects of the present new data on the extrapolated cross section at low energy. The fit is limited to those quantities that are expected to have an effect on either the normalization or the slope of the non-resonant S-factor curve, or on both: The asymptotic normalization coefficient (ANC) of the 6.79 MeV level and the widths of the so-called background poles.

The selection and renormalization of cross section data included in the fit routine follows the approach of the review Solar Fusion cross sections II (SFII, Ref. [AGR$^+$11]). The LUNA data from 2004-2005 in Ref. [FIC$^+$04, ICF$^+$05] were renormalized to the SFII recommended strength of the 259 keV resonance in ^{14}N(p,γ)^{15}O $\omega\gamma_{259} = 13.1 \pm 0.6$ meV, resulting in a scale factor of 1.02. The TUNL data set of Ref. [RCA$^+$05] from 2005 was scaled by a factor of 0.97 in the same way. The more recent LUNA data from 2008-2011 in Ref. [MFG$^+$08, MFB$^+$11] needed no scaling because they already use the recommended strength. The present data are included without normalization, as they do not depend on the strength of the 259 keV resonance. For all data sets, S-factor values close to sharp resonances determined by their energy being between $E_R - 20\Gamma$ and $E_R + 1.5\Delta$ with a target thickness Δ = 30 keV, were excluded. This is the same criterion as in SFII, in order to limit the impact of S-factors above 10 keV b, where the generally low energy uncertainty may lead to significant deviations from the fit curve because. The corrected Bochum data of Ref. [SBB$^+$87] from 1987 were used in SFII (scaled by 0.91) but here they were only taken into account in preliminary R-matrix fits to check if the shape of the high energy resonances in the ground state are correctly reproduced with the fit. Those data were then excluded for the final fit of the ANC of the 6.79 MeV level because of the before mentioned (Sec. 1.3) summing problems and renormalization that made them unreliable for an S-factor extrapolation to zero energy. Instead they are replaced by the present new data. In Tab. 4.1 an overview of the relevant data sets is shown.

Table 4.1.: Summary of experimental data sets used in the R-matrix fits. The number of data points is the sum from direct capture to the ground state as well as capture to the 6.79 MeV excited state. See text for details. Energy range in c.m.

Experiment	Energy range [keV]	Number of data points	Scaling factor	Reference
LUNA 2004-2005	119-393	33	1.02	[MFG$^+$08, MFB$^+$11]
LUNA 2008-2011	315-354	6	1.00	[MFG$^+$08, MFB$^+$11]
TUNL 2005	134-782	50	0.97	[RCA$^+$05]
Bochum 1987	181-3346	168	0.92	[SBB$^+$87]
present data	383-1385	22	1.00	Tab. 3.3

It has been demonstrated previously in Ref. [MdD$^+$14] that the AZURE2 code used here gives similar results to the Descouvemont code of Ref. [DB10] used in Refs. [AD01, FIC$^+$04, ICF$^+$05, MFG$^+$08, MFB$^+$11, AGR$^+$11].

The parameters that are kept fixed in the present multi-channel R-matrix fit are discussed below.

First, in the present fit the very low channel radius of 4.2 fm used previously to fit ^{14}N(p,p)^{14}N scattering data by Notre Dame in Ref. [dBG$^+$15] was tested here. But since it led to an imaginary number for the external partial width of the background pole with $J = \frac{5}{2}^-$, this attempt was discarded. Instead a channel radius of a = 5.5 fm was used (the same radius as in SFII and other studies of Refs. [AGR$^+$11, MFG$^+$08, RCA$^+$05, ICF$^+$05, LGd$^+$16]), which led to a real number for the background pole width and improved χ^2 by 12 %.

Second, the asymptotic normalization coefficients for ground state capture by Mukhamedzhanov from Ref. [MBB$^+$03] are used here. They originate from calculations using the transfer reaction ^{14}N(^{3}He,d)^{15}O. Converted to the AZURE2 coupling scheme that is defined in Ref. [AU$^+$10b] they are the following: $C_{p,1/2}$ = (0.23 ± 0.01) $1/\mathrm{fm}^2$ and $C_{p,3/2}$ = (7.3 ± 0.4) $1/\mathrm{fm}^2$. For the latter value, SFII and Notre Dame in Ref. [LGd$^+$16] use a slightly higher value of (7.4 ± 0.5) $1/\mathrm{fm}^2$.

Third, level energies up to 9.5 MeV are taken from the Ajzenberg-Selove evaluation in Ref. [Ajz91], except where updated by LUNA in Ref. [ICF$^+$05] and kept fixed in the fit. This is different from Notre Dame, where Ajzenberg-Selove energies are used, with level energies above 7.56 MeV being allowed to vary in the fit.

Fourth, in order to preserve the information contained in the S-factor values close to sharp resonances (which are excluded from the fit for the reasons given above), some parameters of the strong 259 keV resonance are kept fixed. Namely, they are the proton width and partial, internal γ-ray widths for decay to the ground state and 6.79 MeV excited state. The measured branching ratios in Ref. [MFB$^+$11] can be converted to partial resonance widths using the resonance strength $\omega\gamma$ = 13.1 meV, recommended by SFII and Eq. (4.1) adapted from Ref. [Ili07, p.192-195] for the special case of $\Gamma_p \gg \Gamma_\gamma$,

$$\omega\gamma \approx \omega\Gamma_\gamma \equiv \frac{(2J^\pi + 1) \cdot (1 + \delta_{01})}{(2j_0 + 1) \cdot (2j_1 + 1)} \Gamma_\gamma. \tag{4.1}$$

Here $J^\pi = \frac{1}{2}^+$ is the spin of the resonance, $j_0 = 1^+$ is the ^{14}N target spin, $j_1 = \frac{1}{2}^+$ is the H$^+$ projectile spin and δ_{01} is zero because the particles in the entrance channel are different. By solving Eq. (4.1) for the total γ-width Γ_γ and computing $\omega = 3$ one can calculate the product of the total γ-width times the branching ratio of a transition to get the partial resonance width of this transition. The values are Γ_p^{259} = 1.12 keV from Ref. [BLUB09], $\Gamma_{\gamma,0}^{259}$ = 0.59 meV and $\Gamma_{\gamma,6.79}^{259}$ = 8.88 meV from the corresponding branching ratios in Ref. [MFB$^+$11, Tab. IV].

These parameters are close to the Notre Dame fit values (see Tab. II in Ref. [LGd$^+$16]), but they have an experimental origin. In addition one can compare the ratio of the resonance widths $\frac{\Gamma_{\gamma,6792}(259)}{\Gamma_{\gamma,0}(259)} = 15.1$ in the present fit with the recent measurement of the 259 keV resonance in Ref. [DKC$^+$16]. Among others, updated branching ratios of 1.5 % for the transition to the ground state and 23 % for the transition to the 6.79 MeV state were reported. The quotient of those branching ratios is 15.3 and this is apparently very similar to the present parameter ratio. This independent experimental reference point, if compared to the lower quotient of parameters from Ref. [LGd$^+$16] $\frac{\Gamma_{\gamma,6792}(259)}{\Gamma_{\gamma,0}(259)} = 14.3$, was a good argument, not to use the parameters from the Notre Dame fit in this case. The decision was confirmed by the 5 % better χ^2 in the fit, if the Notre Dame parameters were not used for the partial resonance widths.

On the other hand, for the resonances at 0.987 and 2.206 MeV, values from the Notre Dame fit were sufficient to act as starting values for the fit procedure. Only minor parameter variations in the preliminary single channel R-matrix fits were observed.

For easier reference, all the R-matrix parameters that have been changed with respect to Ref. [LGd$^+$16] are listed in Tab. 4.2 and it is shown if they originate from Refs. [MBB$^+$03] or [MFB$^+$11].

4.3. Multi-channel R-matrix analysis

In the preliminary single channel fits the chosen parameters for sub threshold level ANC's and partial resonance widths were sufficient to reproduce the resonance data for the ground state and the 6.79 MeV state. But the unfixed parameters for the 987 and 2187 keV resonances converged to slightly different values than the Notre Dame fit in Ref. [LGd$^+$16].

This might stem from the modification to the AZURE2 code that the Notre Dame group did in order to include the differential elastic scattering cross sections of Ref. [dBG$^+$15] measured relative to the cross sections at 30°. In order to ensure the reproducibility of the calculation, in the new fit the AZURE2 code was used as provided by the authors at their web page [AU$^+$10a] and therefore no relative cross sections could be included. That and the use of integrated instead of differential cross section data for the fit can explain the small deviations of $E_{x,\frac{3}{2}^+}$, $\Gamma_p(2187)$ and $\Gamma_{\gamma,0}(\mathrm{BGP}, \frac{3}{2}^+)$ from Ref. [LGd$^+$16] in Tab. 4.2. However, because the off resonance data were not close to the calculated

Table 4.2.: Summary of parameters used in the present R-matrix fit compared to values from fits in literature. See text for details.

	Present work	Ref. [LGd$^+$16]	Ref. [MBB$^+$03]	Ref. [MFB$^+$11]
a	5.5 fm	5.5 fm	5.5 fm	5.5 fm
$C_{p,1/2}$	0.23 $^1/_{\mathrm{fm}^2}$	0.23 $^1/_{\mathrm{fm}^2}$	0.23 $^1/_{\mathrm{fm}^2}$	-
$C_{p,3/2}$	7.3 $^1/_{\mathrm{fm}^2}$	7.4 $^1/_{\mathrm{fm}^2}$	7.3 $^1/_{\mathrm{fm}^2}$	-
$E_{x,1/2+}$	5180.8 keV	5183.0 keV	5183 keV	5180.8 keV
$E_{x,3/2-}$	6172.3 keV	6176.3 keV	6176.3 keV	6172.3 keV
$E_{x,3/2+}$	6791.7 keV	6793.1 keV	6793.1 keV	6791.7 keV
$\Gamma_p(259)$	1.12 keV	0.96 keV	-	1.12 keV
$\Gamma_{\gamma,0}(259)$	0.59 meV	0.65 meV	-	0.59 meV
$\Gamma_{\gamma,6792}(259)$	8.88 meV	9.3 meV	-	8.88 meV
$E_{x,3/2+}$	8289 keV	8285 keV	8284 keV	8284 keV
$\Gamma_p(2187)$	71 keV	89 keV	-	-
$\Gamma_{\gamma,0}(\mathrm{BGP}, \frac{3}{2}^+)$	460 eV	220 eV	-	-
$\Gamma_{\gamma,0}(\mathrm{BGP}, \frac{5}{2}^-)$	716 eV	-	-	-

curves, additional fitting and introduction of additional BGPs was necessary.

At first the channel radius value from Ref. [dBG$^+$15] a = 4.2 fm was chosen for the multi-channel fit as mentioned before. In the fit the $J^\pi = \frac{5}{2}^-$ background pole evolved to values, where the external partial width E1 would become imaginary and thus being ignored by the fit routine. Increasing the radius to 5.5 fm, as recommended for R-matrix fits of ^{14}N(p,γ)^{15}O in Ref. [AGR$^+$11], solved the problem with imaginary widths and reduced the total χ^2 by 12 %. Larger channel radii could not improve the χ^2 for the chosen data set any more but had problems reproducing the high energy ground state data from Bochum in Ref. [SBB$^+$87].

The new multi-channel fit with a = 5.5 fm lead to similar χ^2 for a big region in parameter space as Fig. **??** demonstrates. A similar behavior was seen before with the lower channel radius. The fit routine of AZURE2 minimizes the residuals with the method of the least squares. This means the fit result has the lowest chi-square $\chi^2_{\mathrm{min}} = 1487$ and a region in parameter space can be defined, that has the 99.73 % = 3σ confidence interval of containing the true parameters. According to Ref. [PTVF07, p. 815] for three fitted parameters this 3σ confidence region corresponds to parameter values with a chi-square up to $\Delta\chi^2 = 14.2$ larger then χ^2_{min}. In Fig. **??** this region is marked by the larger dots that are color coded with the corresponding χ^2 value.

To get an estimate for the statistical uncertainty of the S-factor extrapolated to zero

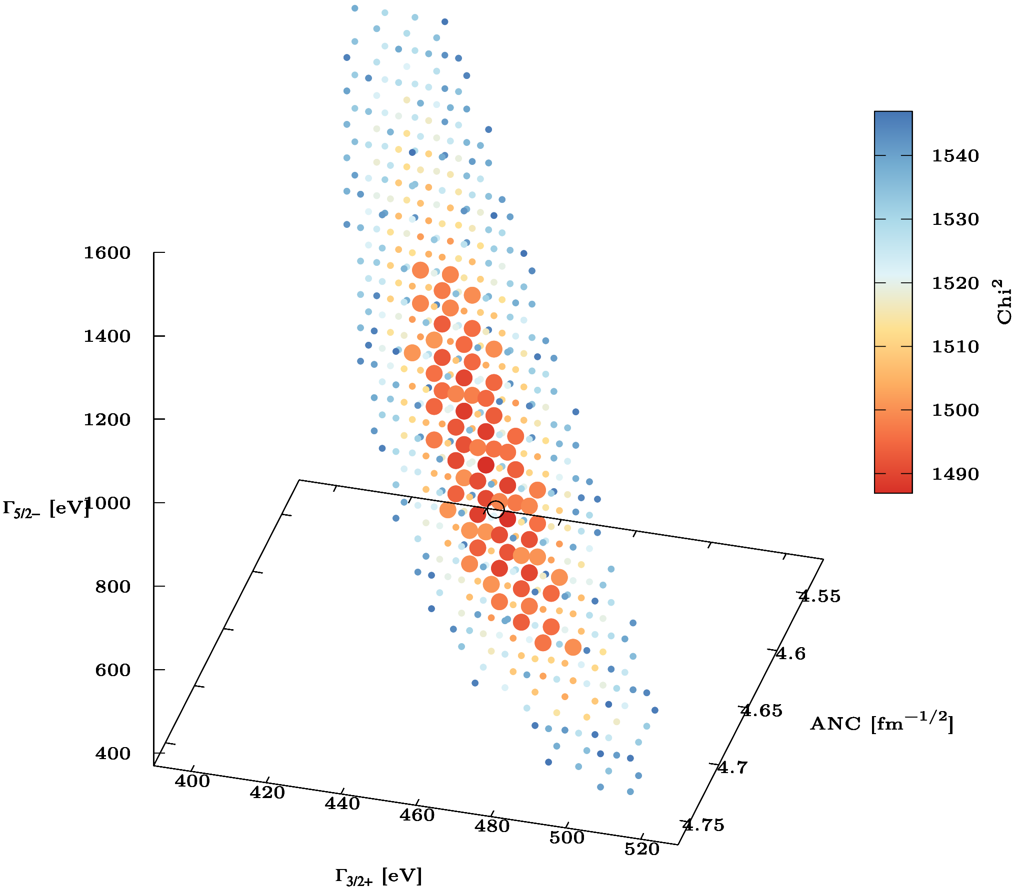

Figure 4.1.: The χ^2 dependence on the three varied parameters with channel radius $a = 5.5$ fm. At the x-axis the ANC of the 6.79 MeV level, at the y-axis the E1 partial width of the $J^\pi = \frac{3}{2}^+$ background pole and at the z-axis the E1 partial width of the $J^\pi = \frac{5}{2}^-$ background pole is drawn. The larger dots in the three dimensional parameter space mark the 3 sigma region of the lowest χ^2. The black circle marks the best fit value of $\chi^2_{\text{min}} = 1486.8$ for the parameters of ANC = 4.64 $^1/_{\text{fm}^2}$ ± 0.4 %, $\Gamma_{3/2+}$ = 461 keV ± 3 % and $\Gamma_{5/2-}$ = 716 keV ± 22 %.

energy, the lowest and highest extrapolated $S_{6.79}(0)$ = (1.163 ... 1.200) kev b from parameters in this $\Delta\chi^2$ confidence region are chosen to calculate the difference to $S_{6.79}(0) = 1.186^{+0.015}_{-0.022}$ kev b from the best fit. The $S_{6.79}(0)$ distribution for the 3σ confidence region is plotted in Fig. 4.2 from the same point of view as Fig. **??** for a better comparison. Of course a two dimensional display of a three dimensional scatter plot is not ideal because some of the points are hidden behind others but the two figures are primarily plotted to give an idea of the procedure of defining adequate uncertainties for the extrapolated S-factors. The same procedure was used to calculate statistical

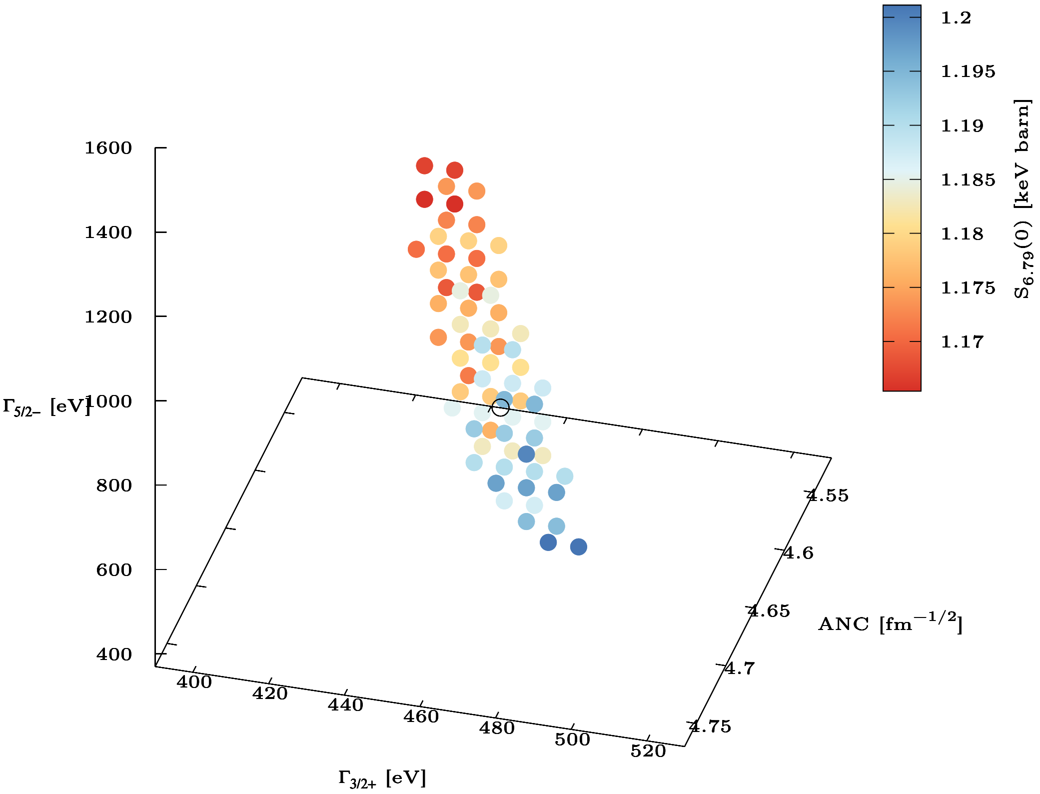

Figure 4.2.: The $S_{6.79}(0)$ dependence on the three varied parameters with channel radius $a = 5.5\,\text{fm}$. The axis are the same as in Fig. ?? for comparison. The dots in the three dimensional parameter space mark the 3σ region of the lowest χ^2 color coded for the $S_{6.79}(0)$ values. The black circle marks the extrapolation from the best fit with $S_{6.79}(0) = 1.186^{+0.015}_{-0.022}$ kev b.

uncertainties for the S-factor of direct capture to the ground state extrapolated to zero energy $S_{\text{g.s.}}(0) = 0.249^{+0.009}_{-0.008}$ keV b.

The described procedure of deriving statistical uncertainties from χ^2 fluctuations by varying free parameters of the R-Matrix fit in a defined parameter space can be extended to more than three free parameters easily, but a graphical representation would be difficult. A full R-matrix calculation with $N > 3$ free parameters is beyond the scope of this work but could in principle profit from this method of uncertainty determination if in addition randomization methods are used for the parameter variation. Otherwise the computing time is increasing exponentially with the power of N and therefore, would become difficult to handle.

Plots of the present R-matrix fit curves from both investigated transitions of the ^{14}N(p,γ)^{15}O reaction can be found in the next chapter. They are compared in Fig. 5.1 and Fig. 5.2 with the fits from R-matrix calculations by SFII (Ref. [AGR+11]) and

Notre Dame in Ref. [LGd+16].

5. Discussion

For capture to the 6.79 MeV excited state, the experimental S-factors of this work are compared in Tab. 5.1 to the S-factors of Ref. [SBB+87] and to the R-matrix fit of SFII from Ref. [AGR+11].

The literature S-factors were selected by energies that are as close as possible to the energies of this work. Some are different by more than 10 keV but this leads to no significant change of the S-factor as long as there is no resonance and the S-factor curve is rather flat around that energy.

The general trend for the SFII fit is an underestimation of the present and Bochum data that increases with higher energies. The fit in SFII included only one BGP of $J^\pi = \frac{5}{2}^-$ at $E = 6$ MeV that appears to be not sufficient to completely reproduce the tail of broad

Table 5.1.: ^{14}N(p,γ)^{15}O S-factors for capture to the 6.79 MeV excited state as a function of the effective energy $E_{\mathrm{c.m.}}$ compared to the R-matrix fit from the SFII review and the S-factors from Bochum of Ref. [SBB+87] with the renormalization recommended in SFII (see Ref. [AGR+11]) at similar energies.

present work		SFII Ref. [AGR+11]		Bochum Ref. [SBB+87]	
$E_{\mathrm{c.m.}}$ [keV]	$S_{6.79}(E_{\mathrm{c.m.}})$ [keV b]	$E_{\mathrm{c.m.}}$ [keV]	$S_{6.79}(E_{\mathrm{c.m.}})$ [keV b]	$E_{\mathrm{c.m.}}$ [keV]	$S_{6.79}(E_{\mathrm{c.m.}})$ [keV b]
357	1.27 ± 0.10	351	1.17	343.3	1.23 ± 0.47
479	1.12 ± 0.07	481	1.00	479.5	1.11 ± 0.11
574	1.17 ± 0.04	571	0.96	575.6	0.93 ± 0.08
613	1.05 ± 0.05	611	0.94	622.2	1.03 ± 0.05
676	1.14 ± 0.04	671	0.92	663.3	1.01 ± 0.05
780	1.00 ± 0.04	781	0.88	780.8	0.90 ± 0.09
780	1.07 ± 0.03	-	-	-	-
877	1.06 ± 0.03	871	0.86	866.7	0.94 ± 0.04
1028	1.17 ± 0.05	1031	0.82	1034.6	0.91 ± 0.09
1099	1.23 ± 0.04	1101	0.80	1108.3	0.97 ± 0.10
1202	1.21 ± 0.07	1201	0.78	1201.6	0.93 ± 0.12
1292	1.15 ± 0.07	1291	0.76	1295.8	0.96 ± 0.09

unidentified structures at higher energy.

The Bochum data are always lower then the present data, but they are within a 2σ uncertainty compatible with the present data. For energies above 1 MeV the discrepancy is stronger than for lower energies because the present data show an increase of 26 % on average over the literature data that remain flat. The statistical uncertainties of the present data are smaller then the uncertainties from the Bochum data. In addition these data from Ref. [SBB+87] had to be re-normalized by a factor of 0.91 because of an updated E = 259 keV resonance strength and new reference cross section values discussed in Ref. [AGR+11]. Without this correction the Bochum data would be even compatible within a 1σ uncertainty, raising again doubts about the treatment of those old data from 1987. In addition, without the original detection efficiency information, no summing correction can be applied either.

The resulting fit for capture to the 6.79 MeV excited state, the red solid curve in Fig. 5.1, shows a somewhat different slope in the E = 400 – 1300 keV range than SFII and Notre Dame, which are both below the present experimental data in this energy range. This

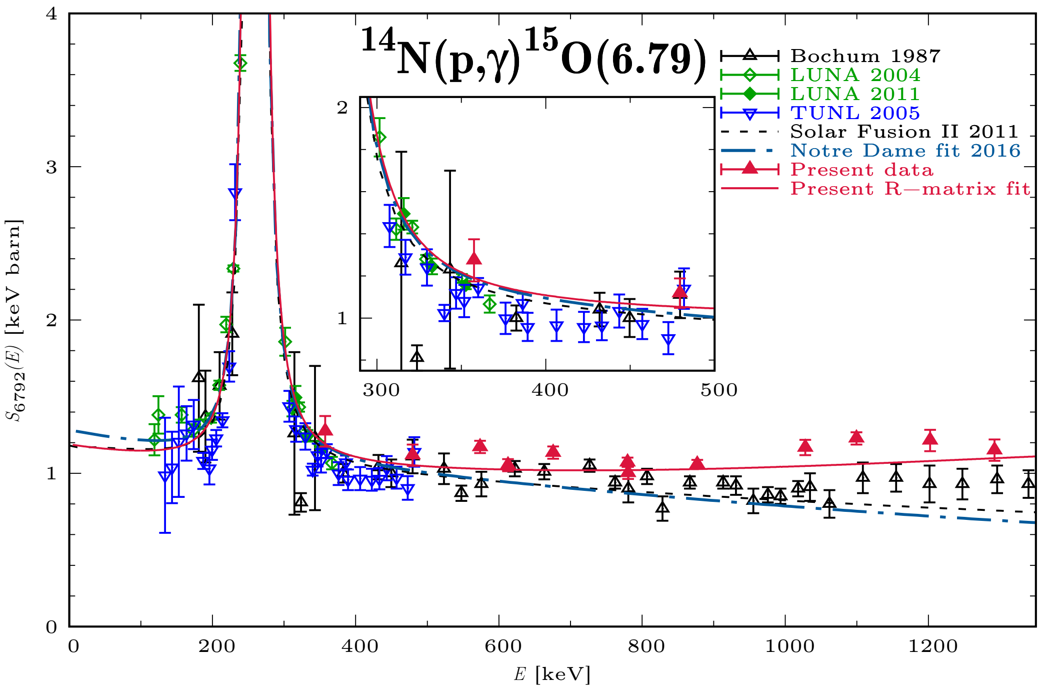

Figure 5.1.: Astrophysical S-factor for the 6.79 MeV transition in ^{14}N(p,γ)^{15}O from the literature [SBB+87, FIC+04, ICF+05, MFG+08, MFB+11, RCA+05] and from the present work. The data from Refs. [SBB+87, FIC+04, ICF+05, RCA+05] have been renormalized as in Ref. [AGR+11] for the 13.1 meV strength of the 259 keV resonance. The R-matrix fits by SFII from Ref. [AGR+11], Notre Dame from Ref. [LGd+16], and from the present work (Sec. 4.3) are also shown.

effect is most visible at E = 1000 − 1300 keV. A possible reason for the SFII fit is the missing BGP mentioned above. The lower Notre Dame fit is probably due to the data at high energies above 1500 keV that were included in the fit. A large sample of scattering data from Ref. [dBG$^+$15] and lower high energy S-factors for the 6.79 MeV transition from Ref. [LGd$^+$16] forces the fit curve to lower S-factors in the intermediate energy range, already.

Despite these non-negligible differences at high energies, the picture is more consistent at low, astrophysical energies. There, the present fit comes out only about 1 % higher than SFII. It should be kept in mind that Notre Dame reported a relatively high zero-energy S-factor for this transition, $S_{679}(0) = (1.29 \pm 0.04_{\text{stat}} \pm 0.09_{\text{syst}})$ keV b, higher than, but still consistent, with the SFII value of (1.18±0.05) keV b. The present result of $S_{679}(0) = (1.19 \pm 0.02_{\text{stat}} \pm 0.10_{\text{syst}})$ keV b lies between the SFII and Notre Dame results and is consistent with both. The systematic uncertainty of $S_{679}(0)$ derives from the 8 % systematic (scale) uncertainty of the present data points. The statistical uncertainty was found to be 0.02 keV b, negligible when compared to the systematic uncertainty. Therefore the total uncertainty of $S_{679}(0)$ is the same as the systematic 0.10 keV b.

For capture to the ground state, the comparison in Tab. 5.2 between the experimental S-factors of this work, the Bochum data and the SFII R-matrix fit yields a different result. While most of the S-factors of the two experimental data sets are consistent

Table 5.2.: ^{14}N(p,γ)^{15}O S-factors for capture to the ground state as a function of the effective energy $E_{\text{c.m.}}$ compared to the R-matrix fit from the SFII review and the S-factors from Bochum of Ref. [SBB$^+$87] with the renormalization recommended in SFII (see Ref. [AGR$^+$11]) at similar energies.

present work		SFII Ref. [AGR$^+$11]		Bochum Ref. [SBB$^+$87]	
$E_{\text{c.m.}}$ [keV]	$S_{\text{gs}}(E_{\text{c.m.}})$ [keV b]	$E_{\text{c.m.}}$ [keV]	$S_{\text{gs}}(E_{\text{c.m.}})$ [keV b]	$E_{\text{c.m.}}$ [keV]	$S_{\text{gs}}(E_{\text{c.m.}})$ [keV b]
479	0.19 ± 0.07	481	0.11	480	0.18 ± 0.05
574	0.26 ± 0.02	571	0.16	576	0.21 ± 0.03
613	0.22 ± 0.02	611	0.18	622	0.21 ± 0.02
676	0.24 ± 0.02	671	0.20	663	0.23 ± 0.02
780	0.26 ± 0.03	781	0.25	781	0.44 ± 0.05
780	0.31 ± 0.03	-	-	-	-
877	0.42 ± 0.02	881	0.29	867	0.40 ± 0.02
1028	0.30 ± 0.05	1031	0.35	1031	0.22 ± 0.02
1099	0.29 ± 0.03	1101	0.37	1108	0.35 ± 0.04
1202	0.23 ± 0.05	1201	0.42	1202	0.37 ± 0.04

within a 1σ uncertainty, there are some outliers in both sets.
A possible reasons for the present data point at $E = 574$ keV ($E_p = 640$ keV) could be a background problem, because it sits on top of a relatively flat Compton region caused by the ^{13}C(p,γ)^{14}N background peak (see Fig. A.3).
Another data point at $E = 1028$ keV just above the $E = 987$ keV resonance may have a problem with the angular correction as discussed in Sec. 3.3.2. In order to take this problem into account, the error bar is enlarged to cover also the value found when only analyzing the 55° detector.
The third exception is the highest-energy data point, which is corrected down by 50 % for a single-escape peak (see Sec. 3.3.1). This data point is significantly lower than the Bochum data and the R-matrix curves, but close to a Notre Dame data point at similar energy.
The impact of those outliers on R-matrix fits is diminished by the resonant contributions and the low energy data from Refs. [FIC$^+$04, ICF$^+$05, MFG$^+$08, MFB$^+$11, RCA$^+$05]. Since in Ref. [AGR$^+$11] it was decided to ignore the resonance at $E = 987$ keV for the SFII R-matrix fit, the deviations from the data are the strongest around this resonance. For most of the present data the SFII fit is different by more then 3σ uncertainty.

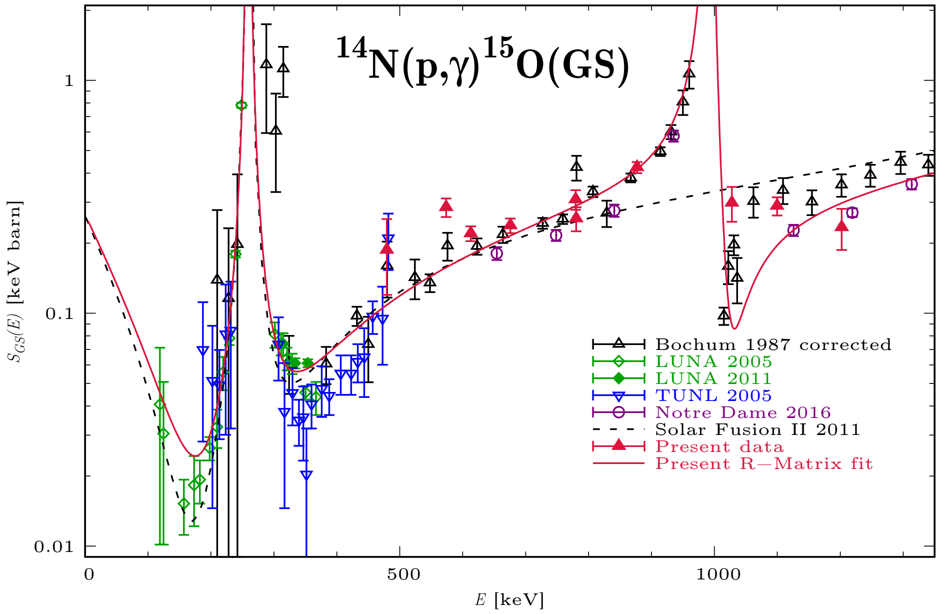

Figure 5.2.: Astrophysical S-factor for the ground state transition in ^{14}N(p,γ)^{15}O from the literature [SBB$^+$87, FIC$^+$04, ICF$^+$05, MFG$^+$08, MFB$^+$11, RCA$^+$05, LGd$^+$16] and from the present work. Normalization as in Fig. 5.1. The Bochum data of Ref. [SBB$^+$87] are shown corrected for the summing-in effect as discussed in Ref. [FIC$^+$04, AGR$^+$11]. The R-matrix fits by SFII from Ref. [AGR$^+$11] and from the present work (Sec. 4.3) are also shown.

The present R-matrix fit, that does not ignore the E = 987 keV resonance, results in a zero-energy extrapolation of $S_{\mathrm{GS}}(0)$ = (0.25 ± 0.01$_{\mathrm{stat}}$) keV b that is consistent with the SFII value of (0.27 ± 0.05) keV b but slightly lower. The higher upper limit of the error band recently suggested by Notre Dame with its value of (0.42 ± 0.04(stat)$^{+0.09}_{-0.19}$(syst)) keV b is not confirmed here. Interestingly, in the depression at $E \sim$ 300 keV, the present fit seems to favor the virtually summing-free LUNA data of Ref. [MFG^{+}08, MFB^{+}11] taken with a segmented detector over the TUNL and remaining LUNA data of Ref. [RCA^{+}05, FIC^{+}04, ICF^{+}05] with their summing issues. SFII shows a compromise between the different data sets at this area and is lower before the E = 259 keV resonance where only a few data from LUNA exists. The mentioned inclusion of the resonance at E = 0.987 MeV in the present fit improves the curve in the high energy region and has a small influence of 5 % on the low energy extrapolation. This may explain the lower zero-energy extrapolation in the present work when compared to SFII.

For the uncertainty of $S_{\mathrm{G}S}(0)$, the scaling uncertainty of the present data points makes only a negligible contribution, mainly due to the much stronger influence of the low-energy data points from LUNA and TUNL. Therefore the systematic uncertainty is taken from the SFII uncertainty with 0.05 keV b. As it is the case for the capture to the 6.79 MeV excited state, the statistical uncertainty of 0.01 keV b is dwarfed by the larger systematic uncertainty.

6. Towards new experiments on $^{14}N(p,\gamma)^{15}O$

To further improve the experimental basis for the ^{14}N(p,γ)^{15}O reaction different approaches can be pursued in order to overcome the problems that were faced in the progress of this work. In Sec. 6.1 the advantage of performing such experiments in underground laboratories and preliminary measurements of the cosmic muon background at a new underground lab are discussed. To reduce problems with beam induced background a different setup and method for ^{14}N(p,γ)^{15}O reaction measurements is explained in Sec. 6.2.

6.1. Muon flux measurement at the Dresden Felsenkeller

The cosmic-ray induced background in a laboratory overground like at the HZDR is orders of magnitude higher than deep underground with a massive overburden of rock that shields from cosmic-rays. This is explained in detail in Ref. [Gri01]. The signal to background ratio can be below one for measurements of reactions like ^{14}N(p,γ)^{15}O with very low cross sections. Especially overground this is often a limiting factor for experiments. Therefore, going underground is a good solution to reduce the background provided that the necessary infrastructure is available.

The world's only underground ion accelerator for nuclear astrophysics is LUNA at LNGS. The lab is inside a tunnel under the Gran Sasso mountain in Italy. The accelerator installed until now can provide ions with energies up to 400 keV only and is therefore not suited for studies at higher energies. The plans to upgrade it to a 3.5 MV accelerator are summarized in Ref. [Gug14]. Other deep underground accelerator projects are under development in the US and China (see Refs. [RCG^{+}16, LLH^{+}16] for details).

The approach at the HZDR is a little different. In collaboration with the Technical University Dresden, an old tunnel system near Dresden called "Felsenkeller" with 45 m rock overburden was selected to house a lab with a 5 MV Pelletron accelerator. At this depth the nucleonic component of cosmic-ray induced background consisting of protons and neutrons and the soft component, which is composed of electrons, positrons and γ's are sufficiently absorbed by the rock. However, high energy muons that are categorized as the hard component can not be absorbed by the rock efficiently in such a shallow underground site. A much larger thickness of rock like the 1400 m at LNGS would be necessary to reduce the muon induced background below the neutron background from the surrounding rock. Fig. 6.1 shows this dependency on the rock thickness and the arrows mark the depths of the different sites.

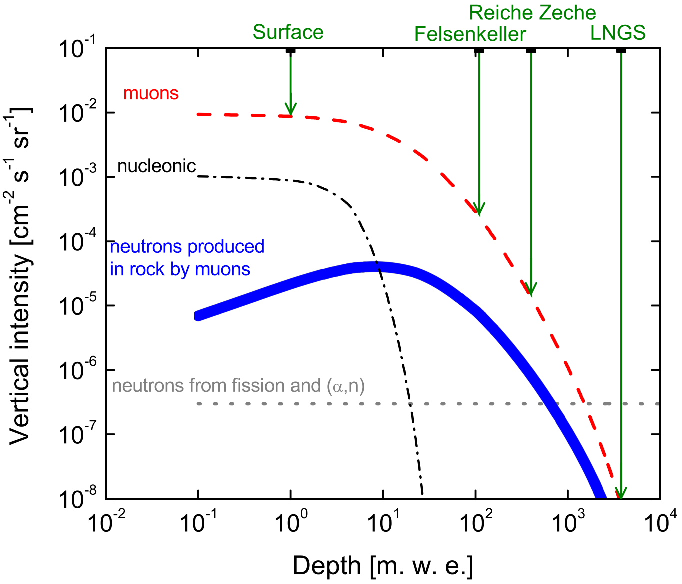

Figure 6.1.: The qualitative intensity dependence of muons (red dashed line), neutrons (black dash-dotted line) and muon induced neutrons (blue solid line) from the depth in meter water equivalent (m.w.e) is shown. Also plotted is the neutron flux (gray dotted line) from fission and (α,n) at the LNGS. The arrows mark the depths of different sites mentioned in the text. Fig. taken from Ref. [SBR^{+}15].

To overcome the drawback of a higher muon flux at the shallow underground lab, compared to deep underground, it was discovered in Ref. [SBC^{+}12] that an additional detector acting as a muon veto can reduce the muon induced signals in the main detector to rates comparable with measurements deep underground. For this purpose scintillation detectors similar to the BGO in the present setup (Sec. 2.3.2) were used. To get more detailed information on the muon flux in the Felsenkeller a comprehensive study was undertaken. A muon tomograph, described in detail in Ref. [OBH^{+}13], from the Hungarian REGARD[1] group was brought to the tunnels several times. A first measurement was taken by the developers of the muon tomograph themselves in 2013. This

---

[1] a collaboration between the Institute for Particle and Nuclear Physics, Wigner RCP and Eötvös University, Budapest

first impression of the muon flux with angular resolution was presented in Ref. [OSB+13]. In 2015 a muon tomograph from the REGARD group was bought by HZDR and the muon flux was measured at different positions with high angular resolution. The four measurement positions in the future Felsenkeller lab are marked on the relief map of Fig. 6.2. Positions MP 1 & 2 are the most interesting, because they represent the future positions of the detectors. MP 3 & 4 are located where the accelerator is installed now.

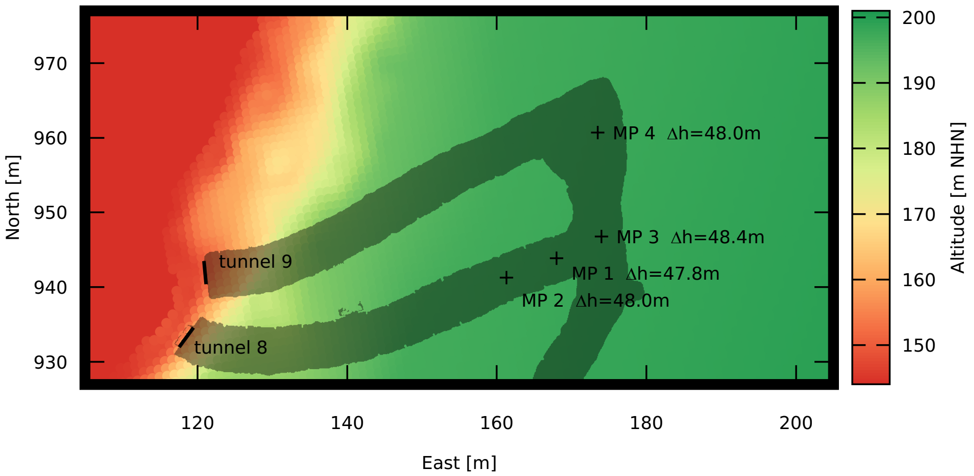

Figure 6.2.: This relief map of the altitude of the Dresden Felsenkeller terrain shows the sheer rock wall, the shape of the tunnels and the positions of the measurements. Δh is the thickness of the rock overburden at the according position.

Seven measurements per position were done to cover the whole hemisphere. To get good statistics each measurement was performed over 3 days. After the single measurements were analyzed to get the muon flux in polar coordinates, the flux maps were superimposed using the weighted average of the flux where the measurements overlapped. The results are flux maps of the whole hemisphere for the four positions as for example Fig. 6.3 for position 1.

The map of Fig. 6.3 shows the flux at the future position of the detectors for the irradiation experiments. The angle of incidence with the highest measured flux of $\Phi_{\mathrm{max}}(\phi,\theta) = (1.96 \pm 0.08)\,{}^{1}/_{\mathrm{m^2 s\,sr}}$ is at a polar angle of 55° and an azimuth angle of 300° (west north west). This is apparently more then the muon flux coming vertical through the 47.8 m of rock, which is $\Phi(\phi,0) = (1.70 \pm 0.04)\,{}^{1}/_{\mathrm{m^2 s\,sr}}$. The reason is the shorter distance to the sheer rock wall of 38 m. Lesser absorbing material in this direction reduces the muon flux not as much as vertical. This holds despite the fact

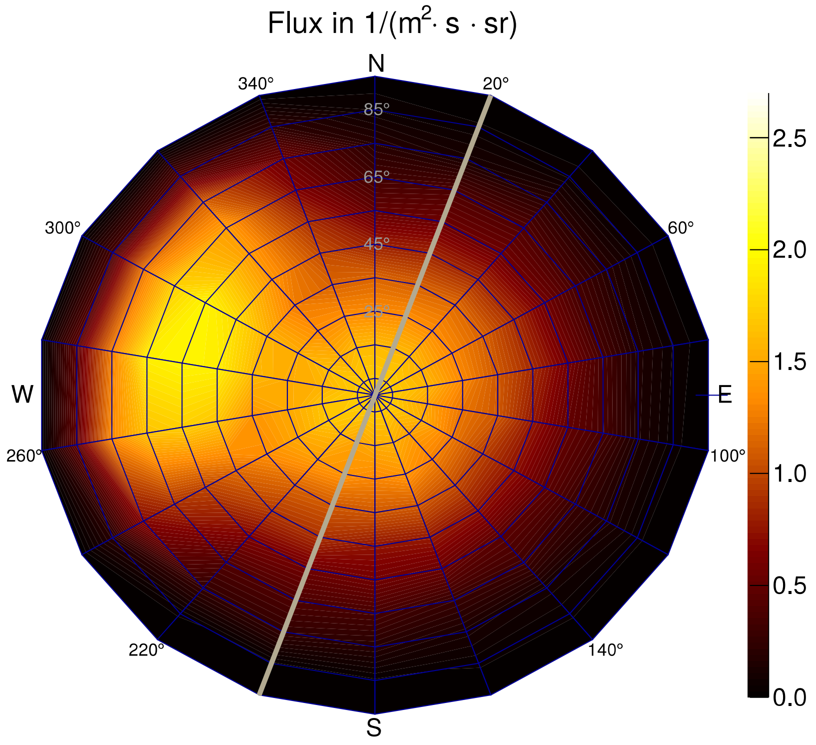

Figure 6.3.: The muon flux in tunnel 8 of the Dresden Felsenkeller at position MP 1. Fig. taken from Ref. [Lud17].

that the surface muon flux from this polar angle is one third of the vertical intensity I_0. Eq. (6.1) shows the ϕ dependence of the flux,

$$\Phi(\phi) = I_0 \cdot \cos^n \phi \tag{6.1}$$

from Ref. [Gri01], where n is a fitted parameter that varies around 2 depending on muon energy and surrounding material. The integrated muon flux at position MP 1 was $4.91\,{}^{1}/_{\mathrm{m^2 s}}$, which is about 3 % of the flux measured at the surface. The vertical intensity of $1.70\,{}^{10^{-4}}/_{\mathrm{cm^2 s}}$ is consistent with the qualitative curve from Fig. 6.1. Maps of the other three positions show a very similar picture. Only the absolute values vary slightly, depending on the distance to the rock wall.

The main conclusion from the muon flux mapping for the to-be detector setup is that most muons move through vertical and from the rock wall. Therefore, if a muon veto can not fully cover all angles, at least these two directions need to be covered.

The presented muon flux measurement results are just an outlook. In Ref. [Lud17], the master thesis of Felix Ludwig, the detailed analysis and all measurement can be found.

6.2. Activation measurement of ^{14}N(p,γ)^{15}O

The aim of this new experiment is to measure the total ^{14}N(p,γ)^{15}O reaction cross section with high precision. To achieve this a promising method is currently tested in the Institute for Nuclear Research (Atomki) in Debrecen, Hungary. For the so-called activation method the solid TiN target is periodically irradiated with the proton beam using the 2 MV tandem accelerator of Atomki. After each activation the decay radiation from the produced ^{15}O isotopes is counted.

In preliminary tests, performed in 2016, a period of 5 min beam and 20 min decay counting emerged as a good compromise. On one hand 20 min are roughly 10 times the half life of β^+ decay from ^{15}O ($T_{1/2}$ = 122.24(16) s) and the almost complete decay in this time makes fitting the decay curve easier in the analysis. On the other hand 5 min of beam with currents between 3 and 6 μA yield good count rates without activating to much β^+ background from proton capture reactions on the ^{12}C contamination and the ^{46}Ti atoms in the target.

The counts in the detector are 511 keV γ-rays that are produced by electron-positron annihilation from ^{15}O β^+-decay in the activated sample. The resulting count rate curve in Fig. 6.4 shows the saw tooth like shape coming from of the periodical irradiation and the nearly complete decay of the activated target each period. The yield of the reaction

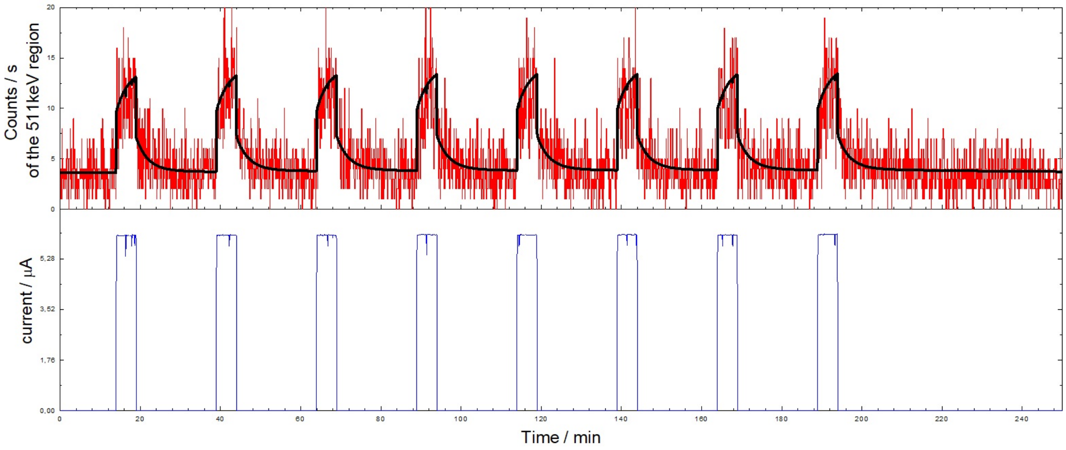

Figure 6.4.: The count rate of 511 keV γ-rays from electron-positron annihilation is plotted over a time of 250 min in the top histogram. It changes repeatedly between 0 and 20 counts/s. The black curve is a fit to the count rate with the irradiation periods and the β^+-decay time of ^{15}O as fixed parameters. In the bottom histogram the H$^+$-ion current in the different phases of the activation experiment is plotted with a plateau value of 6 μA. The irradiation pattern was 5 min of proton beam with E_p = 600 keV and 20 min decay counting without beam. Fig. kindly provided by Tamás Szücs from Atomki, Debrecen in Hungary.

is determined by fitting the shape of the count rate curve taking the proton current and the ^{15}O decay time into account.

One advantage of the setup compared to the setup described in Sec. 2.1 is a cooling trap in the beam line 50 cm before the target. This device, cooled down with liquid N_2 collects residues in the beam line and reduces buildup of contaminants on the target, like for example the carbon found on the targets in this work (Sec. 3.2.2). A similar cooling trap is included in the new target chamber design that will be used in the setup at the Dresden Felsenkeller lab, positioned 1 cm before the target.

The first targets for the new experiment at Atomki came from the same producer at HZDR as for this work and have 100 - 300 nm tick TiN layers. The stoichiometry was measured to be 1:1 with 1.2 % accuracy. The thickness was measured with the same NRRA method as described in Sec. 3.2.1 and confirmed with a Secondary Neutral Mass Spectrometer (SNMS). The SNMS method, described in Ref. [Oec93] provides detailed depth dependent elemental composition information similar to the ERDA performed in this work (Sec. 3.2.2). However, because the measurement, shown in Fig. 6.5 was not

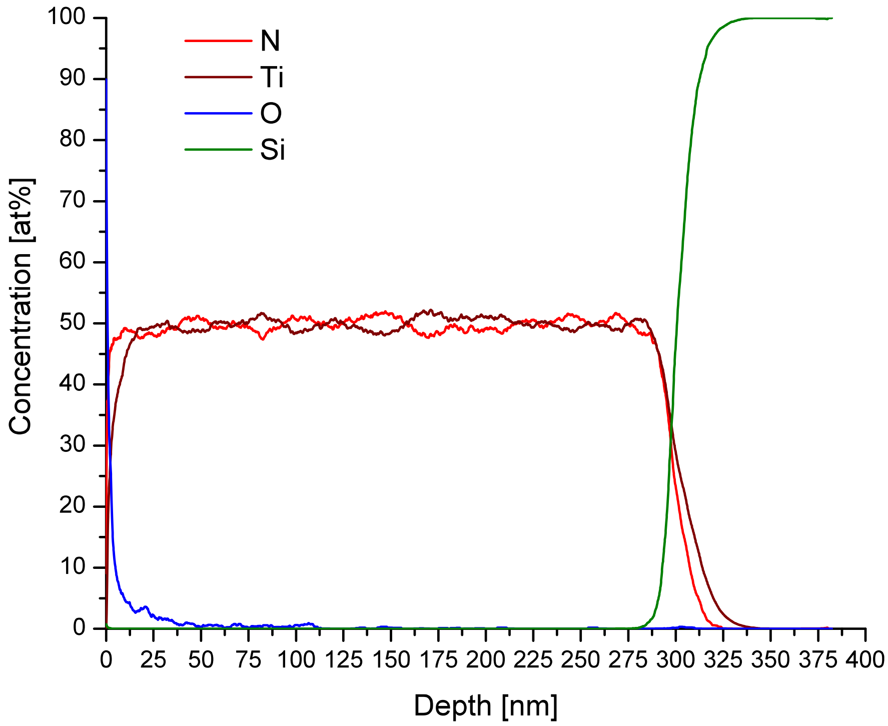

Figure 6.5.: A target profile measured with a SNMS. The TiN layer of 1:1 stoichiometry and 300 nm thickness is on a Si waver for this measurement. On the surface a thin O layer is visible. Fig. kindly provided by György Gyürky from Atomki, Debrecen in Hungary.

done with the irradiated targets on Ta backings no information about buildup or target degradation was gained. Instead the analyzed target was an unused sample with an Si waver as substrate that was placed simultaneously with the tantalum disc in the chamber for magnetron sputtering of the TiN layer.

These first results for the target characterization were presented at the 8th International Conference on Nuclear Physics in Astrophysics (NPA8) by our Hungarian collaborator György Gyürky from Atomki. Hopefully, once the whole experiment is finished and analyzed the total cross section will be known with better precision then the current 7 % from the accepted $S_{\text{total}}(0) = (1.66 \pm 0.12)$ keV b in Ref. [AGR^{+}11]. If that is the case, the present results of the partial cross sections for capture to the ground state and the 6.79 MeV excited state can be subtracted from the new total cross section and the difference could be a more precise value of the cross section of the sum of weaker states not measured in the present work.

7. Summary

A new measurement of the cross section of the ^{14}N(p,γ)^{15}O reaction was undertaken based on the analysis of two transitions. S-factor data were obtained by in-beam γ-ray spectroscopy at twelve c.m. energies between 357 – 1292 keV for capture to the 6.79 MeV excited state in ^{15}O and at ten c.m. energies between 479 – 1202 keV for capture to the ground state in ^{15}O. The absolute cross section was determined, normalized to a target composition obtained by the elastic recoil detection analysis technique.

The new data are not far from the previous wide energy range excitation function by the Bochum group in Ref. [SBB$^+$87], which had recently been questioned due to correction and renormalization issues. However, for the strongest transition, capture to the 6.79 MeV excited state, the present data show a somewhat higher slope than Bochum towards the higher-energy end. With smaller uncertainties, virtually no summing effects and robust target characterization the new data for both levels are superior to the Bochum data and can replace the Bochum direct capture data for energies between 357 – 1292 keV in R-matrix fits.

The impact of the new data on low astrophysical energies is gauged by a preliminary R-matrix fit.

For the 6.79 MeV transition, the resulting zero-energy extrapolated S-factor lies with $S_{679}(0) = (1.19 \pm 0.02_{\text{stat}} \pm 0.10_{\text{syst}})$ keV b between the recently reported extrapolated values from Notre Dame in Ref. [LGd$^+$16] and the previously accepted values from SFII (see Ref. [AGR$^+$11]). It seems that the low energy extrapolation is robust even when taking the somewhat higher, present high-energy 6.79 MeV data into account.

For the capture to the ground state, the present extrapolated value to zero-energy of $S_{\text{GS}}(0) = (0.25 \pm 0.01_{\text{stat}} \pm 0.05_{\text{syst}})$ keV b is lower than but still consistent with the Notre Dame and SFII values.

Summarizing, the 6.79 MeV transition may be excluded as a source of significant uncertainty for the total extrapolated cross section. This means the efforts to improve the uncertainty of the total cross section, needed for the SSM neutrino predictions with a precision better than 5 %, have to concentrate on the weaker transitions. There the uncertainties are much larger, including the ground state capture with 20 % relative uncertainty. For these cases, a new comprehensive data set connecting the precise low-

energy LUNA data (see Refs. [FIC+04, ICF+05, MFG+08, MFB+11]) with the wide energy range Bochum data points from Ref. [SBB+87] is still missing.
Due to the long running times and low counting rates, such data can best be provided at one of the upcoming higher-energy underground accelerators introduced in Refs. [Gug14, RCG+16, LLH+16, BCC+17b]. Especially for the Felsenkeller laboratory, where it was shown previously in Ref. [SBR+15] that the cosmic-ray induced background is about as low as in deep underground labs if a muon veto is used, now the proper alignment and positioning of a veto detector is known. The lab will be commissioned this year and could be used to measure the weaker transitions including the capture to the ground state on a large energy range with lower cosmic-ray induced background. The new target chamber for the lab could help to reduce beam induced background.
An update of the total cross section of ^{14}N(p,γ)^{15}O was not achieved in this work, because weaker transitions to the 6.172, 5.241 and 5.181 MeV level could not be measured with the setup. If recent experiments succeed to measure the total cross section independently by the activation method with low uncertainty, the impact of the weak transitions could be recalculated with better precision.

A. Appendix

A.1. Abbreviations and physical constants used in this work

Abbreviations

BGO	Bismuth germanate (detector) $Bi_4Ge_3O_{12}$
BGP	background pole
c.m.	center-of-mass frame of reference
CIVEN	Coordinamento Interuniversitario Veneto per le Nanotecnologie
DAQ	data acquisition
ERDA	Elastic Recoil Detection Analysis
FWHM	full width half maximum
Geant4	Geometry and Tracking v.4
GS	ground state
HI-ERD	heavy-ion elastic recoil detection
HPGe	high-purity Ge
HZDR	Helmholtz-Zentrum Dresden-Rossendorf
INFN	Istituto Nazionale di Fisica Nucleare
LNL	Laboratori Nazionali di Legnaro
LUNA	Laboratory for Underground Nuclear Astrophysics
m.w.e.	meter water equivalent
NDF	Nuno's DataFurnace

NRRA	Nuclear Resonant Reaction Analysis
PTB	Physikalisch-Technische Bundesanstalt
SE	secondary electrons
SFII	Solar fusion cross sections II
SNMS	Secondary Neutral Mass Spectrometer
SRIM	The Stopping and Range of Ions in Matter
SSM	Solar Standard Model
stat	statistical uncertainty
sys	systematic uncertainty
TiN	titanium nitride
TUNL	Triangle Universities Nuclear Laboratory

Physics Constants

c = 299 792 458 m/s speed of light in vacuum [MTN12, Tab. XL, p. 1586]

e = 1. 602 176 565 (35) $\cdot 10^{-19}$ As the elemental charge [MTN12, Tab. XL, p. 1586]

h = 6. 626 069 57 (29) $\cdot 10^{34}$ Js Planck constant [MTN12, Tab. XL, p. 1586]

k = 1. 380 648 8 (13) $\cdot 10^{-23}$ J/K Boltzmann constant [MTN12, Tab. XL, p. 1586]

m_{Cl} = 35.45 (1) u Cl mass at rest [MBB+16, Tab. 1, p. 272]

m_{Ti} = 47.867 (1) u Ti mass at rest [MBB+16, Tab. 1, p. 272]

m_e = 510 998. 928 (11) eV electron mass at rest [AWW+12, Tab. A, p. 1290]

m_p = 1. 007 276 466 92 (9) u proton mass at rest [AWW+12, Tab. A, p. 1290]

$m_{^{15}\mathrm{N}}$ = 15. 000 108 898 884 (643) u ^{15}N mass at rest [WAW+12, Tab. A, p. 1620]

N_A = 6. 022 141 29 (27) $\cdot 10^{23}$ mol^{-1} Avogadro constant [MTN12, Tab. XL, p. 1586]

A.2. Efficiency curves and γ-spectra of the experiment

For each of the three phases of the experiment a new efficiency calibration was performed. The figures on the next three pages show the calibration results and the fitted efficiency curves.
Subsequent, Fig. A.3 and Fig. A.4 show all γ-ray spectra of the detector at 55°, that could be analyzed in Sec. 3.3. In all panels the marked region is the peak of interest and the red lines to the left and right of the peak show the fitted background level, that was subtracted from the region of interest. The peak shape and position of the primary γ-rays for capture to the 6792 keV level and direct capture to the ground state depend on the target thickness and proton energy. The fitted peak width and the right flank of the peak are marked with arrows. The fit results of these parameters, printed next to the arrows, were used in Fig. 3.8 for comparison to the independent target analysis techniques in Sec. 3.2.1 and Sec. 3.2.2.

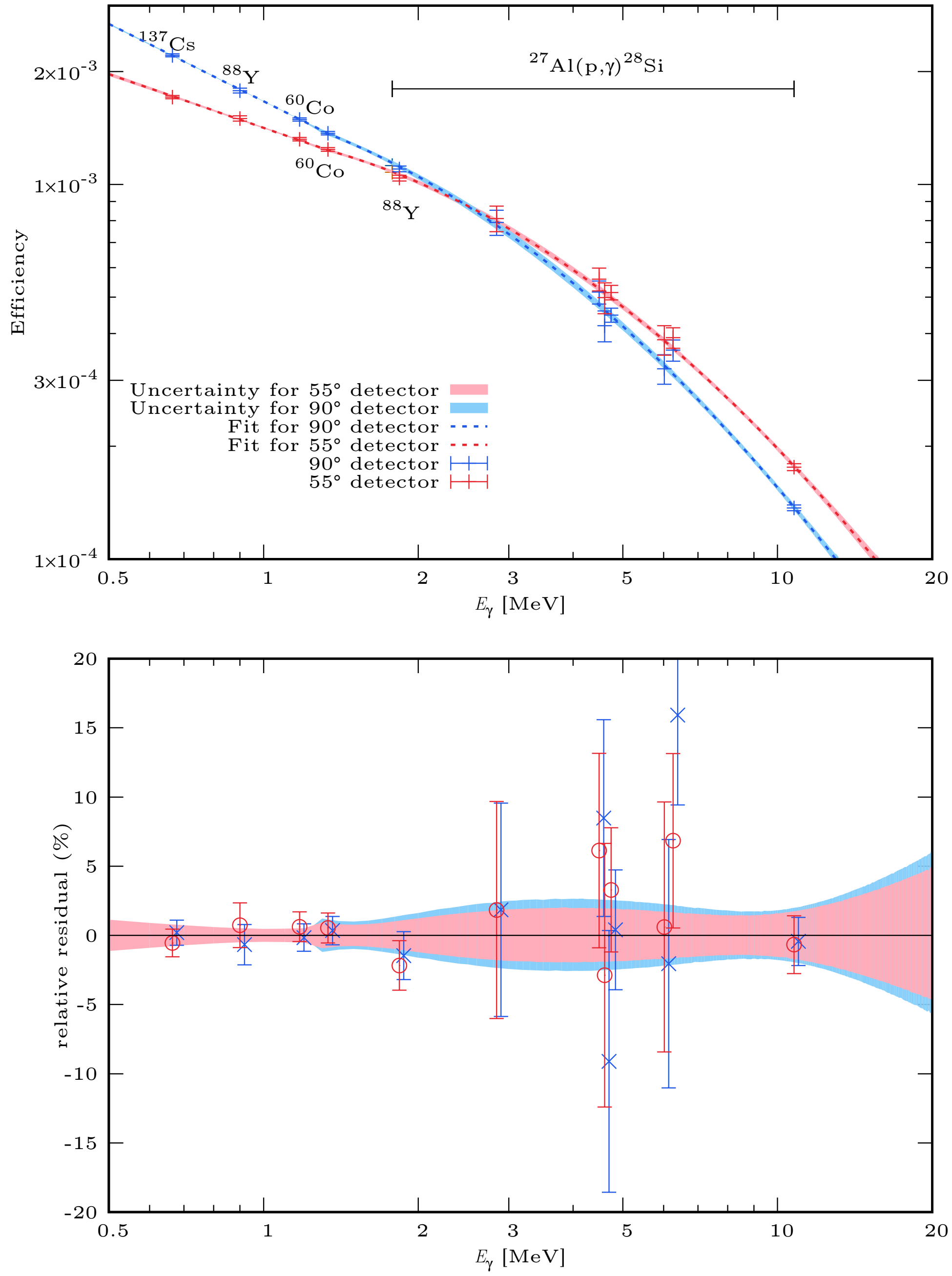

Figure A.1.: The calculated γ-ray detection efficiency $\varepsilon(E_\gamma)$ for detector 1 at 55° in red and detector 2 at 90° in blue, tagged with the source (decay or ^{27}Al(p,γ)^{28}Si reaction) are in the top panel together with the fitted efficiency curves and their uncertainties. The bottom panel shows the relative differences to the respective fit. Results of phase 1.

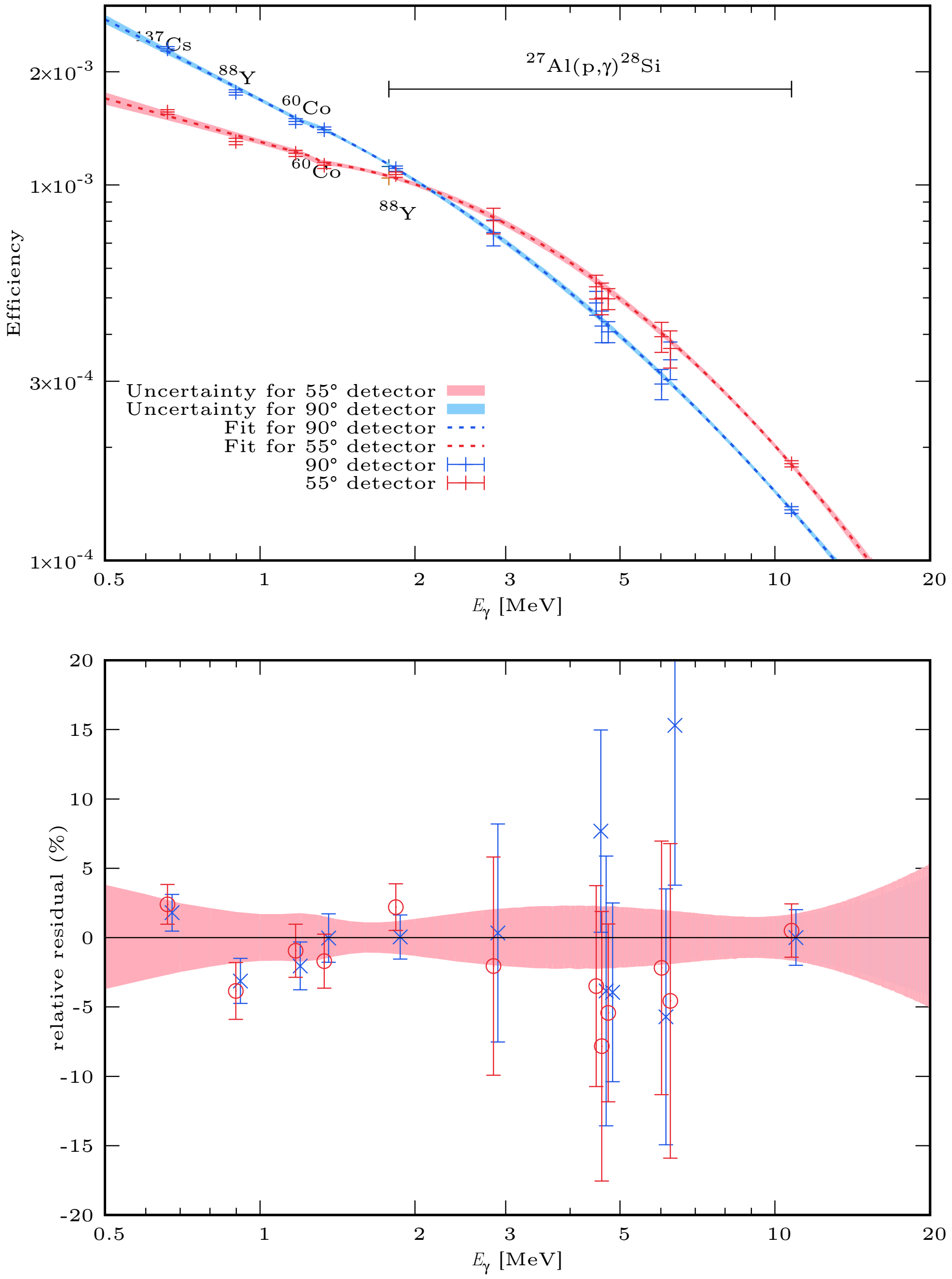

Figure A.2.: See Fig. A.1 for description. Results of phase 2.

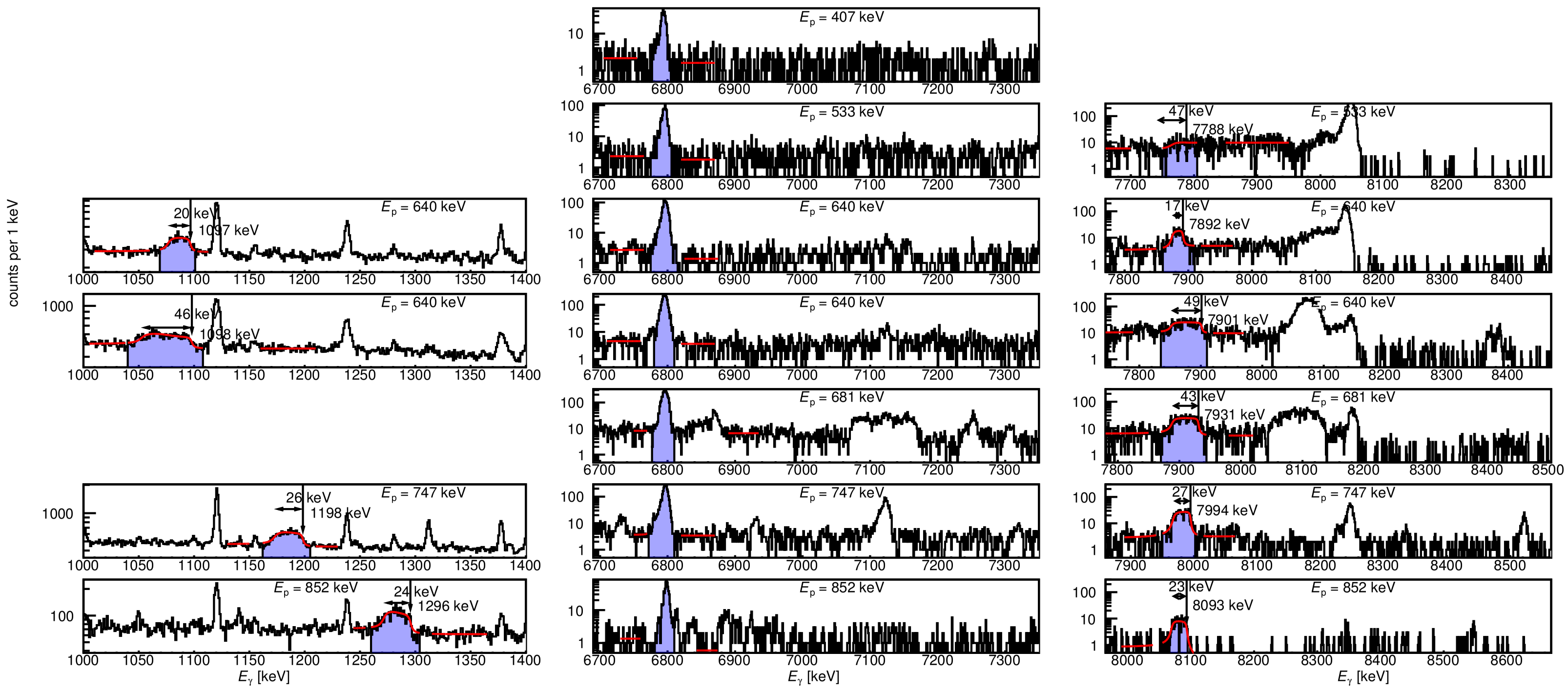

Figure A.3.: In-beam γ-ray spectra from the 55° detector for the E_p = 407 keV – 852 keV with marked regions of interest.The left panels show the primary γ-ray from capture to the 6792 keV level. The middle panels show the secondary peak of the same level and the right panels show the ground state capture peak. Where a panel is not shown, no clean peak could be identified. The special case for the ground state capture at $E_\mathrm{p} = 533$ keV is discussed in Sec. 3.3.1.

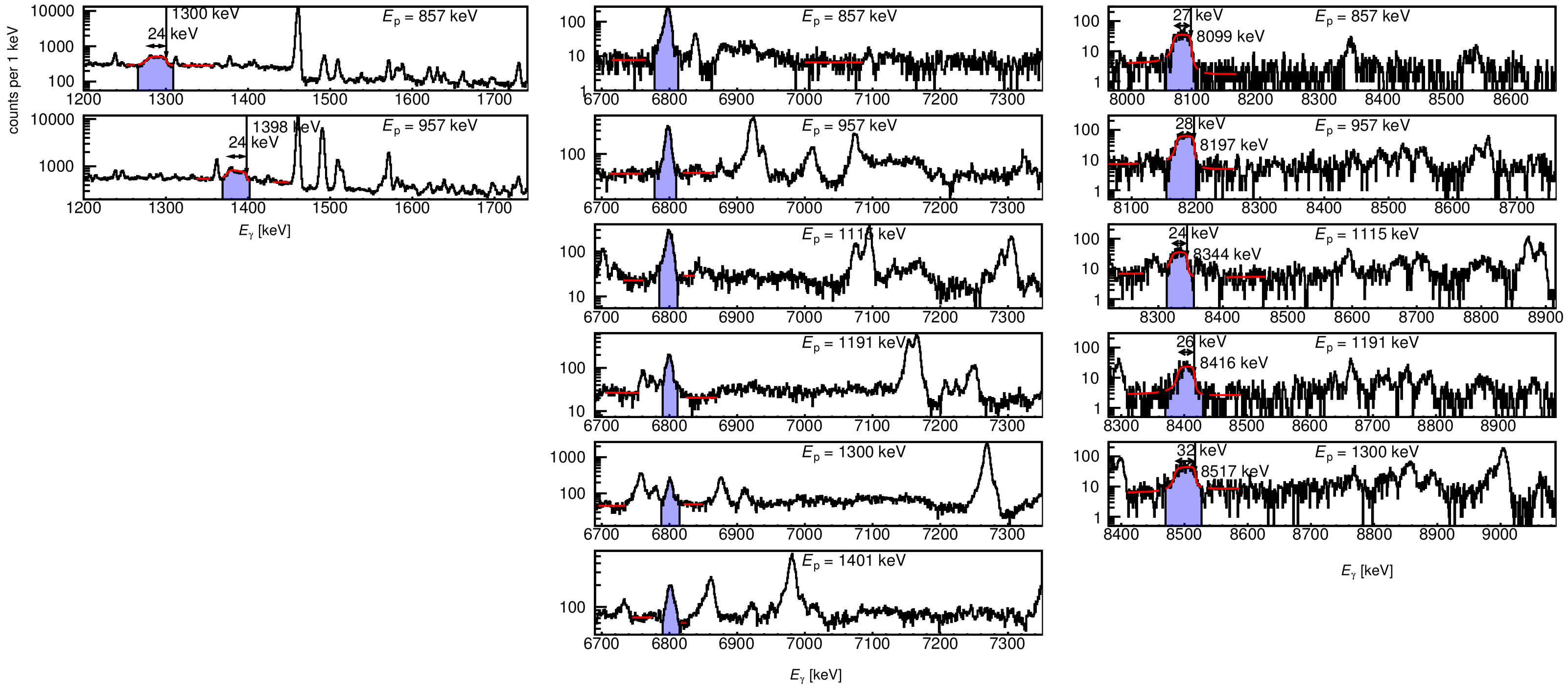

Figure A.4.: In-beam γ-ray spectra from the 55° detector for the $E_\mathrm{p} = 857$ keV – 1401 keV with marked regions of interest.The left panels show the primary γ-ray from capture to the 6792 keV level. The middle panels show the secondary peak of the same level and the right panels show the ground state capture peak. Where a panel is not shown, no clean peak could be identified. The problems with single-escapes in the secondary peaks at $E_\mathrm{p} = 1115$ keV and 1300 keV are discussed in Sec. 3.3.1.

Bibliography

[A+03] S. Agostinelli et al. GEANT 4 - a simulation toolkit. *Nucl. Inst. Meth. A*, 506(3):250 – 303, 2003.

[A+16] S Andringa et al. Current Status and Future Prospects of the SNO+ Experiment. *Adv. High Energy Phys.*, 2016:6194250, 2016.

[AAB+98] E.G. Adelberger, S. M. Austin, J. N. Bahcall, A. B. Balantekin, G. Bogaert, L. S. Brown, L. Buchmann, F. E. Cecil, A. E. Champagne, L. de Braeckeleer, C. A. Duba, S. R. Elliott, S. J. Freedman, M. Gai, G. Goldring, C. R. Gould, A. Gruzinov, W. C. Haxton, K. M. Heeger, E. Henley, C. W. Johnson, M. Kamionkowski, R. W. Kavanagh, S. E. Koonin, K. Kubodera, K. Langanke, T. Motobayashi, V. Pandharipande, P. Parker, R. G. Robertson, C. Rolfs, R. F. Sawyer, N. Shaviv, T. D. Shoppa, K. A. Snover, E. Swanson, R. E. Tribble, S. Turck-Chièze, and J. F. Wilkerson. Solar fusion cross sections. *Rev. Mod. Phys.*, 70:1265–1291, 1998.

[AAR+99] Carmen Angulo, M. Arnould, M. Rayet, P. Descouvemont, D. Baye, C. Leclercq-Willain, A. Coc, S. Barhoumi, P. Aguer, C. Rolfs, R. Kunz, J. W. Hammer, A. Mayer, T. Paradellis, S. Kossionides, C. Chronidou, K. Spyrou, S. degl'Innocenti, G. Fiorentini, B. Ricci, S. Zavatarelli, C. Providencia, H. Wolters, J. Soares, C. Grama, J. Rahighi, A. Shotter, and M. Lamehi Rachti. A compilation of charged-particle induced thermonuclear reaction rates. *Nucl. Phys. A*, 656:3–187, 1999.

[ACA+11] S. Albrecht, C. Cymorek, K. Andersson, K. Reichert, and R. Wolf. *Tantalum and Tantalum Compounds*. Ullmann's Encyclopedia of Industrial Chemistry, 2011.

[AD01] Carmen Angulo and Pierre Descouvemont. The ^{14}N(p,γ)^{15}O low-energy S-factor. *Nucl. Phys. A*, 690:755–768, 2001.

[AGR+11] E.G. Adelberger, A. García, R. G. H. Robertson, K. A. Snover, A. B. Balantekin, K. Heeger, M. J. Ramsey-Musolf, D. Bemmerer, A. Junghans, C. A. Bertulani, J.-W. Chen, H. Costantini, P. Prati, M. Couder, E. Uberseder, M. Wiescher, R. Cyburt, B. Davids, S. J. Freedman, M. Gai, D. Gazit, L. Gialanella, G. Imbriani, U. Greife, M. Hass, W. C. Haxton, T. Itahashi, K. Kubodera, K. Langanke, D. Leitner, M. Leitner, P. Vetter, L. Winslow, L. E. Marcucci, T. Motobayashi, A. Mukhamedzhanov, R. E. Tribble, K. M. Nollett, F. M. Nunes, T.-S. Park, P. D. Parker, R. Schiavilla, E. C. Simpson, C. Spitaleri, F. Strieder, H.-P. Trautvetter, K. Suemmerer, and S. Typel. Solar fusion cross sections. II. The pp chain and CNO cycles. *Rev. Mod. Phys.*, 83:195–246, 2011.

[AGSS09] M. Asplund, N. Grevesse, A. J. Sauval, and P. Scott. The Chemical Composition of the Sun. *Annu. Rev. Astron. Astroph.*, 47:481–522, September 2009.

[Ajz91] F. Ajzenberg-Selove. Energy levels of light nuclei a = 13-15. *Nucl. Phys. A*, 523:1–196, 1991.

[AKHF77] A. Anttila, J. Keinonen, M. Hautala, and I. Forsblom. Use of the ^{27}Al(p,γ)^{28}Si, E_{p} = 992 keV resonance as a gamma-ray intensity standard. *Nucl. Inst. Meth.*, 147(3):501 – 505, 1977.

[AU+10a] Richard Azuma, , E. Uberseder, E. C. Simpson, C. R. Brune, H. Costantini, R. J. de Boer, J. Görres, M. Heil, P. J. Leblanc, C. Ugalde, and M. Wiescher. http://azure.nd.edu/, 2010.

[AU+10b] Richard Azuma, , E. Uberseder, E. C. Simpson, C. R. Brune, H. Costantini, R. J. de Boer, J. Görres, M. Heil, P. J. Leblanc, C. Ugalde, and M. Wiescher. AZURE: An R-matrix code for nuclear astrophysics. *Phys. Rev. C*, 81:045805, 2010.

[AWW+12] G. Audi, M. Wang, A.H. Wapstra, F.G. Kondev, M. MacCormick, X. Xu, and B. Pfeiffer. The Ame2012 atomic mass evaluation. *Chinese Physics C*, 36(12):1287, 2012.

[AZ77] H. H. Andersen and J. F. Ziegler. *Hydrogen Stopping Powers and Ranges in All Elements*, volume 3 of *The Stopping and Ranges of Ions in Matter*. PERGAMON PRESS, 1977.

[Bah89] J. N. Bahcall. *Neutrino Astrophysics*. Cambridge and New York, Cambridge University Press, 1989.

[Bas13] M. Shamsuzzoha Basunia. Nuclear Data Sheets for A = 28. *Nuclear Data Sheets*, 114(10):1189 – 1291, 2013.

[BBB$^+$14] BOREXINO Collaboration, G. Bellini, J. Benziger, D. Bick, G. Bonfini, D. Bravo, B. Caccianiga, L. Cadonati, F. Calaprice, A. Caminata, P. Cavalcante, A. Chavarria, A. Chepurnov, D. D'Angelo, S. Davini, A. Derbin, A. Empl, A. Etenko, K. Fomenko, D. Franco, F. Gabriele, C. Galbiati, S. Gazzana, C. Ghiano, M. Giammarchi, M. Göger-Neff, A. Goretti, M. Gromov, C. Hagner, E. Hungerford, A. Ianni, A. Ianni, V. Kobychev, D. Korablev, G. Korga, D. Kryn, M. Laubenstein, B. Lehnert, T. Lewke, E. Litvinovich, F. Lombardi, P. Lombardi, L. Ludhova, G. Lukyanchenko, I. Machulin, S. Manecki, W. Maneschg, S. Marcocci, Q. Meindl, E. Meroni, M. Meyer, L. Miramonti, M. Misiaszek, M. Montuschi, P. Mosteiro, V. Muratova, L. Oberauer, M. Obolensky, F. Ortica, K. Otis, M. Pallavicini, L. Papp, L. Perasso, A. Pocar, G. Ranucci, A. Razeto, A. Re, A. Romani, N. Rossi, R. Saldanha, C. Salvo, S. Schönert, H. Simgen, M. Skorokhvatov, O. Smirnov, A. Sotnikov, S. Sukhotin, Y. Suvorov, R. Tartaglia, G. Testera, D. Vignaud, R. B. Vogelaar, F. von Feilitzsch, H. Wang, J. Winter, M. Wojcik, A. Wright, M. Wurm, O. Zaimidoroga, S. Zavatarelli, K. Zuber, and G. Zuzel. Neutrinos from the primary proton-proton fusion process in the Sun. *Nature*, 512:383–386, August 2014.

[BCC$^+$17a] J. F. Beacom, S. Chen, J. Cheng, S. N. Doustimotlagh, Y. Gao, S.-F. Ge, G. Gong, H. Gong, L. Guo, R. Han, X. Huang, J. Li, J. Li, M. Li, X. Li, G.-L. Lin, Z. Liu, W. McDonough, J. Tang, L. Wan, Y. Wang, Z. Wang, Z. Wang, H. Wei, Y. Xi, Y. Xu, Z. Yang, C. Yao, M. Yeh, Q. Yue, L. Zhang, Y. Zhang, Z. Zhao, Y. Zheng, X. Zhou, X. Zhu, and K. Zuber. Letter of Intent: Jinping Neutrino Experiment. *Chinese Physics C*, 41:023002, 2017.

[BCC$^+$17b] D. Bemmerer, F. Cavanna, T. E. Cowan, M. Grieger, T. Hensel, A. R. Junghans, F. Ludwig, S. E. Müller, B. Rimarzig, S. Reinicke, S. Schulz, R. Schwengner, K. Stöckel, T. Szücs, M. P. Takács, A. Wagner, L. Wagner, and K. Zuber. *Progress of the Felsenkeller shallow-underground accelerator for nuclear astrophysics*, volume 14, page 021106. Proceedings of the 14th International Symposium on Nuclei in the Cosmos (NIC2016), 2017.

[BCE$^+$09] S. Basu, W. J. Chaplin, Y. Elsworth, R. New, and A. M. Serenelli. Fresh Insights on the Structure of the Solar Core. *Astrophys. J.*, 699:1403–1417, July 2009.

[BCL+06] Daniel Bemmerer, F. Confortola, A. Lemut, R. Bonetti, C. Broggini, P. Corvisiero, H. Costantini, J. Cruz, A. Formicola, Z. Fülöp, G. Gervino, A. Guglielmetti, C. Gustavino, G. Gyürky, G. Imbriani, A. Jesus, M. Junker, B. Limata, R. Menegazzo, P. Prati, V. Roca, C. Rolfs, D. Rogalla, M. Romano, C. Rossi-Alvarez, F. Schümann, E. Somorjai, O. Straniero, F. Strieder, F. Terrasi, and H. P. Trautvetter. Low energy measurement of the ^{14}N(p,γ)^{15}O total cross section at the LUNA underground facility. *Nucl. Phys. A*, 779:297–317, 2006.

[BCP+01] P.F. Bertone, A. E. Champagne, D. C. Powell, C. Iliadis, S. E. Hale, and V. Y. Hansper. Lifetime of the 6793-keV state in ^{15}O. *Phys. Rev. Lett.*, 87:152501, 2001.

[BFIS62] John N. Bahcall, William A. Fowler, I. Iben, and R. L. Sears. Solar neutrino flux. *The Astrophysical Journal*, 137:344–346, 12 1962.

[BJN52] C. A. Barnes, D. B. James, and G. C. Neilson. Angular Distribution of the Gamma Rays from the Reaction $^{15}\mathrm{N}(\mathrm{p},\alpha\gamma)^{12}\mathrm{C}$. *Can. J. Phys.*, 30:717–718, Nov 1952.

[BJW97] N. P. Barradas, C. Jeynes, and R. P. Webb. Simulated annealing analysis of rutherford backscattering data. *Appl. Phys. Lett.*, 71(2):291–293, 1997.

[BLUB09] M. Borowski, K. P. Lieb, M. Uhrmacher, and W. Bolse. Precision Measurements of the 278 keV ^{14}N(p,γ) and the 151 keV ^{18}O(p,α) Resonance Parameters. In *AIP Conf. Proc. 1090: Capture Gamma-Ray Spectroscopy and Related Topics*, page 450, January 2009.

[CBd+02] T. B. Coplen, J. K. Böhlke, P. de Bièvre, T. Ding, N. E. Holden, J. A. Hopple, H. R. Krouse, A. Lamberty, H. S. Peiser, K. Révész, S.E. Rieder, K. J. R. Rosman, E. Roth, P.D.P. Taylor, R. D. Vocke, Jr., and Y. K. Xiao. Isotope-abundance variations of selected elements (IUPAC Technical Report). *Pure Appl. Chem.*, 74:1987–2017, 2002.

[CCL+02] C. Casella, H. Costantini, A. Lemut, B. Limata, D. Bemmerer, R. Bonetti, C. Broggini, L. Campajola, P. Cocconi, P. Corvisiero, J. Cruz, A. D'Onofrio, A. Formicola, Z. Fülöp, G. Gervino, L. Gialanella, A. Guglielmetti, C. Gustavino, G. Gyurky, A. Loiano, G. Imbriani, A. P. Jesus, M. Junker, P. Musico, A. Ordine, F. Parodi, M. Parolin, J. V. Pinto, P. Prati, J. P. Ribeiro, V. Roca, D. Rogalla, C. Rolfs, M. Romano, C. Rossi-Alvarez, A. Rottura,

F. Schuemann, E. Somorjai, F. Strieder, F. Terrasi, H. P. Trautvetter, A. Vomiero, and S. Zavatarelli. A new setup for the underground study of capture reactions. *Nucl. Inst. Meth. A*, 489:160–169, August 2002.

[CLS+11] E. Caffau, H.-G. Ludwig, M. Steffen, B. Freytag, and P. Bonifacio. Solar Chemical Abundances Determined with a CO5BOLD 3D Model Atmosphere. *Solar Physics*, 268:255–269, February 2011.

[D+04] E.G. Degl'Innocenti et al. The ^{14}N(p,γ)^{15}O reaction, solar neutrinos and the age of globular clusters. *Phys. Lett. B*, 590:13–20, 2004.

[DB10] Pierre Descouvemont and Daniel Baye. The R-matrix theory. *Rep. Prog. Phys.*, 73:036301, 2010.

[dBG+15] R. J. deBoer, D. W. Bardayan, J. Görres, P. J. LeBlanc, K. V. Manukyan, M. T. Moran, K. Smith, W. Tan, E. Uberseder, M. Wiescher, P. F. Bertone, A. E. Champagne, and M. S. Islam. Low energy scattering cross section ratios of $^{14}\mathrm{N}(p,p)^{14}\mathrm{N}$. *Phys. Rev. C*, 91:045804, Apr 2015.

[DCF+15] Rosanna Depalo, Francesca Cavanna, Federico Ferraro, Alessandra Slemer, Tariq Al-Abdullah, Shavkat Akhmadaliev, Michael Anders, Daniel Bemmerer, Zoltán Elekes, Giovanni Mattei, Stefan Reinicke, Konrad Schmidt, Carlo Scian, and Louis Wagner. Strengths of the resonances at 436, 479, 639, 661, and 1279 keV in the ^{22}Ne(p,γ)^{23}Na reaction. *Phys. Rev. C*, 92:045807, Oct 2015.

[DKC+16] S. Daigle, K. J. Kelly, A. E. Champagne, M. Q. Buckner, C. Iliadis, and C. Howard. Measurement of the E$_{r,c.m.}$ = 259 keV resonance in the ^{14}N(p ,γ)^{15}O reaction. *Phys. Rev. C*, 94(2):025803, August 2016.

[ELR+15] S. Elhatisari, D. Lee, G. Rupak, E. Epelbaum, H. Krebs, T. A. Lähde, T. Luu, and U.-G. Meißner. Ab initio α–α scattering. *Nature*, 528:111–114, December 2015.

[ES08] J. Eberth and J. Simpson. From Ge(Li) detectors to gamma-ray tracking arrays-50 years of gamma spectroscopy with germanium detectors. *Progress in Particle and Nuclear Physics*, 60(2):283 – 337, 2008.

[FBHT96] M. Friedrich, W. Bürger, D. Henke, and S. Turuc. The Rossendorf 3 MV tandetron: a new generation of high-energy implanters. *Nucl. Inst. Meth. A*, 382:357–360, February 1996.

[FIC$^+$04] A. Formicola, G. Imbriani, H. Costantini, C. Angulo, D. Bemmerer, R. Bonetti, C. Broggini, P. Corvisiero, J. Cruz, P. Descouvemont, Z. Fülöp, G. Gervino, A. Guglielmetti, C. Gustavino, G. Gyürky, A. P. Jesus, M. Junker, A. Lemut, R. Menegazzo, P. Prati, V. Roca, C. Rolfs, M. Romano, C. Rossi Alvarez, F. Schümann, E. Somorjai, O. Straniero, F. Strieder, F. Terrasi, H. P. Trautvetter, A. Vomiero, and S. Zavatarelli. Astrophysical S-factor of ^{14}N(p,γ)^{15}O. *Phys. Lett. B*, 591:61–68, 2004.

[FT03] M. Friedrich and H. Tyrroff. A modified ion sputter source with increased lifetime. *Nucl. Inst. Meth. B*, 201(4):645 – 648, 2003.

[Gil08] G. Gilmore. *Practical γ-ray spectrometry, 2nd edition*. John Wiley and Sons, New York, 2008.

[Gri01] P.K.F. Grieder. *Cosmic Rays at Earth: Researcher's Reference Manual and Data Book*. Elsevier Science Limited, 2001.

[Gug14] Alessandra Guglielmetti. Nuclear astrophysics and underground accelerators. *Physics of the Dark Universe*, 4:10 – 13, 2014.

[HA04] F. Herwig and S. M. Austin. Nuclear Reaction Rates and Carbon Star Formation. *Astrophys. J. Lett.*, 613:L73–L76, September 2004.

[HAL06] F. Herwig, S. M. Austin, and J. C. Lattanzio. Nuclear reaction rate uncertainties and astrophysical modeling: Carbon yields from low-mass giants. *Phys. Rev. C*, 73(2):025802, February 2006.

[HRS13] W.C. Haxton, R.G. Hamish Robertson, and Aldo M. Serenelli. Solar neutrinos: Status and prospects. *Annual Review of Astronomy and Astrophysics*, 51(1):21–61, 2013.

[HS08] W. C. Haxton and A. M. Serenelli. CN-Cycle Solar Neutrinos and Sun's Primordial Core Metalicity. *Astrophys. J.*, 687:678–691, 2008.

[ICF$^+$04] Gianluca Imbriani, H. Costantini, A. Formicola, D. Bemmerer, R. Bonetti, C. Broggini, P. Corvisiero, J. Cruz, Z. Fülöp, G. Gervino, A. Guglielmetti, C. Gustavino, G. Gyürky, A. P. Jesus, M. Junker, A. Lemut, R. Menegazzo, P. Prati, V. Roca, C. Rolfs, M. Romano, C. Rossi Alvarez, F. Schümann, E. Somorjai, O. Straniero, F. Strieder, F. Terrasi, H. P. Trautvetter, A. Vomiero, and S. Zavatarelli. The bottleneck of CNO burning and the age of Globular Clusters. *Astron. Astrophys.*, 420:625–629, June 2004.

[ICF$^+$05] Gianluca Imbriani, H. Costantini, A. Formicola, A. Vomiero, C. Angulo, D. Bemmerer, R. Bonetti, C. Broggini, F. Confortola, P. Corvisiero, J. Cruz, P. Descouvemont, Z. Fülöp, G. Gervino, A. Guglielmetti, C. Gustavino, G. Gyürky, A. P. Jesus, M. Junker, J. N. Klug, A. Lemut, R. Menegazzo, P. Prati, V. Roca, C. Rolfs, M. Romano, C. Rossi-Alvarez, F. Schümann, D. Schürmann, E. Somorjai, O. Straniero, F. Strieder, F. Terrasi, and H. P. Trautvetter. S-factor of ^{14}N(p,γ)^{15}O at astrophysical energies. *Eur. Phys. J. A*, 25:455–466, 2005.

[Ili07] Christian Iliadis. *Nuclear Physics of Stars.* Wiley-VCH, Weinheim, 2007.

[KBB$^+$10] David G. Koch, William J. Borucki, Gibor Basri, Natalie M. Batalha, Timothy M. Brown, Douglas Caldwell, Jörgen Christensen-Dalsgaard, William D. Cochran, Edna DeVore, Edward W. Dunham, Thomas N. Gautier III, John C. Geary, Ronald L. Gilliland, Alan Gould, Jon Jenkins, Yoji Kondo, David W. Latham, Jack J. Lissauer, Geoffrey Marcy, David Monet, Dimitar Sasselov, Alan Boss, Donald Brownlee, John Caldwell, Andrea K. Dupree, Steve B. Howell, Hans Kjeldsen, Sören Meibom, David Morrison, Tobias Owen, Harold Reitsema, Jill Tarter, Stephen T. Bryson, Jessie L. Dotson, Paul Gazis, Michael R. Haas, Jeffrey Kolodziejczak, Jason F. Rowe, Jeffrey E. Van Cleve, Christopher Allen, Hema Chandrasekaran, Bruce D. Clarke, Jie Li, Elisa V. Quintana, Peter Tenenbaum, Joseph D. Twicken, and Hayley Wu. Kepler mission design, realized photometric performance, and early science. *The Astrophysical Journal Letters*, 713(2):L79, 2010.

[KFFL53] A. A. Kraus, A. P. French, W. A. Fowler, and C. C. Lauritsen. Angular Distribution of Gamma-Rays and Short-Range Alpha-Particles from ^{15}N(p,$\alpha\gamma$)^{12}C. *Phys. Rev.*, 89(1):299–301, Jan 1953.

[KMH$^+$14] M. Kosmata, F. Munnik, D. Hanf, R. Grötzschel, S. Crocoll, and W. Möller. Oxygen depth profiling with subnanometre depth resolution. *Nucl. Inst. Meth. B*, 337:27–33, October 2014.

[LBC$^+$06] A. Lemut, D. Bemmerer, F. Confortola, R. Bonetti, C. Broggini, P. Corvisiero, H. Costantini, J. Cruz, A. Formicola, Z. Fülöp, G. Gervino, A. Guglielmetti, C. Gustavino, G. Gyürky, G. Imbriani, A. P. Jesus, M. Junker, B. Limata, R. Menegazzo, P. Prati, V. Roca, D. Rogalla, C. Rolfs, M. Romano, C. Rossi Alvarez, F. Schümann, E. Somorjai, O. Straniero, F. Strieder,

F. Terrasi, and H. P. Trautvetter. First measurement of the ^{14}N(p,γ)^{15}O cross section down to 70 keV. *Phys. Lett. B*, 634:483, 2006.

[LDDF12] L.P.B. Lima, J.A. Diniz, I. Doi, and J. Godoy Fo. Titanium nitride as electrode for MOS technology and Schottky diode: Alternative extraction method of titanium nitride work function . *Microelectronic Engineering*, 92:86 – 90, 2012. 27th Annual Advanced Metallization Conference 2010.

[LGd+16] Q. Li, J. Görres, R. J. deBoer, G. Imbriani, A. Best, A. Kontos, P. J. LeBlanc, E. Uberseder, and M. Wiescher. Cross section measurement of $^{14}\mathrm{N}(p,\gamma)^{15}\mathrm{O}$ in the CNO cycle. *Phys. Rev. C*, 93:055806, May 2016.

[LLH+16] W. Liu, Z. Li, J. He, X. Tang, G. Lian, Z. An, J. Chang, H. Chen, Q. Chen, X. Chen, Z. Chen, B. Cui, X. Du, C. Fu, L. Gan, B. Guo, G. He, A. Heger, S. Hou, H. Huang, N. Huang, B. Jia, L. Jiang, S. Kubono, J. Li, K. Li, T. Li, Y. Li, M. Lugaro, X. Luo, H. Ma, S. Ma, D. Mei, Y. Qian, J. Qin, J. Ren, Y. Shen, J. Su, L. Sun, W. Tan, I. Tanihata, S. Wang, P. Wang, Y. Wang, Q. Wu, S. Xu, S. Yan, L. Yang, Y. Yang, X. Yu, Q. Yue, S. Zeng, H. Zhang, H. Zhang, L. Zhang, N. Zhang, Q. Zhang, T. Zhang, X. Zhang, X. Zhang, Z. Zhang, W. Zhao, Z. Zhao, and C. Zhou. Progress of Jinping Underground laboratory for Nuclear Astrophysics (JUNA). In *European Physical Journal Web of Conferences*, volume 109 of *European Physical Journal Web of Conferences*, page 09001, February 2016.

[LSS63] J. Lindhard, M. Scharff, and H.E. Schioett. Range concepts and heavy ion ranges (notes on atomic collisions, ii). *Kgl. Danske Videnskab. Selskab. Mat. Fys. Medd.*, Vol: 33: No. 14, Jan 1963.

[LT58] A M Lane and R G Thomas. R-matrix theory of nuclear reactions. *Rev. Mod. Phys.*, 30:257–353, 1958.

[Lud17] Felix Ludwig. Der Myonenfluss im zukünftigen Felsenkeller Beschleunigerlabor. Master's thesis, Institut für Kern- und Teilchenphysik Technische Universität Dresden, 2017.

[MBB+03] A.M. Mukhamedzhanov, P. Bém, B. A. Brown, V. Burjan, C. A. Gagliardi, V. Kroha, J. Novák, F. M. Nunes, Š. Iskoř, F. Pirlepesov, E. Šimečková, R. E. Tribble, and J. Vincour. Asymptotic normalization coefficients for ^{14}N +p $\rightarrow$ ^{15}O and the astrophysical S factor for ^{14}N(p,γ)^{15}O. *Phys. Rev. C*, 67:065804, 2003.

[MBB+16] Juris Meija, Michael Berglund, Willi A. Brand, Paul De Biévre, Manfred Gröning, Norman E. Holden, Johanna Irrgeher, Robert D. Loss, Thomas Walczyk, and Thomas Prohaska. Atomic weights of the elements 2013 (IUPAC Technical Report). *Pure and Applied Chemistry*, 88(3):265–291, 2016.

[MdD+14] D. J. Mountford, R. J. deBoer, P. Descouvemont, A. S. J. Murphy, E. Uberseder, and M. Wiescher. Evaluation of the implementation of the R-matrix formalism with reference to the astrophysically important ^{18}F(p,α)^{15}O reaction. *Nucl. Inst. Meth. A*, 767:359–363, December 2014.

[MFB+11] M. Marta, A. Formicola, D. Bemmerer, C. Broggini, A. Caciolli, P. Corvisiero, H. Costantini, Z. Elekes, Z. Fülöp, G. Gervino, A. Guglielmetti, C. Gustavino, G. Gyürky, G. Imbriani, M. Junker, A. Lemut, B. Limata, C. Mazzocchi, R. Menegazzo, P. Prati, V. Roca, C. Rolfs, C. Rossi Alvarez, E. Somorjai, O. Straniero, F. Strieder, F. Terrasi, H. P. Trautvetter, and A. Vomiero. The ^{14}N(p,γ)^{15}O reaction studied with a composite germanium detector. *Phys. Rev. C*, 83(4):045804, April 2011.

[MFG+08] M. Marta, A. Formicola, G. Gyürky, D. Bemmerer, C. Broggini, A. Caciolli, P. Corvisiero, H. Costantini, Z. Elekes, Z. Fülöp, G. Gervino, A. Guglielmetti, C. Gustavino, G. Imbriani, M. Junker, R. Kunz, A. Lemut, B. Limata, C. Mazzocchi, R. Menegazzo, P. Prati, V. Roca, C. Rolfs, M. Romano, C. R. Alvarez, E. Somorjai, O. Straniero, F. Strieder, F. Terrasi, H. P. Trautvetter, and A. Vomiero. Precision study of ground state capture in the ^{14}N(p,γ)^{15}O reaction. *Phys. Rev. C*, 78(2):022802(R), August 2008.

[Mic13] Caterina Michelagnoli. *The lifetime of the 6.79 MeV state in ^{15}O as a challenge for nuclear astrophysics and γ-ray spectroscopy: a new DSAM measurement with the AGATA Demonstrator array*. PhD thesis, Università degli studi di Padova, 2013.

[MTB+10] M. Marta, E. Trompler, D. Bemmerer, R. Beyer, C. Broggini, A. Caciolli, M. Erhard, Z. Fülöp, E. Grosse, G. Gyürky, R. Hannaske, A. R. Junghans, R. Menegazzo, C. Nair, R. Schwengner, T. Szücs, S. Vezzú, A. Wagner, and D. Yakorev. Resonance strengths in the ^{14}N(p,γ)^{15}O and ^{15}N(p,$\alpha\gamma$)12C reactions. *Phys. Rev. C*, 81:055807, 2010.

[MTN12] Peter J. Mohr, Barry N. Taylor, and David B. Newell. Codata recommended values of the fundamental physical constants: 2010. *Rev. Mod. Phys.*, 84:1527–1605, Nov 2012.

[Mün57] A. Münster. Eigenschaften und anwendungen von titannitrid und titancarbid. *Angewandte Chemie*, 69(9):281–290, 1957.

[MVR75] M.A. Meyer, I. Venter, and D. Reitmann. Energy levels of ^{28}Si. *Nuclear Physics A*, 250(2):235 – 256, 1975.

[OBH+13] László Oláh, Gergely Gabor Barnaföldi, Gergö Hamar, Hunor Gergely Melegh, Gergely Suranyi, and Dezsö Varga. Cosmic muon detection for geophysical applications. *Advances in High Energy Physics*, 2013:7, 2013.

[Oec93] Hans Oechsner. Recent instrumental developments in surface and thin-film analysis by electron and mass spectrometric techniques. *Applied Surface Science*, 70-71(Part 1):250 – 260, 1993.

[OSB+13] Laszlo Oláh, Gergely Suranyi, Gergely Gabor Barnaföldi, Daniel Bemmerer, Gergö Hamar, Hunor Gergely Melegh, and Dezsö Varga. Cosmic Background Measurements at a Proposed Underground Laboratory by the REGARD Muontomograph. In *Proceedings of Nuclear Physics in Astrophysics VI, Lisbon, Portugal*, 2013.

[PTVF07] William H. Press, Saul A. Teukolsky, William T. Vetterling, and Brian P. Flannery. *Numerical Recipes 3rd Edition: The Art of Scientific Computing*. Cambridge University Press, New York, NY, USA, 3 edition, 2007.

[RAB+16] Tobias P. Reinhardt, Shavkat Akhmadaliev, Daniel Bemmerer, Klaus Stöckel, and Louis Wagner. Absolute hydrogen depth profiling using the resonant ^{1}H(^{15}N,α)^{12}C nuclear reaction. *Nucl. Inst. Meth. B*, 381:58 – 66, 2016.

[RCA+05] R. C. Runkle, A. E. Champagne, C. Angulo, C. Fox, C. Iliadis, R. Longland, and J. Pollanen. Direct Measurement of the ^{14}N(p,γ)^{15}O S Factor. *Phys. Rev. Lett.*, 94:082503, 2005.

[RCG+16] D. Robertson, M. Couder, U. Greife, F. Strieder, and M. Wiescher. Underground nuclear astrophysics studies with CASPAR. In *European Physical Journal Web of Conferences*, volume 109 of *European Physical Journal Web of Conferences*, page 09002, February 2016.

[RKMG92] M. E. Rudd, Y. K. Kim, D. H. Madison, and T. J. Gay. Electron production in proton collisions with atoms and molecules: energy distributions. *Rev. Mod. Phys.*, 64:441–490, Apr 1992.

[RMP+01a] V Rigato, G Maggioni, A Patelli, V Antoni, G Serianni, M Spolaore, L Tramontin, L Depero, and E Bontempi. Effects of plasma non-homogeneity on the physical properties of sputtered thin films. *Surface and Coatings Technology*, 142 - 144:943 – 949, 2001. Proceedings of the 7th International Conference on Plasma Surface Engineering.

[RMP+01b] V Rigato, G Maggioni, A Patelli, V Antoni, G Serianni, M Spolaore, L Tramontin, L Depero, and E Bontempi. Effects of plasma non-homogeneity on the physical properties of sputtered thin films. *Surface and Coatings Technology*, 142–144:943 – 949, 2001. Proceedings of the 7th International Conference on Plasma Surface Engineering.

[RR88] Claus Rolfs and William Rodney. *Cauldrons in the Cosmos*. University of Chicago Press, Chicago, 1988.

[SAA+13] K. Schmidt, S. Akhmadaliev, M. Anders, D. Bemmerer, K. Boretzky, A. Caciolli, D. Degering, M. Dietz, R. Dressler, Z. Elekes, Z. Fülöp, G. Gyürky, R. Hannaske, A. R. Junghans, M. Marta, M.-L. Menzel, F. Munnik, D. Schumann, R. Schwengner, T. Szücs, A. Wagner, D. Yakorev, and K. Zuber. Resonance triplet at E_α=4.5 MeV in the ^{40}Ca(α,γ)^{44}Ti reaction. *Phys. Rev. C*, 88(2):025803, August 2013.

[SBB+87] Uwe Schröder, H. W. Becker, G. Bogaert, J. Görres, C. Rolfs, H. P. Trautvetter, R. E. Azuma, C. Campbell, J. D. King, and J. Vise. Stellar reaction rate of ^{14}N(p,γ)^{15}O and hydrogen burning in massive stars. *Nucl. Phys. A*, 467:240–260, 1987.

[SBC+12] T. Szücs, D. Bemmerer, T. Cowan, D. Degering, Z. Elekes, Z. Fülöp, G. Gyürky, A. Junghans, M. Köhler, M. Marta, R. Schwengner, A. Wagner, and K. Zuber. Shallow-underground accelerator sites for nuclear astrophysics: Is the background low enough? *Eur. Phys. J. A*, 48:8, January 2012.

[SBR+15] T. Szücs, D. Bemmerer, T. P. Reinhardt, K. Schmidt, M. P. Takács, A. Wagner, L. Wagner, D. Weinberger, and K. Zuber. Cosmic-ray-induced background intercomparison with actively shielded HPGe detectors at underground locations. *The European Physical Journal A*, 51(3):1–9, 2015.

[Sch11] Konrad Schmidt. Experimente zur Entstehung von Titan-44 in Supernovae. Master's thesis, Institut für Kern- und Teilchenphysik Technische Universität Dresden, 2011.

[SHP11] A. M. Serenelli, W. C. Haxton, and C. Peña-Garay. Solar Models with Accretion. I. Application to the Solar Abundance Problem. *Astrophys. J.*, 743:24, December 2011.

[SPnGH13] Aldo Serenelli, Carlos Peña Garay, and W. C. Haxton. Using the standard solar model to constrain solar composition and nuclear reaction S factors. *Phys. Rev. D*, 87:043001, 2013.

[SWC$^+$17] Serenelli, A., Weiss, A., Cassisi, S., Salaris, M., and Pietrinferni, A. The brightness of the red giant branch tip - theoretical framework, a set of reference models, and predicted observables. *A&A*, 606:A33, 2017.

[TBSZ15] M. P. Takács, D. Bemmerer, T. Szücs, and K. Zuber. Constraining big bang lithium production with recent solar neutrino data. *Phys. Rev. D*, 91(12):123526, June 2015.

[Tro09] Erik Trompler. Messung des Wirkungsquerschnitts astrophysikalisch relevanter Kernreaktionen. Master's thesis, Technische Universität Dresden, Sep 2009. FZD Report FZD-523.

[TWC93] D.R. Tilley, H.R. Weller, and C.M. Cheves. Energy levels of light nuclei A = 16-17. *Nuclear Physics A*, 564(1):1 – 183, 1993.

[VRA$^+$17] Kuldeep Verma, Keyuri Raodeo, H. M. Antia, Anwesh Mazumdar, Sarbani Basu, Mikkel N. Lund, and Victor Silva Aguirre. Seismic measurement of the locations of the base of convection zone and helium ionization zone for stars in the kepler seismic legacy sample. *The Astrophysical Journal*, 837(1):47, 2017.

[WAW$^+$12] M. Wang, G. Audi, A.H. Wapstra, F.G. Kondev, M. MacCormick, X. Xu, and B. Pfeiffer. The Ame2012 atomic mass evaluation. *Chinese Physics C*, 36(12):1603, 2012.

[WE47] E. P. Wigner and L. Eisenbud. Higher angular momenta and long range interaction in resonance reactions. *Phys. Rev.*, 72:29–41, Jul 1947.

[YMA+04] K. Yamada, T. Motobayashi, H. Akiyoshi, N. Aoi, Z. Fülöp, T. Gomi, Y. Higurashi, N. Imai, N. Iwasa, H. Iwasaki, Y. Iwata, H. Kobayashi, M. Kurokawa, Z. Liu, T. Minemura, S. Ozawa, H. Sakurai, M. Serata, S. Shimoura, S. Takeuchi, T. Teranishi, Y. Yanagisawa, K. Yoshida, and M. Ishihara. E1 strength of the subthreshold $3/2^+$ state in ^{15}O studied by Coulomb excitation. *Phys. Lett. B*, 579:265–270, 2004.

[Zie13] J. Ziegler. SRIM version 2013.00, http://www.srim.org. Software SRIM, 2013.

[ZJAvdL90] F. Zijderhand, F. P. Jansen, C. Alderliesten, and C. van der Leun. Detector-efficiency calibration for high-energy gamma-rays. *Nucl. Inst. Meth. A*, 286(3):490 – 496, 1990.

[ZZB10] James F Ziegler, M D Ziegler, and J P Biersack. SRIM - The stopping and range of ions in matter (2010). *Nucl. Inst. Meth. B*, 268:1818–1823, 2010.

Danksagung

In dem langwierigen, herausfordernden Prozess dessen Resultat diese Arbeit ist, standen mir viele Personen mit Rat und Tat zu Seite bei denen ich mich vielmals bedanken möchte.

Zuallererst gilt mein Dank PD Dr. Daniel Bemmerer, der mir in seiner Arbeitsgruppe am HZDR die Möglichkeit gegeben hat tief in die Nukleare Astrophysik einzutauchen und einen Beitrag für dieses faszinierende Forschungsgebiet zu leisten. Ich schätze die zielführenden fachlichen Diskussionen genauso wie den lockeren Umgang miteinander und die interessanten Einblicke in Vorgänge des Wissenschaftsbetriebs am HZDR. Stets konnte ich auf Daniels Unterstützung bauen, sei es bei Hürden in dieser Arbeit, der Teilnahme an interessante Workshops oder dem zukünftigen beruflichen Werdegang.

Ein besonderer Dank gilt Prof. Dr. Kai Zuber, der mein Doktorvater an der TU Dresden ist. Seine Begeisterung für experimentelle Astrophysik, die er in seinen Vorlesungen ausstrahlt, ist sehr ansteckend und bestärkte mich diesem spannenden Gebiet der Physik auf den Grund zu gehen. Außerdem macht die langjährige Kollaboration von Kai mit dem Institut für Strahlenphysik am HZDR diese Doktorarbeit erst möglich.

Meinem Kollegen und guten Freund Stefan Reinecke möchte ich insbesondere für das ausführliche inhaltliche Korrekturlesen dieser Arbeit danken. Außerdem gebührt Stefan und allen anderen Kollegen, die bei den Experimenten geholfen haben mein herzlichster Dank. Hervorheben möchte ich Konrad Schmidt der 2013 die meisten Schichten übernommen hat genauso wie Martin Serfling 2014. Danke Leute, das ist erstklassiger Teameinsatz!

Meiner Familie möchte ich ebenso herzlich danken für die uneingeschränkte Unterstützung auf meinem bisherigen Weg. Egal bei welchen Sorgen oder Problemen, ich kann immer auf ihren Zuspruch und ihre Hilfe vertrauen und das gibt mir einen starken Rückhalt egal wo ich bin.

Für die Herstellung mehrerer TiN Proben nach meinen (unerwartet anspruchsvollen) Vorstellungen möchte ich Mario Steinert vielmals danken. Ebenfalls vom Ionenstrahl-Zentrum möchte ich Dr. Frans Munnik herzlich danken für die Durchführung und gemeinsame Analyse der ERD Messungen.

Die Experimente mit dem Myonen Teleskop im Felsenkeller zusammen mit Felix Ludwig

waren ein spannendes Highlight für das ich sehr dankbar bin und die Zusammenarbeit hat mir viel Freude gemacht.
I want to thank Dr. Michele Marta for the work on the ^{14}N(p,γ)^{15}O reaction, that he performed at HZDR before I started in 2012 because his setup laid a proper groundwork that I could build upon.
Gyürky György has my many thanks for the invitation and accommodation in Debrecen, Hungary to participate in the activation experiment on ^{14}N(p,γ)^{15}O and the provision of preliminary results. I can't await the final results Gyuri. Good luck!
I owe Dr. Richard James deBoer a dept of gratitude for his help with problems according the R-matrix software AZURE2 and the invitation and support to attend an insightful R-matrix workshop in Santa Fee, South Dakota, USA.
Last but not least I am deeply grateful for Markus Poschmann's hard work of proof reading this thesis to improve my English.

Erklärung

Hiermit versichere ich, dass ich die vorliegende Arbeit ohne unzulässige Hilfe Dritter und ohne Benutzung anderer als der angegebenen Hilfsmittel angefertigt habe. Die aus fremden Quellen direkt oder indirekt übernommenen Gedanken sind als solche kenntlich gemacht.
Diese Arbeit wurde an der TU Dresden und am Helmholtz-Zentrum Dresden Rossendorf unter wissenschaftlicher Betreuung von PD Dr. Daniel Bemmerer angefertigt. Die Arbeit wurde bisher weder im Inland noch im Ausland in gleicher oder ähnlicher Form einer anderen Prüfungsbehörde vorgelegt.
Ich erkenne hiermit die Promotionsordnung der Technische Universität Dresden Fakultät Mathematik und Naturwissenschaften Bereich Physik vom 23.02.2011 an.

Dresden, 11.01.2018
Louis Wagner